MAGNETIC CHARACTERISTICS OF ZINC SUBSTITUTED COBALT FERRITES

This Dissertation is submitted in partial fulfillment of the requirements for the degree of

Master of Philosophy

in

Physics, from the University of Dhaka

By

Tamanna Mariam

Registration No: 111

Session: 2015-2016

Department of Physics

University of Dhaka

August 2018

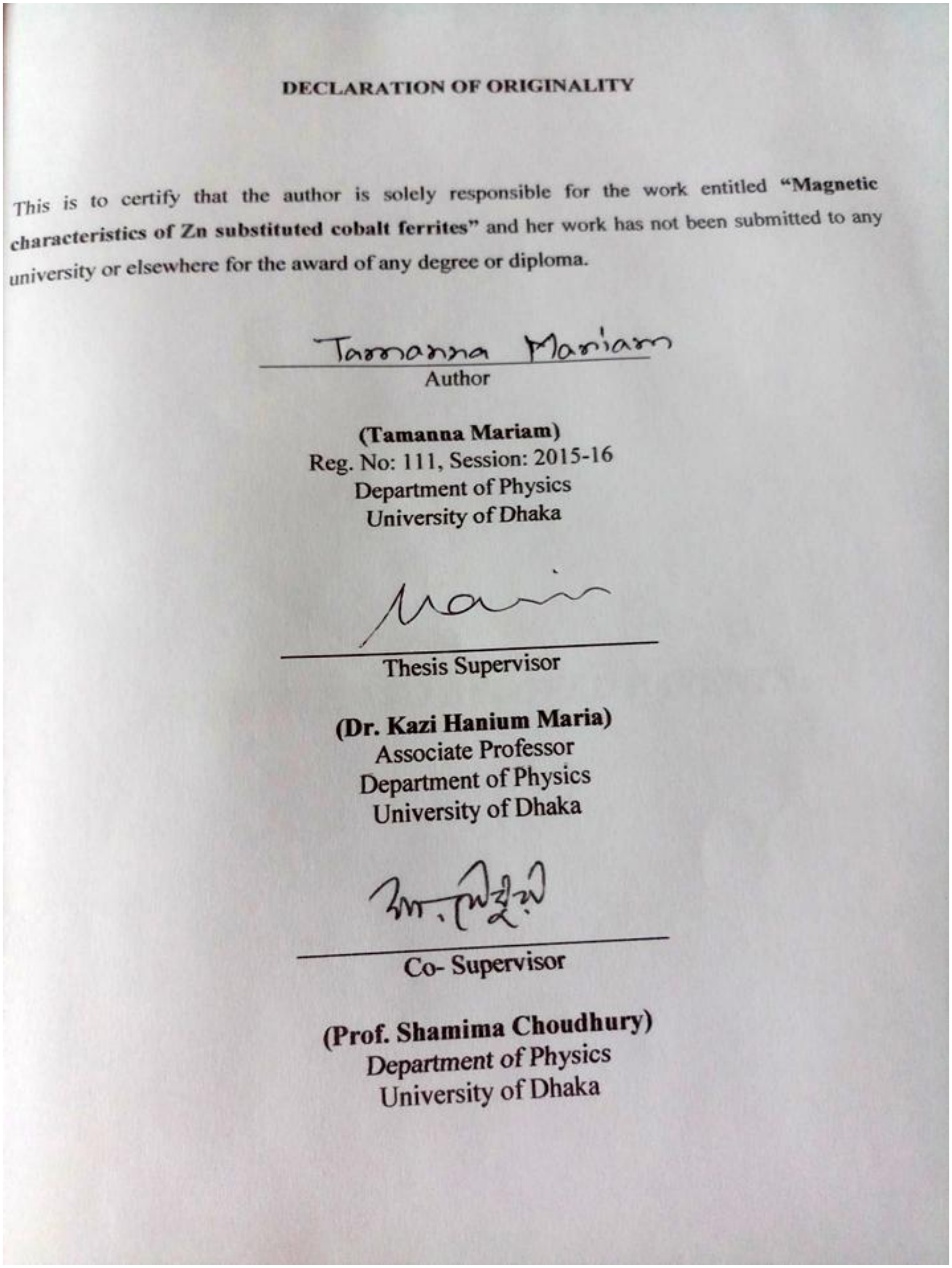

DECLARATION OF ORIGINALITY

This is to certify that the author is solely responsible for the work entitled **"Magnetic characteristics of Zn substituted cobalt ferrites"** and her work has not been submitted to any university or elsewhere for the award of any degree or diploma.

Tamanna Mariam

Author

(Tamanna Mariam)
Reg. No: 111, Session: 2015-16
Department of Physics
University of Dhaka

Thesis Supervisor

(Dr. Kazi Hanium Maria)
Associate Professor
Department of Physics
University of Dhaka

Co- Supervisor

(Prof. Shamima Choudhury)
Department of Physics
University of Dhaka

DEDICATED TO BELOVED PARENTS

ACKNOWLEDGEMENT

At the very first , I would like to express my admiration to praise the Almighty Allah who has given me the strength and opportunity to complete my research work and leading to M .Phil degree.

I take this opportunity to express my sincere gratitude and thanks to my honorable thesis supervisor Dr. Kazi Hanium Maria, Associate Professor, Department of physics, University of Dhaka, for guiding me as a mentor and encorage me by her constant guidance and supervision throughout the work.

I express my deepest sense of gratitude and profound respect to my co-supervisor honorable Prof. Shamima Choudhury, Department of physics, University of Dhaka, for her invaluable time, dedicationand helpful attitude provided during the work.

I am grateful to Dr. Nazrul Islam Khan, Principal Scientific Officer, Materials Science Division, Bangladesh Atomic Energy Commission,Dhaka for his valuable suggestions and helps throughout the research work.

I specially give thanks to Iffat Nur esha, Lecturer, Department of physics, University of Dhaka , for being patient and helpful during the measurement of the characteristics of the compositions and to the completion of my research.

I am thankful to Samia Islam Liba, Senior Scientific Officer and Arijun Nahar, Scientific Officer, Materials Science Division, Bangladesh Atomic Energy Commission,Dhaka for their cooperation, affection and inspiration throughout the work.

Finally, I would like to express my gratitude to my beloved parents for their tremendous support through all these years of my eduction. This dissertation would never have been possible without their love and affection.

Tamanna Mariam

21 May, 2019

ABSTRACT

A series of $Co_{1-x}Zn_xFe_2O_4$ ferrite(x=0.0, 0.1, 0.2, 0.3, 0.4, 0.5) compositions were synthesized using the standard double sintering ceramic technique, sintered at 1050°C for 2 hours. Substituting Zn in place of Co influenced the structural, dielectric and magnetic properties of $CoFe_2O_4$samples. Structural analyses were carried out using X-ray diffraction (XRD). The X-Ray diffraction pattern confirmed the single-phase cubic spinel structure and the sharp peak revealed that the samples are in good crystalline form. The lattice parameters were calculated for each composition and found to increase with Zn substitution. A significant increase in density and subsequent decrease in porosity were observed with increasing Zn content. The grain size of the samples was reduced by enhancing the Zn concentration. The dielectric constant (ε') of the sample is found to decrease with increase in frequency exhibiting normal dielectric behavior. Dielectric relaxation peaks were observed for the frequency dependence of dielectric loss tangent curves. The observed dielectric properties were explained on the basis of electron conduction mechanism. The variation of the resistivity versus temperature was also studied and the dielectric constant of the system has a variation quite similar to that of the resistivity. Vibrating Sample Magnetometer measurement confirmed that the magnetizations of all the samples were saturated. Saturation magnetization and coercivity were estimated with variation of Zn content. These effects are due to facilitation of demagnetization by substitution of the non-magnetic Zn ions. Permeability was found to decrease with increase in Zn content. Cobalt Ferrites have the characteristics of electromagnetism, excellent chemical stability, mechanical hardness, low coercivity, moderate saturation magnetization and high anisotropy constant. Hence, Zinc substituted Cobalt Ferrite is a good candidate for synthesizing as dielectric, magnetic, multiferroic material and also for using in storage devices in advancement of science and technology.

CONTENT

CHAPTER 1: INTRODUCTION AND REVIEW WORKS

CHAPTER 2: THEORETICAL BACKGROUND

2.2.1 Diamagnetism

2.2.2 Paramagnetism

2.2.3 Ferromagnetism

2.2.4 Antiferromagnetism

2.2.5 Properties of ferrimagnetism

2.2.6 Néel theory of ferrimagnetism

2.2.7 History of ferrite materials

2.2.8 Spinel structure of ferrites

2.2.9 Cation distribution of spinel ferrites

2.2.10 Canting effect in spinel ferrites

2.2.11 Interaction between magnetic moments on lattice sites

2.2.12 Magnetism in spinel ferrite

CHAPTER 3: SAMPLE PREPARATION

CHAPTER 4: EXPERIMENTAL PROCEDURES

CHAPTER 5: RESULTS AND DISCUSSION

CHAPTER 6: CONCLUSION

LIST OF FIGURES

LIST OF TABLES

LIST OF SYMBOLS AND ABBREVIATIONS

H	Magnetic field
H_C	Coercivity
M	Magnetization
Mr	Remanence
Tanδ	Loss factor
μ'	Real part of the complex permeability
μ''	Imaginary part of the complex permeability
ε'	Dielectric constant
B	Magnetic field
θ	Bragg’s law angle
C_0	Capacitance of the capacitor without the dielectric materials
XRD	X-Ray Diffraction
SEM	Scanning electron microscopy
EDX	Energy dispersive X-ray spectroscopy
VSM	Vibrating sample magnetometer

CHAPTER 1

INTRODUCTION AND REVIEW WORKS

CHAPTER 1

INTRODUCTION AND REVIEW WORKS

1.1 Introduction

The history of science became precious with the invention of magnet. The ability of magnets to attract ferrous objects upto a certain distance depending on its characteristics, has captivated countless curious spirits over two millennia including albert Einstein. Feeble permanent magnets are quite widespread in nature chemically known as iron oxide Fe_3O_4 – which were magnetized by huge electric currents in lightning strikes [1].

A lodestone carved in the shape of a Chinese spoon was the center piece of an early magnetic device, called 'South pointer'. Being used for geometrical purposes in China at the beginning of our era (Fig. 1.1), the spoon turns on the base to align its handle with the Earth's magnetic field. Evidence of the South pointer's application can also be seen in the grid-like street plans of certain Chinese towns.

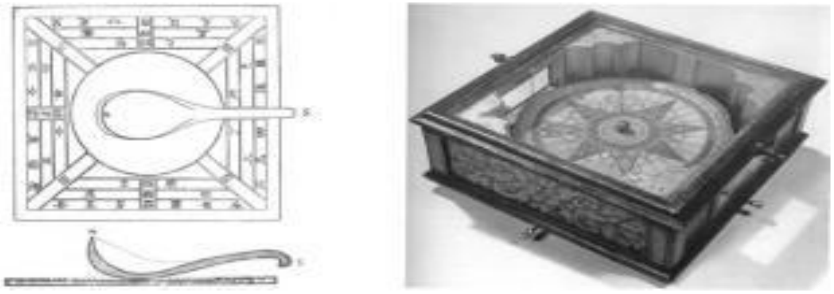

Figure 1.1: Some early magnetic devices: the 'South pointer' used for orientation in China around the beginning of the present era, and a Portuguese mariner's compass from the fifteenth century (adapted from ref. [1])

There is a long history of Magnetism. Below in Table 1.1 shows the seven ages of magnetism (adapted from ref. [1])

Period	Dates	Icon	Drivers	Materials
Ancient period	−2000B.C.–1500A.C.	Compass	State, geomancers	Iron, lodestone
Early modern age	1500–1820	Horseshoe magnet	Navy	Iron, lodestone
Electromagnetic age	1820–1900	Electromagnet	Industry/infrastructure	Electrical steel
Age of understanding	1900–1935	Pauli matrices	Academic	(Alnico)
High-frequency age	1935–1960	Magnetic	Military	Ferrites
Age of applications	1960–1995	Resonance Electric screwdriver	Consumer market	Sm-Co Nd-Fe-B
Age of spin electronics	1995–	Read head	Consumer market	Multilayers

Today, magnetic materials are found in numerous products around us- home appliances, electronic products, automobiles, communication equipment and data processing devices and equipment. These materials have now become a vital part of everyday life in modern life. The magnetic materials used in early applications were metallic magnetic materials. But for frequencies exceeding MHz, metals and alloys produced from soft magnets are generally not suitable, as the eddy current losses are very high. Since 1946, after the development of ferrites, it has been reported that electrical resistivity of ferrites is higher than those of metals and it has an enormous impact in the application of magnetic materials particularly at high frequencies.

Ferrites are ceramic and homogeneous materials composed of various oxides associated with iron oxide as their main constituent. They are brittle, polycrystalline and generally grey and black in color. In terms of magnetic properties, they are 'ferrimagnetic'. Ferrites can have several distinct crystal structures. In this work, we are concerned with magnetically soft ferrites, which have a spinal polycrystalline structure.

With rapid development of mobile communication and information technology, the electronic devices with small size, low cost and high performance are expected. Surface mounting devices and multilayer chip inductors are important components for the latest electronic products such as cellular phones, video cameras, notebook, hard and floppy drives, etc. These devices require light weight with better functions which become more integrated with the help of soft magnetic materials [2, 3].

Ferrite is a popular word in the field of magnetism for its multifunctional uses. Ferrite is the ceramic material which is also considered as metallic oxide. Cubic spinel type ferrite is considered as face centered cubic lattice (fcc) and the most common type of magnetic material in a sense of its combination with AB_2O_4 spinel structure where the ions are dispersed in two different lattice sites called tetrahedral (A) and octahedral (B) sites [4-7].

For commercial importance there has a great interest on the field of ferrite materials. The magnetic properties of Zn-substituted ferrites have attracted considerable attention because of their importance in high frequency applications [8]. Ferrite materials are also populated for its high frequency application and magneto di-electric properties especially in microwave and radio frequency region [9]. In the consideration of low frequency ferrite material there has a chance to pass eddy current through the material. Consequently, energy is wasted in the form of heat inside it [10].

The magnetic properties of ferrite depend on cation distribution in different lattice sites, preparing condition [11], sintering temperature, sintering time, heating and cooling rate. In general ferrite materials are synthesized by conventional ceramic method as well as solid state reaction method. In this process the sintering technique has to take for constructing the desire shape and the sintering temperature is high so it's responsible for the change in magnetization and resistivity of the materials.

Many scientists have the contribution on the research of magnetic ferrite material field. But Snoek and his associates firstly involved their self in commercial production of ferrite material at Phillips Research laboratory in the years of 1993-1945 in Holland [12-13]. Variety in content on ferrite material makes it more efficient, flexible and sustainable. Such as the addition or substitution of nonmagnetic materials like Li, Mg, Al, Cu, Zn etc on strongly influenced magnetic materials Cr, Mn, Fe, Co, Ni etc. can change their structural, magnetic and electrical properties.

The basic reasons of choosing ferrite material in research are:

- High quality factor and low loss factor, i.e. the electrical and magnetic performances are superb.
- In natural temperature it has low sensitivity.
- Over expected frequency band the materials are shown acceptable performance.
- The variation of time has no greater effect on susceptibility and sensibility.

- By changing the content in different percentages the properties of ferrite could be controlled which will show satisfactory behavior on application of it.
- The necessity in the development of modern technology and home appliances and also the availability of raw materials and production mechanism make the ferrite attractive to research on.

In this research Cobalt Iron Oxide, commonly known as Cobalt ferrite ($CoFe_2O_4$) is chosen to be substituted by Zn in place of Co which has the formula $Co_{1-x}Zn_xFe_2O_4$($x=0.0-0.5$). Cobalt ferrite ($CoFe_2O_4$) is a well-known ferroelectric materials. Ferroelectric magnets simultaneously show the properties of ferroelectrics and ferromagnets [14]. Ferroelectric materials possess two or more orientational states in the absence of an electric field and can be changed from one to another of these states by the application of an electric field. The combination of magnetic and electrical properties makes ferroelectric-magnet useful in many technological applications. It has covered a wide range of applications including electronic devices, high density information storage devices, high rate of change of strain with magnetic field, high coercivity, moderate saturation magnetization, high Curie temperature T_C, photo magnetism, good electrical insulation etc [15-19]. Cobalt ferrites are suitable for magnetic recording applications such as audio and videotape and high-density digital recording disks etc [20]. Cobalt ferrites are the subject of much interest due to their unusual optical, electronic and magnetic properties. Cobalt iron oxide has achieved fair interest to work on it to improve its structural, magnetic, electric properties etc. Substitution of rare earth (Y^{3+}, Gd^{3+}, Ho^{3+}, Sm^{3+}, Nd^{3+}) ion into cobalt ferrites has been reported to lead to structural distortion that induces strains in the material which indicate improved crystallinity of the sample and to affect the electrical and magnetic properties significantly [21].

On the other hand, several researches have been done on non-magnetic metals substituted ferrites like Zn substitution in place of Co. As for example, A. Hassadee *et al.* [22] reported on the effect of Zinc-substituted cobalt ferrites, $Co_{1-x}Zn_xFe_2O_4$ (x = 0.0 – 0.5) prepared by ceramic processing. The results revealed that the spinel structure was modified by the substituted ions. In $Co_{1-x}Zn_xFe_2O_4$ samples, Zn^{2+} went to A-site and resulted in an increase in the lattice parameter. Magnetization measurements indicated that Zn substituted Cobalt Ferrite showed ferrimagnetic behavior at room temperature. The saturation magnetization and the coercivity of the $Co_{1-x}Zn_xFe_2O_4$ samples were investigated to be decreased by increasing the Zn content.

The works of A. Hassadee *et al.* [22] and K.H. Maria *et al.* [40] were seen to be more attractive for this research work. So Zn substituted Cobalt Ferrites with general formula $Co_{1-x}Zn_xFe_2O_4$(x=0.0-0.5) were synthesized by Solid State Reaction method in this research and their structural, morphological, magnetic and dielectric properties were investigated by doping Zinc in place of Cobalt.

1.2 Review of earlier research

A large number of researchers all over the world are working on Ferrites and the findings are publishing in national and international journals. A brief review of these research is given below:

- A. Hassadee *et al.* [22] reported about the effect of zinc substitution on structural and magnetic properties of cobalt ferrite. Zinc-substituted cobalt ferrites, $Co_{1-x}Zn_xFe_2O_4$ (x = 0.0 – 0.5), were prepared by ceramic processing. The structural, morphological and magnetic properties of the products were determined by X-ray diffractometry (XRD), scanning electron microscopy (SEM), and vibrating sample magnetometer (VSM) respectively. The results revealed that the spinel structure was also modified by the substitute ions. In $Co_{1-x}Zn_xFe_2O_4$ samples, Zn^{2+} commonly substitute for Co^{2+}, resulting in an increase in the lattice parameter from 8.381 – 8.412 Å. Magnetization measurements indicated that $Co_{1-x}Zn_xFe_2O_4$ samples with x = 0.0 – 0.5 showed ferrimagnetic behavior at room temperature. The decrease in the maximum magnetization of the $Co_{1-x}Zn_xFe_2O_4$ samples from 134 to 100 emu/g and the decrease in the coercivity of the $Co_{1-x}Zn_xFe_2O_4$ samples from 140 to 4 Oe by increasing the zinc content from 0.0 to 0.5 can be attributed to the magnetic characteristic and the anisotropic nature of cobalt.

- S. Singhal *et al.* [23] investigated Zinc substituted cobalt ferrite nanoparticles ($Co_xZn_{1-x}Fe_2O_4$, with x = 0.0, 0.2, 0.4, 0.8 and 1.0) which were prepared via sol-gel route and the effect of zinc concentration on saturation magnetization and lattice parameter were investigated. The particle sizes of the as obtained samples were found to be ~10 nm which increases up to ~92 nm on annealing at 1000°C. The frequency bands near 564-588 cm^{-1} and 425-442 cm^{-1} are assigned to the tetrahedral and octahedral clusters which confirm the presence of M-O stretching band in ferrites. The unit cell parameter ‘a’ increases linearly with increasing con-centration of zinc due to larger ionic radii of Zn^{2+} ion. It was found that this substitution allows tunable changes in the magnetic properties of cobalt ferrite. Interestingly, saturation magnetization first increases up to x = 0.4 and then de-creases for higher Zn substitution, thus tunable changes in magnetic properties of cobalt ferrite are possible. Source of such behavior could be the variation of exchange interaction between the tetrahedral and the octahedral sites.
- S. Tapdiya and A.K. Shrivastava [24] reported that Zinc substituted cobalt ferrite nanoparticles ($Co_{1-x}Zn_xFe_2O_4$, with x = 0.0, 0.1, 0.2 and 0.3) were prepared via chemical co precipitation method. The effect of zinc concentration on saturation magnetization and

lattice parameter were investigated. The particle sizes of the as obtained samples were found to be 22 to 38 nm. The frequency bands near 598 cm^{-1} and 421 cm^{-1} are assigned to the tetrahedral and octahedral clusters which confirm the presence of M-O stretching band in ferrites. The unit cell parameter ‘a’ increases linearly with increasing concentration of zinc due to larger ionic radii of Zn^{2+} ion. It was found that this substitution allows tunable changes in the magnetic properties of cobalt ferrite. Saturation magnetization increases as Zn was substituted, thus tunable changes in magnetic properties of cobalt ferrite are possible. Source of such behavior could be the variation of exchange interaction between the tetrahedral and the octahedral sites.

- M.T. Jamil *et al.* [25] investigated on a series of spinel ferrites with composition $Zn_xCo_{1-x}Fe_2O_4$ ($0 \leq x \leq 1$) which has been synthesized via co-precipitation route. The samples have been characterized by means of X-ray Diffraction (XRD), Scanning Electron Microscope (SEM), Fourier Transform Infrared (FTIR) Spectroscopy, UV-Visible Spectroscopy and Photoluminescence (PL) Spectroscopy. X-ray diffraction (XRD) technique was applied to characterize the nanoparticles. The particle size of the obtained samples, calculated by using Scherrer’s formula, were found in the range of 30 to 70 nm on annealing at $700°C$. The Scanning Electron Microscope was used to study the morphology of the synthesized samples which revealed the heterogeneous grain size distribution. FTIR transmittance spectroscopy was used to investigate the bonding among different atoms present in the sample. The frequency bands near 564-588cm^{-1} and 425-442 cm^{-1} are assigned to the tetrahedral and octahedral clusters which confirm the presence of metal oxygen (M-O) stretching band in ferrites. UV-visible spectroscopy was used to calculate optical energy band gap by using Tauc relation.

- A. Khan *et al.* [26] reported about Effect of Zn content on the dielectric and transport properties of $CoZn_xFe_{2-x}O_4$ (x = 0.0, 0.1,0.2, 0.3 and 0.4), prepared by standard double sintering ceramic technique, sintered at 1000^oC for 4 hours were investigated. The X-ray diffraction (XRD) pattern of the prepared samples showed single phase inverse-spinel structure without any detectable impurity. Lattice constant of the samples increased with the increasing Zn concentration which follows Vegard's law. The theoretical densities of these samples remained almost constant whereas the bulk density decreased with Zn content up to x = 0.2. But with further increase of Zn content the bulk density increased. The porosity of the prepared samples showed the opposite trend. The dielectric constant (ϵ') measurement showed the normal dielectric behavior of the prepared ferrite. The DC electrical resistivity of the prepared samples decreased with the increasing temperature which indicates the semiconducting behavior of the prepared ferrites. The Zn concentration showed pronounced effect on the resistivity at room temperature. Possible explanation for the observed features of densities, porosity, dielectric constant and resistivity of the studied samples are discussed.
- R. Rani *et al.* [27] investigated on zinc substituted cobalt Nano ferrites, with formula $Co_{1-x}Zn_xFe_2O_4$ (x = 0.0, 0.1, 0.2, 0.3, 0.4), have been prepared by solution combustion method and are investigated for their electric and dielectric properties such as dc resistivity, dielectric constant and dielectric loss. Analysis of the X-ray diffraction pattern of all the samples confirmed the formation of spinel structure. The surface morphology of the samples was studied by using TEM. The dc resistivity was found to be increasing with an increasing substitution of zinc ions and the high value of dc resistivity, 108 Ωcm, make these nanoferrites more suitable at high frequency applications. Dielectric constant

and dielectric loss tangent, measured in the frequency range from 1kHz to 1MHz, were found to decrease with an increase in frequency. Possible mechanisms responsible for the results are discussed minutely in this paper.

- A.S.F. El-Saaey *et al.* [28] reported on nano-crystalline zinc-substituted cobalt ferrite powders, $Co_{1-x}Zn_xFe_2O_4$(X=0.0, 0.1, 0.3, 0.5, 0.7, 0.9 and 1.0), which have been synthesized by the Co-precipitation method. The structural and magnetic properties of the products were determined and characterized in detail by X-ray diffraction (XRD), High Resolution -Transmission Electron Microscope (HR-TEM), Fourier Transform Infrared (FTIR) and vibrating sample magnetometer (VSM). X-ray analysis showed that the samples were cubic spinel. The increase in zinc concentration resulted in an increase in the lattice constant, X-ray density, ionic radii, the distance between the magnetic ions and bond lengths on tetrahedral sites and octahedral sites of cubic spinel structure. The HR-TEM and XRD shows that crystallite size was ranging from 6–24 nm. The FTIR measurements between 400 and 2000 cm^{-1} confirmed the intrinsic cation vibrations of the spinel structure. The variation of saturation magnetization (M_S) and Magnetic coercivity of the samples were studied. The magnetic measurements show that the saturation magnetization and coercivity decrease by increasing the zinc content. Furthermore, the results reveal that the sample with a chemical composition of $Co_{0.3}Zn_{0.7}Fe_2O_4$ exhibits the super-paramagnetic behavior.
- S.K. Gore *et al.* [29] investigated on the bismuth (Bi^{3+})-doped cobalt ferrite nanostructures with dual phase, i.e. cubic spinel with space group Fd3m and perovskite with space group R3c, have been successfully engineered via self-ignited sol-gel combustion route. To obtain information about the phase analysis and structural

parameters, like lattice constant, Rietveld refinement process is applied. The replacement of divalent Co^{2+} by trivalent Bi^{3+} cations have been confirmed from energy dispersive analysis of the ferrite samples. The micro-structural evolution of cobalt ferrite powders at room temperature under various Bi^{3+} doping levels have been identified from the digital photo images recorded using scanning electron microscopy. The hyperfine interactions, like isomer shift, quadrupole splitting and magnetic hyperfine fields, and cation distribution are confirmed from the Mossbauer spectra. Saturation magnetization is increased with Bi^{3+}-addition up to $x = 0.15$ and then is decreased when $x = 0.2$. The coercivity is increased from 1457 to 2277 G with increasing Bi^{3+}-doping level. The saturation magnetization, coercivity and remanent ratio for $x = 0.15$ sample is found to be the highest, indicating the potential of Bi^{3+} doping in enhancing the magnetic properties of cobalt ferrite.

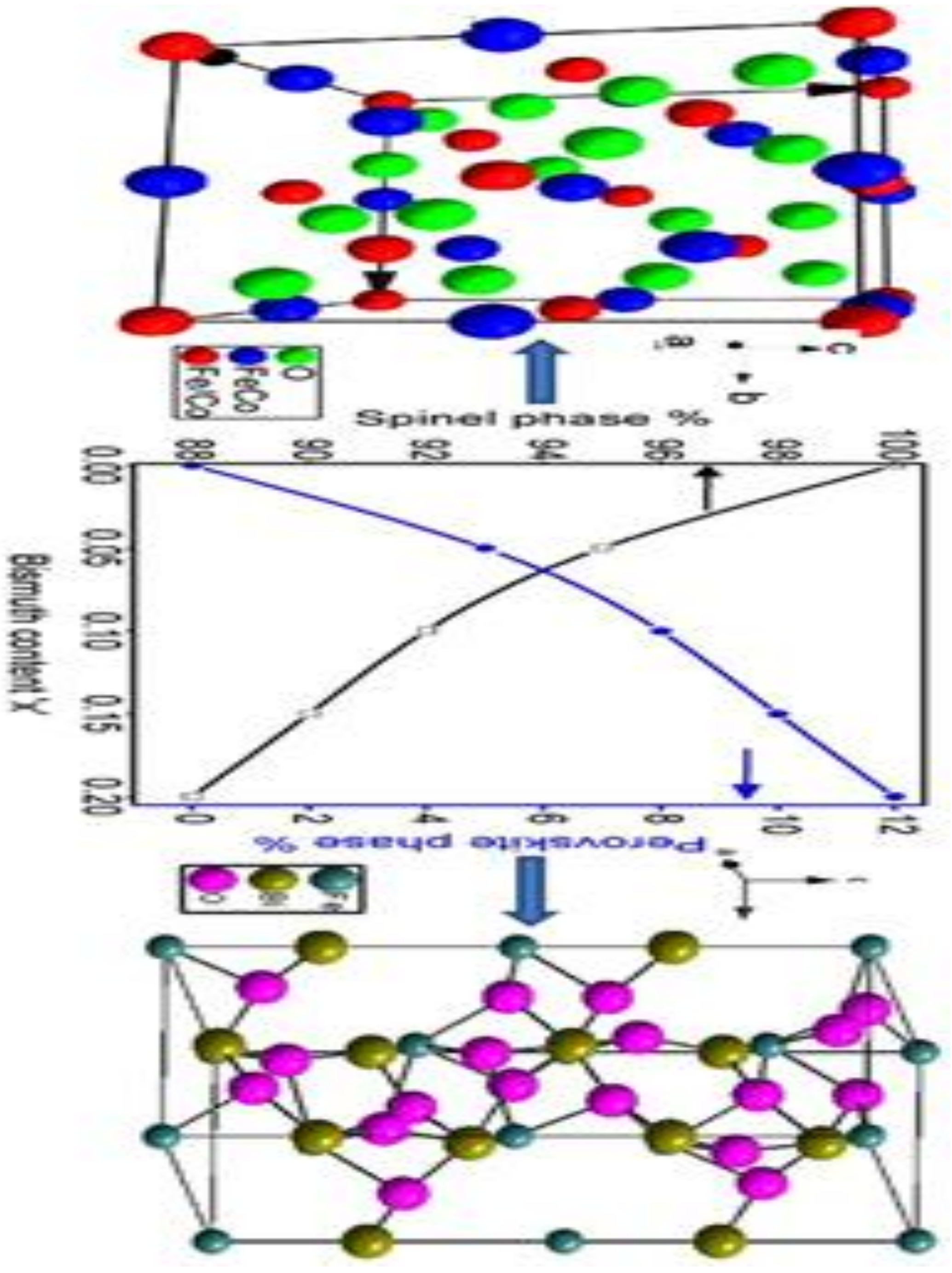

Figure 1.2: Influence of Bi^{3+}-doping on spinel (left) and perovskite (right) phases of CBF [Adapted from ref. [29]]

- K. Praveena and K. Sadhana [30] focuses on two systems, nanocrystalline Zn substituted $Co_{1-x}Zn_xFe_2O_4$ ($0 \leq x \geq 1$) and $Ni_{0.4}Zn_{0.2}Mn_{0.4}Fe_2O_4$, were synthesized using microwave hydrothermal and auto-combustion method respectively. The synthesized powders were characterized by X-ray diffraction (XRD), transmission electron microscope (TEM), thermo-gravimetric-differential thermal analysis (TG-DTA) and FTIR. The average particle size was obtained from TEM and it is found to be 17 nm. Zero field cooled (ZFC) and Field cooled (FC) measurements for $Co_{1-x}Zn_xFe_2O_4$ reveal that samples with $0.6 \leq x \geq 1$ have superparamagentic behavior at room temperature, which confirms weak interaction between magnetic particles. The blocking temperatures obtained form ZFC-FC curves decreases as Zn concentration increases. Lower reduced remnant magnetization (Mr/Ms) values ($x < 0.5$) suggest that all the samples have uniaxial anisotropy. For $Ni_{0.4}Zn_{0.2}Mn_{0.4}Fe_2O_4$ bulk densities of the samples were increased with an increase of sintering temperature. The grain sizes of all the samples vary in between 18 nm to 30 nm. The hysteresis loops show high saturation magnetization and low coercivity, indicates that it is a soft material. The incremental permeability (permeability with magnetic field superposition) was influenced by both ΔM and Hc. So these ferrites has the properties and are widely used as electromagnetic wave absorbing materials in the VHF/UHF region and as radar absorbing materials in C-band frequencies.

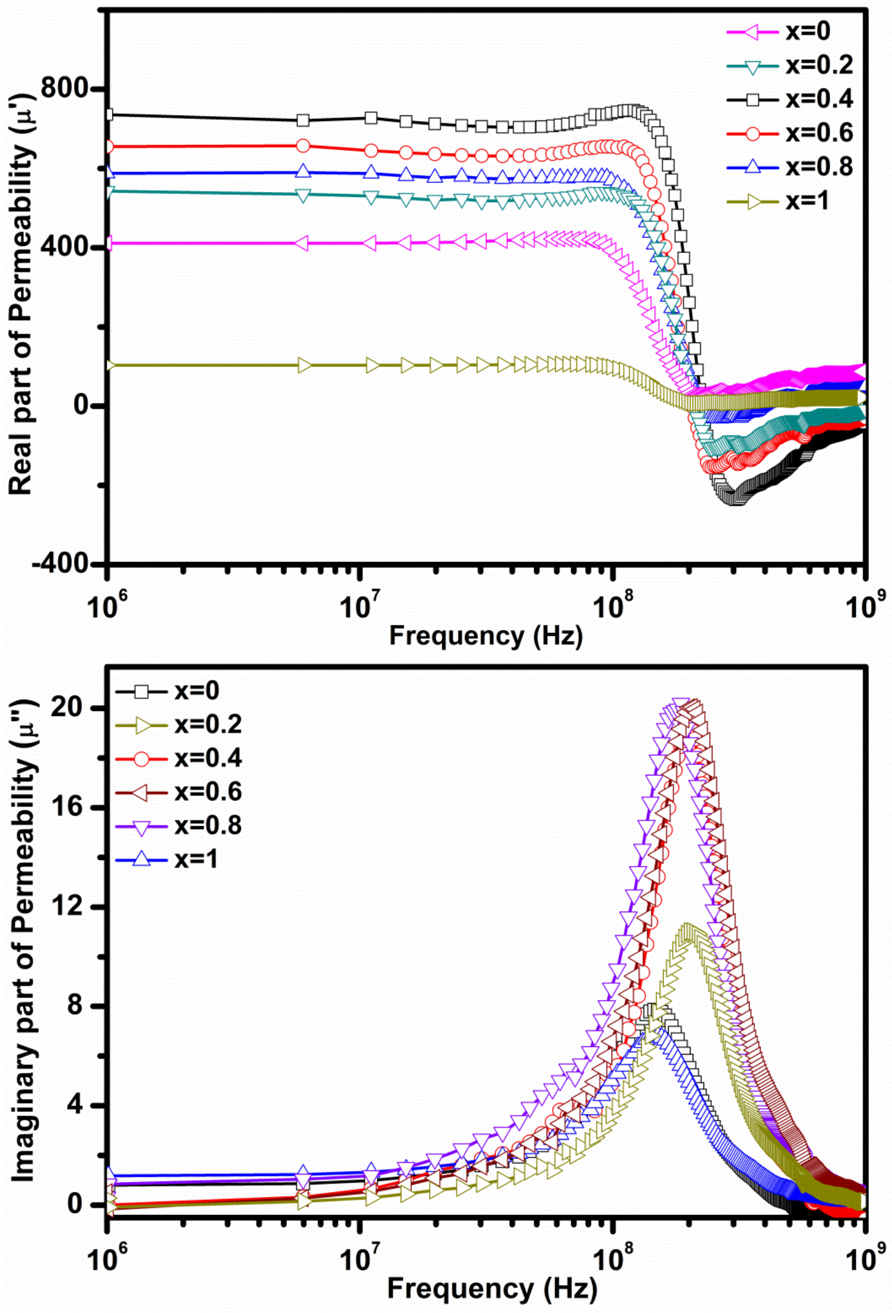

Figure 1.3: a. Frequency variation of real part of permeability of $Co_{1-x}Zn_xFe_2O_4$($0 \le x \le 1$)

b. Frequency variation of imaginary part of permeability of

$Co_{1-x}Zn_xFe_2O_4$ ($0 \le x \le 1$) (adapted from ref. [30])

- James M. Byrne *et al*. [31] found that The magnetic moments of magnetite nanoparticles are dramatically enhanced through the addition of zinc in a microbiologically driven synthesis procedure. The particles are produced through the reduction of Fe(III)-compounds containing Zn(II) by the iron reducing bacterium Geobacter sulfurreducens. Results indicate a significant increase in the saturation magnetization by over 50% compared to magnetite at both room and low temperatures for relatively minor quantities of zinc substitution. A maximum saturation magnetization of nearly 100 emug^{-1} of sample is measured at room temperature. Analysis of the cation site ordering reveals a complex dependence on the Zn content, with the combined effect of Zn substitution of Fe^{3+} ions on tetrahedral sites, together with Fe^{2+} cation oxidation, leading to the observed magnetization enhancement for low Zn doping levels. The improved magnetic properties give superior performance in MRI applications with an MRI contrast enhancement among the largest values reported, being more than 5 times larger than a commercial contrast agent (Feridex) measured under identical conditions. The synthesis technique applied here involves an environmentally benign route and offers the potential to tune the magnetic properties of magnetic nanoparticles, with increased overall magnetization desirable for many different commercial applications.

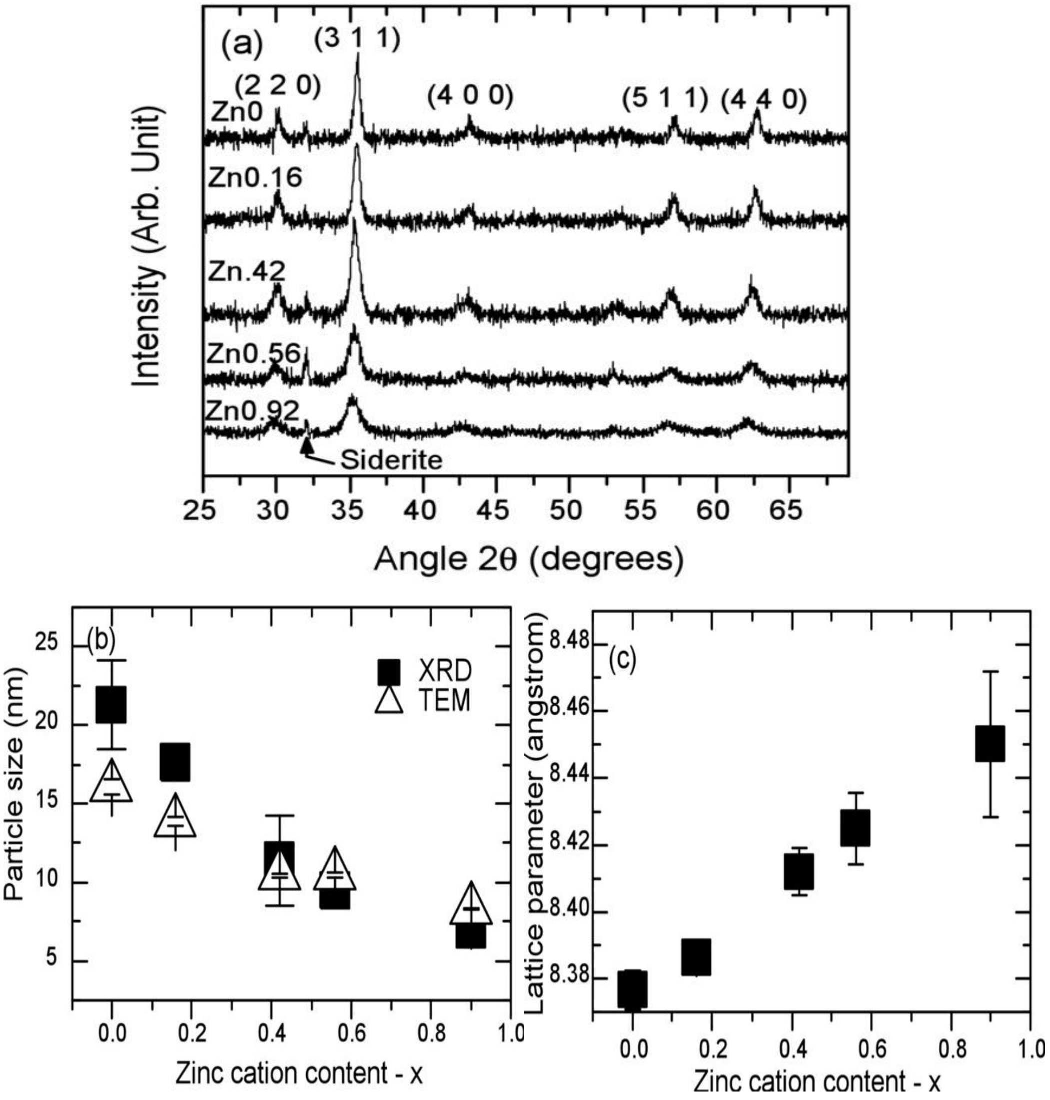

Figure 1.4: Powder X-ray diffraction data. a) XRD patterns displaying magnetite and zinc doped magnetite peaks. Siderite is also present. b) Mean crystallite particle size from powder XRD compared to TEM determined by fitting a Lorentzian curve to all peaks, then using the Scherrer equation to calculate mean particle size, compared against TEM determined mean size. c) Lattice parameter for magnetite with error bars determined from the standard deviation from the mean of all fitted powder XRD reflections (adapted from ref. [31]).

- M. Ranjani *et al.* [32] reported on synthesis and characterization of soft $Co_{1-x}Zn_xFe_2O_4$ magnetic nanoparticles synthesized using sol-gel method. The prepared nanoparticles were characterized by using Fourier transform infrared spectroscopy (FTIR), X-ray diffraction (XRD), Thermo Gravimetric-Differential Thermal Analysis(TGDTA), Scanning Electron Microscopy (SEM), Energy Dispersive X-ray Spectrum(EDX) and Vibrating Sample Magnetometer(VSM). Using XRD, it is confirmed that the samples were cubic structure in nature and the mean crystalline size were decreases from 16nm to 11nm respectively. The morphology and the quantitative analysis of the prepared particles were studied by using SEM and EDX spectrum. The FTIR was used to study the presence of functional groups. Finally, the magnetic properties of the powders have been studied at room temperature from the hysteresis loop measurements using a Vibrating Sample Magnetometer (VSM). From this analysis it was observed that the values of the saturation magnetization increased and the coercive field of $Co_{1-x}Zn_xFe_2O_4$ nanoparticles were found to decrease with increasing degree of Zn substitution.

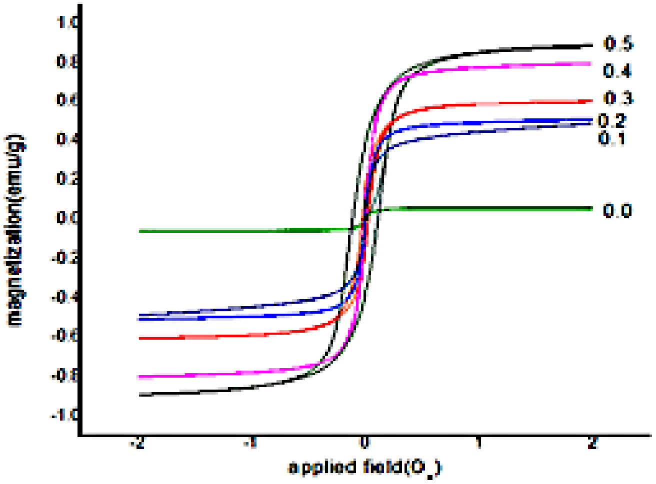

Figure 1.5: Room temperature hysteresisloopsof $Co_{1-x}Zn_xFe_2O_4$at 800°C annealingtemperature(adapted from ref. [32])

- N
  .

Somaiah *et al.* [33] reported on Cobalt-ferrite ($CoFe_2O_4$) based materials are suitable candidates for magneto mechanical sensor applications owing to a strong sensitivity of their magnetostriction to an applied magnetic field. Zn-doped cobalt-ferrites, with nominal compositions $CoFe_{2-x}Zn_xO4$ (x = 0–0.3), were synthesized by auto-combustion technique using Co-, Fe-, and Zn nitrate as precursors. X-ray spectra analysis and Transmission electron microscopy studies revealed that the as-prepared powders were comprised of nano-crystalline (~25–30 nm) cubic-spinel phase with irregularly-shaped grains morphology along with minor impurity phases. Calcination (800°C for 3 h) of the precursor followed by sintering (1300 °C for 12 h) resulted in a single phase cubic-spinel structure with average grain size ~2–4μm, as revealed from scanning electron micrographs. The magnitude of coercive field decreases from ~540 Oe for x = 0 to 105 Oe for x = 0.30. Saturation magnetization initially increases and peaks to ~87 emu/g for x = 0.2 and then decreases. The peak value of magnetostriction monotonically decreases with increasing Zn content in the range 0.0–0.3; however the piezomagnetic coefficient ($d\lambda/dH$) reaches a maximum value of 105×10^{-9} Oe^{-1} for x = 0.1. The observed variation in piezomagnetic coefficient in the Zn substituted cobalt ferrite is related to the reduced anisotropy of the system. The Zn doped cobalt-ferrite (x = 0.1) having high strain derivative could be a potential material for stress sensor application.

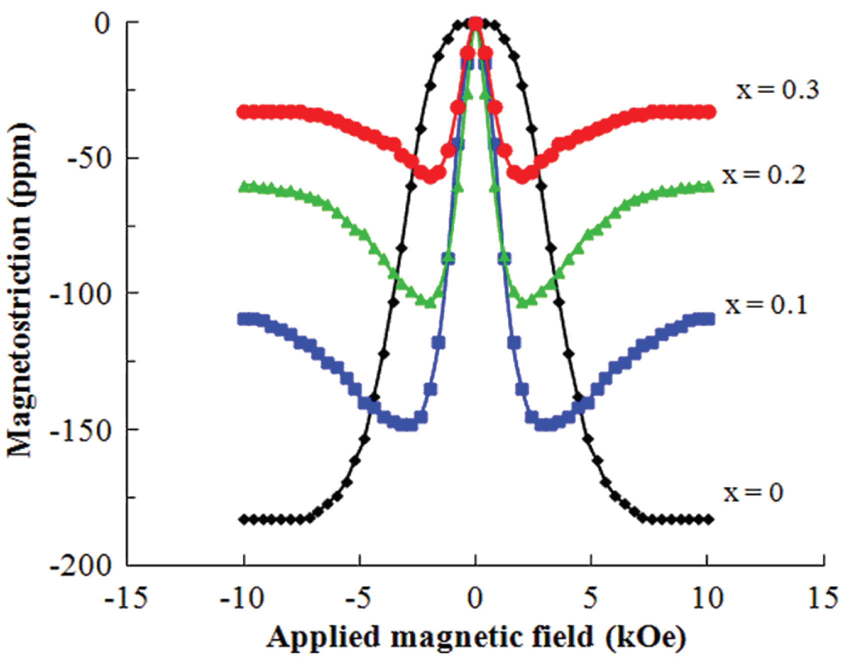

Figure 1.6: Magnetostriction (*λ*–*H*) curves of CoZn*x*Fe2−*x*O4, (*x* = 0, 0.1, 0.2 and 0.3) at ambient temperature (~298 K) (adapted from ref. [33])

- T.Joseph and D.Pamu [34] reported on a series of Zn doped Cobalt ferrite with formula $Co_{1-x}Zn_xFe_2O_4$ (x = 0.2, 0.35,0.5, 0.65 and 0.8). The nanoparticles were prepared using reverse co-precipitation method with different Zn concentrations. The XRD patterns showed that the undertaken materials exhibit spinel structure with non-preferential orientation. The structure of the as prepared samples $Co_{1-x}Zn_xFe_2O_4$ is found to be spinel structure and, which is confirmed using X-ray diffraction analysis. The particle size (11. 25 nm to 6.24 as x varies from 0.2 to 0.8) and its distribution may be controlled by changing the Zn content in the Co1-xZnxFe2O4 investigated by the XRD and HRSEM. The lattice parameters a= 8.03609 Å (x = 0.2) is observed to decrease as Zn concentration is increased to x = 0.8 (a= 8.2233 Å). The saturation magnetization, which decreased from 58.03 to 10 emu/gm for the increase of Zn content from 0.2 to 0.8 moles at room temperature, appears to be due to pronounced growth of magnetic anisotropy. The values of coercivity decreased from 103.5Oe to 0.931Oe as Zn content increased from 0.02 to 0.8. It is observed that the magnetization reminisce ratio has decreased from 0.0826 to 0.00048 at room. The magnetic measurements have been carried out using VSM and Tc measurements. The measurements revealed that the samples are super paramagnetic innature.

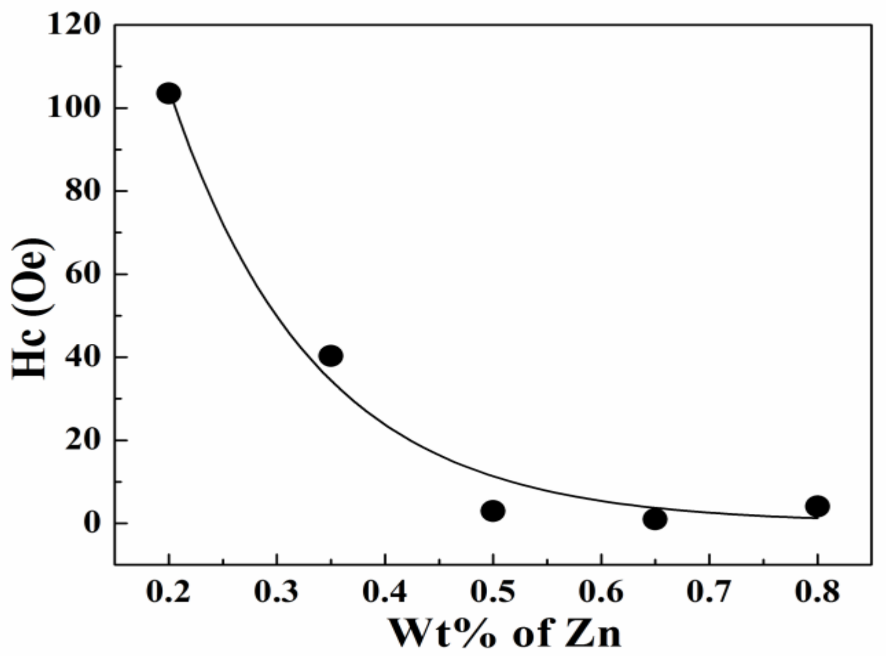

Figure 1.7: Variation of Coercivity of Zn content change in $Co_{1-x}Zn_xFe_2O_4$ (x = 0.2, 0.35,0.5, 0.65 and 0.8) (adapted from ref. [34])

- S.T.Aloneand K.M. Jadhav [35] investigated on Spinal ferrites having the general formula $Co_{1-x}Zn_xFe_{2-x}Al_xO4$ ($x = 0{:}0,0.1, 0.2, 0.3, 0.4, 0.5, 0.6$) were prepared using the wet chemical co-operation technique. The samples were annealed at 800±C for 12 h and were studied by means of X-ray diffraction, magnetization and low field AC susceptibility measurements. The X-ray analysis showed that all the samples had single-phase cubic spinel structure. The variation of lattice constant with Zn and Al concentration deviates from Vegard's law. The saturation magnetization ¾s and magneton number n_B measured at 300 K using high field hysteresis loop technique decreases with increasing x, suggesting decrease in ferrimagnetic behaviour. Curie temperature T_C deduced from AC susceptibility data decreases with x, suggesting a decrease in ferrimagnetic behavior.

- I. Ahmad and M. T. Farid [36] reported on A series of Gd-substituted Cobalt based ferrites of nominal composition $CoGd_{2-x}Fe_{2-2x}O_4$ for x= 0.00-0.25 in steps of 0.05 was produced by conventional ceramic technique. From X-Ray diffraction patterns, all samples showed single cubic spinel structure as a main phase along with small traces of second phase ($GdFeO_3$). The lattice parameter 'a' initially increases for x = 0.05 and then decreases with increasing value of x. dc resistivity and activation energies showed increasing trend with increasing Gd contents. The temperature dependent resistivity and activation energy decreases with increasing temperature. In all samples, saturation magnetization increases while the coercivity decreases with increasing Gd content. The increases in dc resistivity and saturation magnetization suggest that these materials are suitable for high density recording media and microwave devices. The structural, physical, electrical and magnetic properties of Gd-substituted Cobalt based ferrites are discussed in the current paper.

- N. M. Nee and M. R. Johan [37] reported on the composition of silver iodide rich solid solutions $AgI_{(x)}$-$Zn_{(1-x)}$I2 ($0.5 \leq x \leq 1$) were prepared using mechano-chemical technique. Addition of ZnI2 content reduces the degree of crystallinity of samples. Sample with 70% AgI shows the most amorphous structure. From the DSC curve, the glass transition temperature (Tg) of 70% AgI is 80.91ºC. The increasing ZnI2 content decreases the Tg of AgI-ZnI2 system. 70% of AgI exhibited the highest conductivity at room temperature, which is 1.913 × 10-4S/cm. The flexural modulus and ultimate flexural strength for 70% AgI are 0.069MPa and 0.058MPa respectively. Sample with 70% of AgI was used for battery fabrication. Open circuit voltage and the internal resistance obtained are 0.654V and 4.4Ω respectively.

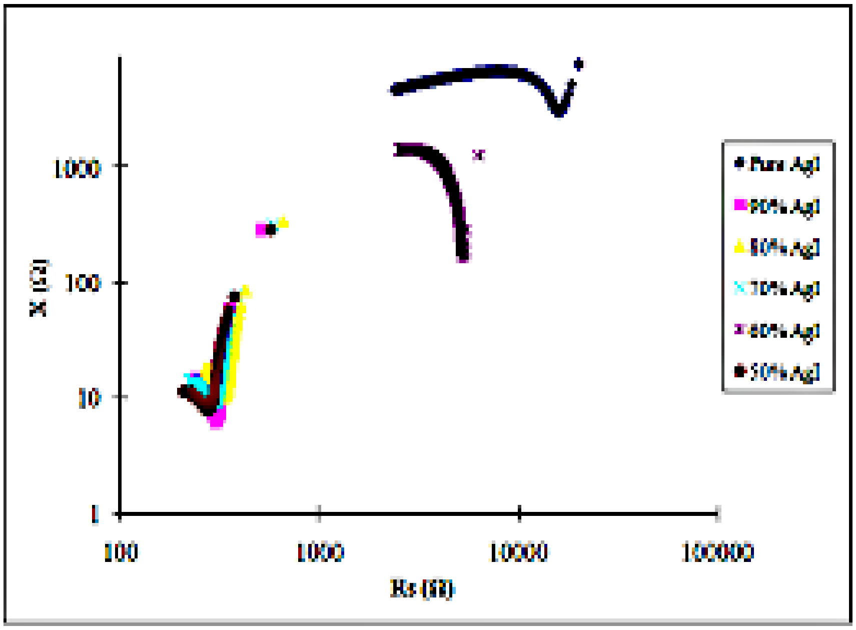

Figure 1.8: The cole-cole plot for silver rich AgI-ZnI_2 system at various compositions (adapted from ref. [37])

- M. Bouhbou *et al.* [38] reported on The influence of Zn substitution on the magnetic and magnetocaloric properties of $Cd_{1-x}Zn_xCr_2Se_4$ ($0.35 \leq x \leq 0.45$) spinel was investigated. All the samples exhibited two successive magnetic transitions associated with the reentrant spin glass at a freezing temperature (T_f) and Curie temperature (T_C). It was demonstrated that T_f changed slightly with the Zn content; however, the T_C value decreased with increasing Zn content due to the decrease of lattice constant. The magnetic entropy variation ($-\Delta S$) was found to exhibit two maxima at T_C and T_f , which have an opposite trend as a function of Zn content. With increasing Zn content, ($-\Delta S_M$) was found to decrease at T , whereas at T , ($-\Delta S_M$) increased. It was shown that the change of ($-\Delta S_M$) is closely correlated to the local exponent factor n at both transitions. The results showed that materials with double magnetic transitions could be integrated in a new class of magnetic refrigeration working in different temperature windows.
- M. Houshiar*et al.* [39] reported on cobalt ferrite ($CoFe_2O_4$) nanoparticles which are synthesized using three different methods; combustion, co precipitation, and precipitation. Size, structural, and magnetic properties were determined and compared using X-ray diffraction (XRD), scanning electron microscopy (SEM), and vibrating sample magnetometer (VSM). XRD data analysis showed an average size of 69.5 nm for combustion, 49.5 nm for co precipitation, and 34.7 nm for precipitation samples which concorded with SEM images. XRD data further revealed a reverse cubic spinel structure with the space group *Fd*-3*m* in all three samples. VSM data of samples showed a saturation point in the magnetic field of less than 15 kOe. Magnetization saturation (M_s) was 56.7 emu/g for combustion synthestized samples, 55.8 emu/g for co precipitation samples, and 47.2 emu/g for precipitation samples. Coercivity (H_c) was 2002 Oe for

combustion synthestized samples, 850 Oe for co precipitation samples, and 233 Oe for precipitation samples. These results show that various methods of nanoparticle synthesis can lead to different particle sizes and magnetic properties. H_c and M_s are greatest in the combustion method and least in precipitation method.

- K.H. Maria *et al.* [40] investigated on Zn doped Cu ferrite of the composition $Cu_{1-x}Zn_xFe_2O_4$ ferrites for x = 0, 0.1, 0.2, 0.3, 0.4, 0.5,0.6 prepared by standard double sintering ceramic technique. SEM micrograph of all the samples revealed that the grain sizes decrease gradually with the increase of Zn content and has great influence on the magnetic and transport properties. Permeability is found to increase with increase in Zn content up to x = 0.4 and then slightly decreases with further increase in Zn. The values of relative quality factor (RFQ) changes with Zn concentration. Room temperature DC resistivity changes significantly with Zn addition. The variation of the resistivity versus frequency was studied and the dielectric constant of the system has a variation quite opposite to that of the AC resistivity. Dielectric constant shows the normal behaviour of the ferrite materials that can be explained by the interfacial polarization as predicted by Maxwell and Wagner.
- S.M. Haque et al. [41] reported on soft magnetic properties of Co-based amorphous alloy of the composition $Co_{67}Fe_4Ni_2Si_{15}B_{12}$ which have been investigated by isothermal heat treatment up to the conventional crystallization temperature. In the as-cast condition the Curie temperature of the sample is 272 °C and saturation magnetization is 74 emu/g. Magnetic properties undergo variation depending on the heat treatment temperature. For the heat treatment temperatures of around 420 and 490 °C, superior soft magnetic properties are obtained. For both the temperatures initial permeability, μ' reaches value up

to ten times the value of permeability in the as-received samples. Annealing effect on giant magneto-impedance has been observed for the current-driving frequencies of 4.5 and 6 MHz. Field dependence of magneto-impedance shows hysteresis at low field, which is related to the changes in the magnetization process of the sample.

1.3 Objectives of the present work

The main objectives of the present research work are as follows:

- Various $Co_{1-x}Zn_xFe_2O_4$(x=0-0.5) compositions are prepared by double sintering solid state reaction method.
- Structural characterization has been performed by X-ray diffraction (XRD). From the XRD results lattice parameter, density and porosity of all compositions are determined.
- From microstructural analysis, the average grain sizes of all compositions have been measured to investigate the influence of grain size on the domain wall motion, density and porosity of the above mentioned compositions.
- The variations of saturation magnetization (M_s), remanence (B_r) and coercivity (H_c) with different compositions have been studied using M-H loops measured at room temperature.
- Temperature dependent initial permeability μ has been measured which indicates the strength of the exchange interaction among magnetic cations.
- Measurement of Dielectric Constant (ƙ) with respect to Frequency and a graphical representation has been shown.
- Temperature dependent resistivity has been studied.

Structure of the thesis

This research work has been configured into six chapters which are as follows.

Chapter one: Introduction

Chapter one presents a general introduction. Some earlier and a number of literatures of recent works are reviewed to understand the scientific importance of those studies need for the present investigation and the objectives of the study.

Chapter two: Theoretical Background

Chapter two describes the details about magnetism and magnetic materials, coercivity, remenance, dielectric properties etc.

Chapter Three: Sample Preparation

the experimental techniques are briefly explained in chapter three. The detailed discussion of the sample preparation and the techniques are explained here.

Chapter Four: Experimental Background

The brief description of the experimental setup and instrumentation of the different characterization techniques are presented in chapter four.

Chapter Five: Results and Discussion

The structural, dielectric, magnetic properties are presented in chapter five. The variation of the phase impurity, lattice parameter, grain size, density, porosity, dielectric constant, magnetism, permeability, temperature dependent resistivity is measured in this chapter.

Chapter Six: Conclusion

finally, the conclusions of the work done and suggestions for the future research on these ceramics are included in chapter six.

References:

[1] J.M.D. Coey; Magnetism and Magnetic Materials; Cambridge University Press, New York; (2009); Introduction.

[2] N. Varalaxmi, and K. Sivakumar, World J. Conden. Matt. Phys., 1 (2011) 105.

[3] T. Nomura and A. Nakano, Proceedings of ICF-6, Japan Society of Powder and Powder Metallurgy, (1992) 1198.

[4] Goldman, A., “Modern Ferrite Technology”, Van Nostrand Reinhold, New York, (1990).

[5] D. J. Craik, Magnetic Oxide, part 1, John Wiley and Sons, Ltd., Bristol, England, (1975).

[6] E. J. W. Verway, and E. L. Heilmann, J. Chem. Phys., 15 (1947) 174.

[7] S. Chickazumi, and S. H. Charap, “Physics of Magnetism”, Krieger Malabar, (1978).

[8] K.H. Maria, S. Choudhury and M.A. Hakim, International Nano Letters, 42 (2013) 1.

[9] P.B. Belavi, G.N. Chavan, L.R. Naik, R. Somshekar, and R.K. Kotnala, Mat. Chem. And Phys., 132 (2012) 138.

[10] K. Mathuraman, V. Naidu, S.K.A. Ahamed, and T. Vasudevan, Int. J. Comp. App. 65(2013) 0975.

[11] J. Smith, and H.P.J. Wijn, Ferrites, Wiley, London, (1959) 140.

[12] S. Hilpert, B. Deutseh, Chem. Ges. BD2, 42 (1909) 2248.

[13] M. Sugimoto, J. Am. Ceram. Soc., 82 (1999) 269.

[14] G. A. Smolenskioe, V. A. Bokov, V. A. Isupov, N. N. Kraoenik, R. E. Pasynkov, A. I. Sokolov, and N. K. Yushin, Physics of Ferroelectric Phenomena (Nauka, Leningrad, 1985) [in Russian].

[15] Y. Chen, J.E. Snyder, C.R. Schwichtenberg, K.W. Dennis, R.W. McCallum and D.C. Jiles, IEEE Trans. Magn., 35 (1999) 3652.

[16] A. Lisfi and C.M. Williams, J. Appl. Phys. 93 (2003) 8143.

[17] H.T. Jeng and G.Y. Guo, J. Magn. Magn. Mater. 239 (2002)88.

[18] J.C. Slonczewski, Phys. Rev. 110 (1958) 1341.

[19] C.N. Chinnasamy, B. Jeyadevan, K. Shinoda, K. Tohji, D.J. Djayaprawira, M. Takahashi, R.J. Joseyphus and A. Narayanasamy, Appl. Phys. Lett. 83 (2003) 2862.

[20] M.L. Kahn, Z. J. Zhang, Applied Physics Letters 78 (2001) 23.

[21] M.A. Rahman, M.A. Gafur and M.A.R. Sarker, IJIRAE, 2 (2015) 99.

[22] A. Hassadee, T. Jutarosaga and W. Onreabroy, Procedia Engineering, 32 (2012) 597.

[23] S.Singhal, T. Namgyal, S.Bansal and K.Chandra, J. Electromagnetic Analysis and Applications, 2 (2010) 376.

[24] S. Tapdiya and A.K. Shrivastava, IJIRSET, 5 (2016) 6681.

[25] M. T. Jamil, J. Ahmad, S. H. Bukhari, T. Sultan, M. Y. Akhter, H. Ahmad and G. Murtaza, J. Ovonic Research, 13(2017) 45.

[26] A. Khan, M.A. Bhuiyan, G.D. Al-Quaderi, K.H. Maria, S. Choudhury, K.A. Hossain, S. Akther and D.K. Saha, J. Bang. Aca. Sci, 37 (2013) 73.

[27] R. Rani, G. Kumar, K.M. Batoo and M. Singh, American J. Nanomaterials, 1 (2013) 9.

[28] A.S.F. El-Saaey, A.E.F.M. Khourshid, A. E. El-Hammady and A.R.A. Badawi, IOSR-JAC, 7(2014) 30.

[29] S.K. Gore, S.S. Jadhav, V.V. Jadhav, S. M. Patange, Mu. Naushad, R.S. Mane and K. H. Kim, Scientific Reports, 7 (2017) 1.

[30] K. Praveena and K. Sadhana, International Journal of Scientific and research publications, 5 (2015) 1.

[31] J.M. Byrne, V.S. Coker , E.Cespedes , P.L. Wincott , D.J. Vaughan , R.A. D. Pattrick , G.V.D. Laan , E. Arenholz , F. Tuna , M. Bencsik , J.R. Lloyd and N.D. Telling, Adv. Funct. Mater, 24(2014) 2518.

[32] M. Ranjani, Dr.Sr.Jesurani, M.Priyadharshini and S. Vennila, International Journal of Engineering Research and Technology (IJERT), 5 (2016) 882.

[33] N. Somaiah, T.V. Jayaraman, P.A. Joy and D. Das, Journal of Magnetism and Magnetic Materials, 324 (2012) 2286.

[34] T. Joseph and D. Pamu, International Journal of Science and Research (IJSR), ISSN (Online), (2013) 2319.

[35] S.T. Alone and K.M. Jadhav, Indian Academy of Sciences, 70 (2008) 172.

[36] I. Ahmad and M. T. Farid, World Applied Sciences Journal, 19 (2012) 464.

[37] N.M. Nee and M. R. Johan, Int. J. Electrochem. Sci., 7 (2012) 2448.

[38] M. Bouhbou, R. Moubah, W. Belayachi, A. Belayachi and H. Lassri, Dalton Transitions, 47 (2017) 2007.

[39] M. Houshiar, F.Z. Zahra, J. Razi, A. Alidoust, Z. Askari, Journal of Magnetism and Magnetic Materials, 371 (2014) 43.

[40] K.H. Maria, S. Choudhury and M.A. Hakim, J.Bangladesh Acad. of Sci., 34 (2010)1.

[41] S.M. Haque, F.A.Khan and M.A.Hakim, Phy.B: Cond.Matt. 390 (2007) 245.

CHAPTER 2

THEORETICAL BACKGROUND

CHAPTER 2

THEORETICAL BACKGROUND

2.1 Origin of magnetism

Almost everyone is familiar with what a magnetic material can do but very few know how a magnet works. To understand this phenomenon, one must first grasp the inextricable connection that exists between magnetism and electricity. A simple electromagnet can be produced by wrapping copper wire into the form of a coil and connecting the wire to a battery.

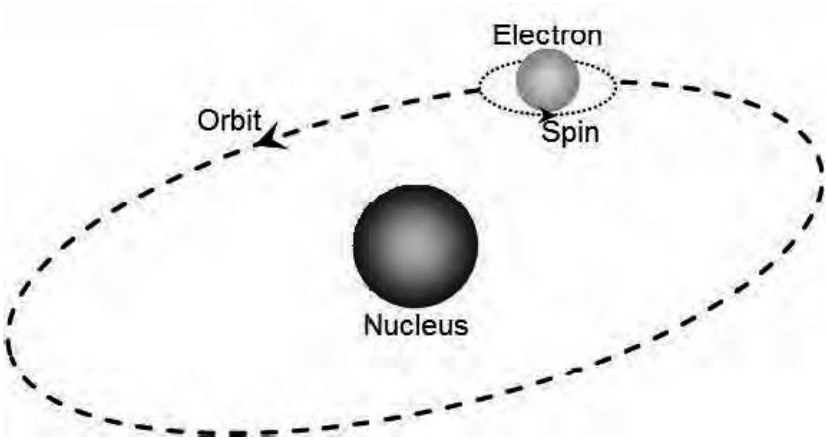

Figure 2.1: The orbit of a spinning electron about the nucleus of an atom

(adapted from ref. [1])

A magnetic field is created in the coil but it remains there only while electricity flows through the wire. An ordinary bar magnet does not have an obvious connection with electricity so how does it work? The field created by the magnet is associated with the motions and interactions of its electrons, the minute charged particles which orbit the nucleus of each atom. Electricity is the movement of electrons, whether in a wire or in an atom, so each atom represents a tiny permanent magnet in its own right. The circulating electron produces its own orbital magnetic moment, and there is also a spin magnetic moment associated with it due to the electron's own spin about its axis as illustrated in Fig. 2.1. So the origin of magnetism lies in the orbital and spin motions of electrons and how the electrons interact with one another. In most materials there are resultant magnetic moments, due to the electrons being grouped in pairs causing the magnetic moment to be cancelled by its neighbor [1-4].

In certain magnetic materials the magnetic moments of a large proportion of the electrons align, producing a unified magnetic field. The field produced in the material has a direction of flow and any magnet will experience a force trying to align it with an externally applied field. These forces are used to drive electric motors, produce sounds in a speaker system, control the voice coil in a CD player etc. The interactions between magnetism and electricity are therefore an essential aspect of many devices we use every day.

2.2Magnetic ordering

The magnetic properties of a matter are fundamentally the result of the electrons of the atom, which have a magnetic moment by means of the electrons motion. The response of a material to a magnetic field is represented by the magnetization. Many materials containing transition elements behave as if they were spontaneously magnetized. Fe, Co, Ni, Gd and many of their alloys, as well as many of their oxides and fluorides exhibit spontaneous magnetic ordering. The magnetic behavior of materials can be classified into five major groups [5, 6]. They are discussed below and their different types of magnetic moment ordering are shown in Fig. 2.2.

2.2.1 Diamagnetism

Diamagnetism is an inherent property of the orbital motion of the individual electron in a field. Since it is even a weaker effect than para magnetism, it is only observed when the atom does not have a net spin or orbital moment. The orbital motion even though compensated sets up a field opposite to the applied field in a manner similar to the back emf of Lenz's Law. The effect leads to a negative susceptibility or the actual lowering of the net moment in the material as an external field is applied. Diamagnetism is so weak an effect that a small paramagnetic impurity can offer mask out the effect.

2.2.2 Paramagnetism

If an atom has a net magnetic moment, (it is paramagnetic), this moment may be partially aligned in the direction of an applied magnetic field. Each atom therefore acts as an individual magnet in a field. The process of rotating these moments against thermal agitation is a difficult one and a large field is necessary to achieve only a small degree of alignment or magnetization. In many paramagnetic materials such as in hydrated salts, as the temperature is raised, the thermal agitation of the spins reduces even this small amount of alignment.

Pierre Curie showed that in these cases, the susceptibility, χ, which is defined as

$$\chi = M/H \tag{2.1}$$

Where χ = susceptibility, M = magnetization or moment, H = Magnetic field strength

follows the Curie Law given as,

$$\chi = C/T \tag{2.2}$$

Where: C = Curie constant,T = Temperature in Degrees Kelvin

Also,

$$1/\chi = T/C \tag{2.3}$$

2.2.3 Ferromagnetism

In ferromagnetic materials (as in paramagnetic materials), the alignment of magnetic moments in a magnetic field at higher temperature is decreased. Since a much greater degree of alignment occurs in ferromagnetic, the effect is even more pronounced. With further temperature increase, the thermal agitation will exceed the exchange forces and at a certain temperature called the Curie point, ferromagnetism disappears.

Above the Curie point, the ferromagnetic material becomes paramagnetic, the susceptibility of which decreases with temperature. If the reciprocal susceptibility, $1/\chi$, is plotted against T, the curve obeys the Curie Weiss Law,

$$1/\chi = 1/[C(T-T_C)] \tag{2.4}$$

Where, C = Curie Weiss Constant, T_c = Curie point

2.2.4 Antiferromagnetism

A simple antiferromagnet can be visualized as consisting of two magnetic sub lattices (A and B). In the magnetically ordered state, the atomic moments are parallel or ferromagnetically coupled within each of the two sub lattices. Any two atomic magnetic moments belonging to different sub lattices have an antiparallel orientation. Since the moments of both sub lattices have the same magnitude and since they are oriented in opposite directions, one finds that the total magnetization of an antiferromagnet is essentially zero (at least at zero kelvin). Many antiferromagnetic substances are oxides, the classic case being MnO.

In ferromagnetism, the interaction of atomic spin moments was a positive one meaning that the exchange interaction aligned neighboring spins parallel in a magnetic domain. antiferromagnetic susceptibility of the Curie-Weiss law at high temperatures with negative θ as,

$$\chi = C/(T+\theta) \tag{2.5}$$

where θ = Experimentally determined constant

$$\text{Also } \chi = C/(T-T_N) \qquad (2.6)$$

where T_N= Néel Temperature

2.2.5 Properties of ferrimagnetism

In ferrimagnetic substances, in contrast with the antiferromagnets the magnetic moments of the A and B sub lattices are not equal (as shown in Fig. 2.2). The magnetic atoms (A and B) in a crystalline ferrimagnet occupy two kinds of lattice sites that have different crystallographic environments. Each of the sub lattices is occupied by one of the magnetic species, with ferromagnetic (parallel) alignment between the moments residing on the same sublattice. There is antiferromagnetic (antiparallel) alignment, however, between the moments of A and B. Since the number of A and B atoms per unit cell are generally different, and/or since the values of the A and B moments are different, there is nonzero spontaneous magnetization below T_c [1-3, 5].

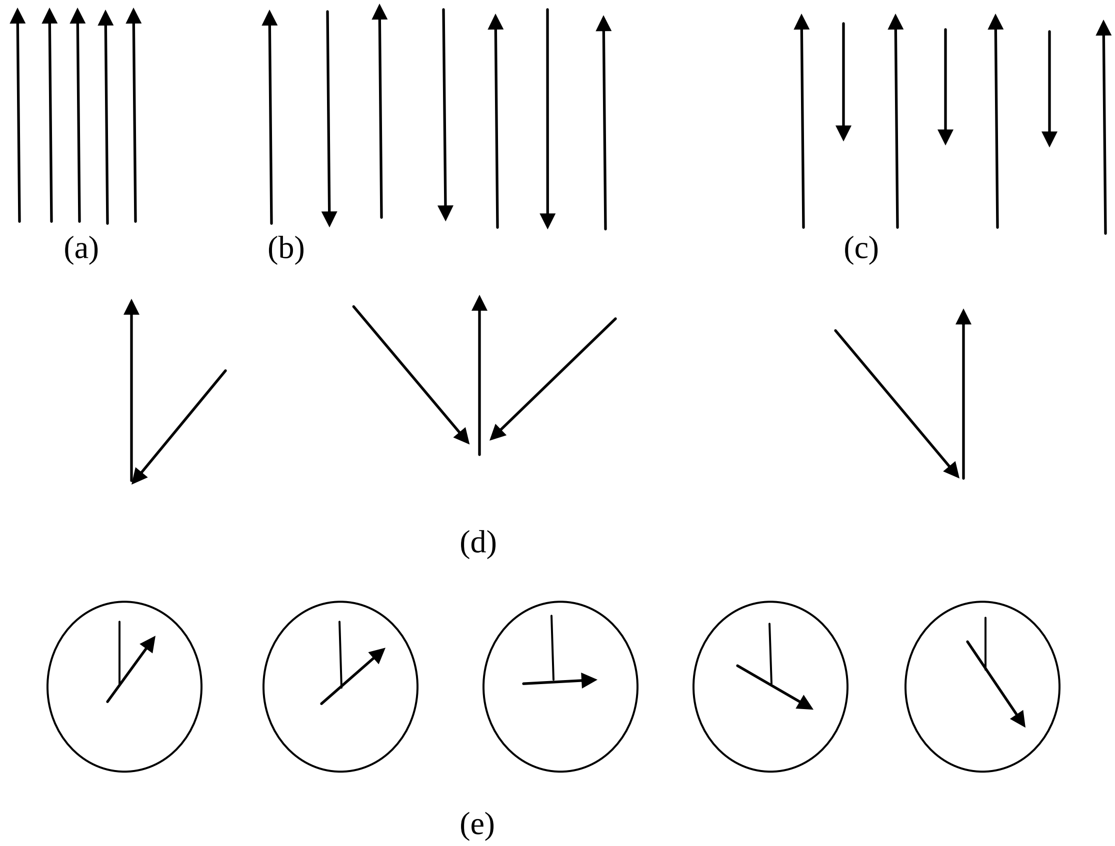

Figure 2.2: Schematic representation of Some magnetic structures (a) ferromagnetic (b) antiferromagnetic, (c) ferrimagnetic (d) triangular or canted; and (e) helical (adapted from ref. [3]).

Ferrimagnetics also have a Curie point and one would expect the same type of paramagnetic behavior above the Curie temperature as shown in Fig. 2.3. However, because of the negative interaction such as found in antiferromagnetics, the curve of $1/\chi$ vs T will be concave approaching an asymptotic value which would extrapolate to a negative value which again was found in antiferromagnetics.

The onset of magnetic order in solids has two basic requirements:

(i) Individual atoms should have magnetic moments (spins),

(ii) Exchange interactions should exist that couple them together.

Magnetic moments originate in solids as a consequence of overlapping of the electronic wave function with those of neighboring atoms. This condition is best fulfilled by some transition metals and rare-earths. The exchange interactions depend sensitively upon the inter-atomic distance and the nature of the chemical bonds, particularly of nearest neighbor atoms. When the positive exchange dominates, which corresponds to parallel coupling of neighboring atomic moments (spins), the magnetic system becomes ferromagnetic below a certain temperature $T_C$called the Curie temperature. The common spin directions are determined by the minimum of magneto-crystalline anisotropy energy of the crystal.

Therefore, ferromagnetic substances are characterized by spontaneous magnetization. But a ferromagnetic material in the demagnetized state displays no net magnetization in zero field because in the demagnetized state a ferromagnetic of macroscopic size is divided into a number of small regions called domains, spontaneously magnetized to saturation value and the directions of these spontaneous magnetization of the various domains are such that the net magnetization of the specimen is zero.

The existence of domains is a consequence of energy minimization. The size and formation of these domains is in a complicated manner dependent on the shape of the specimen as well as its magnetic and thermal history. When negative exchange dominates, adjacent atomic moments align antiparallel to each other, and the substance is said to be anti-ferromagnetic below a characteristic temperature, T_N, called the Néel temperature.

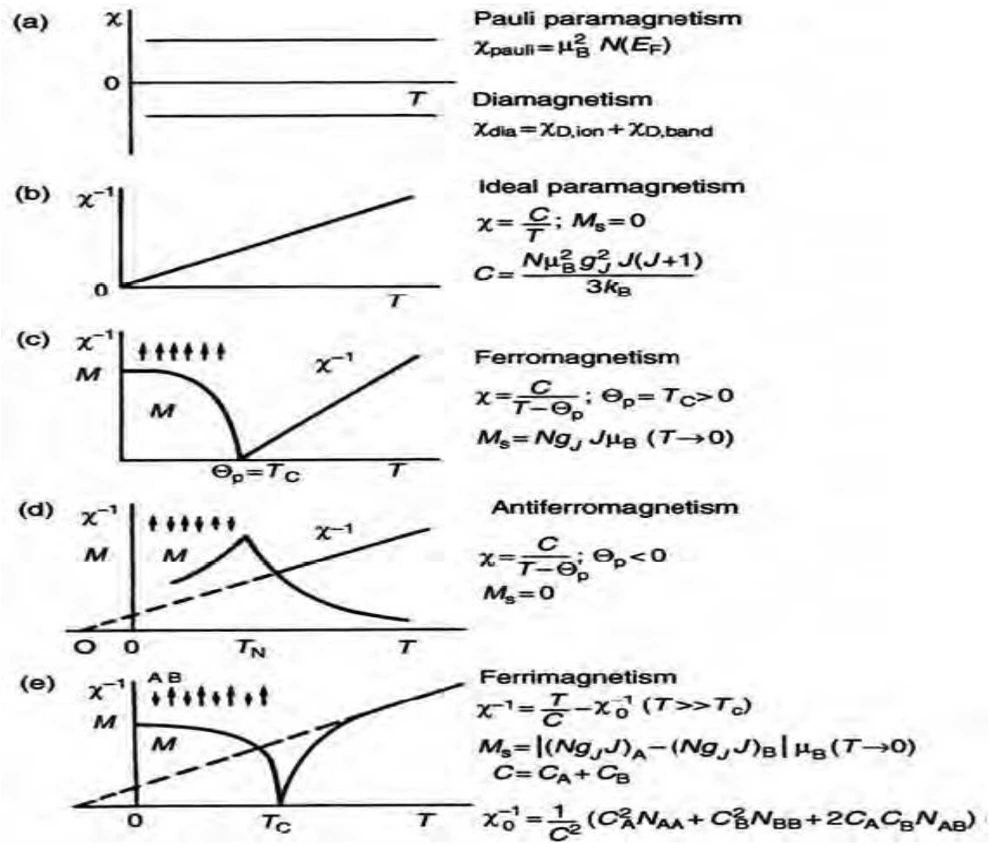

Figure 2.3: Summary of the temperature dependence of the magnetization M, the magnetic susceptibility χ or the reciprocal of susceptibility χ-1 in various types of magnetic materials (adapted from ref. [1]).

2.2.6 Néel theory of ferrimagnetism

If we consider the simplest case of a two-sub lattice system having antiparallel and non-equal magnetic moments, the inequality may be due to:

1) different elements in different sites,

2) same element in different ionic states, and

3) different crystalline fields leading to different effective moments for ions having the same spin.

The spins on one sub lattice are under the influence of exchange forces due to the spins on the second sub lattice as well as due to other spins on the same sub lattice. The molecular fields acting on the two sub lattices A and B can be written as [2, 5-6]

$$\vec{H}_A = \lambda_{AA}\vec{M}_A + \lambda_{AB}\vec{M}_B, \tag{2.7(a)}$$

$$\vec{H}_B = \lambda_{AB}\vec{M}_A + \lambda_{BB}\vec{M}_B \tag{2.7(b)}$$

are the magnetizations of the two sub lattices and λ's are the Weiss constants. Since the interaction between the sub lattices is antiferromagnetic, λ_{AB} must be negative, but λ_{AA} and λ_{BB} may be negative or positive depending on the crystal structure and the nature of the interacting atoms. Probably, these interactions are also negative, though they are in general quite small.

Assuming all the exchange interactions to be negative the molecular fields will be then given by

$$\vec{H}_A = -\lambda_{AA}\vec{M}_A - \lambda_{AB}\vec{M}_B, \tag{2.8(a)}$$

$$\vec{H}_B = -\lambda_{AB}\vec{M}_A - \lambda_{BB}\vec{M}_B \tag{2.8(b)}$$

Since in general, λ_{AA} and λ_{BB} are small compared to λ_{AB} , it is convenient to express the strengths of these interactions relative to the dominant λ_{AB} interaction.

Let $\lambda_{AA} = \alpha\lambda_{AB}$

and $\lambda_{BB} = \beta\lambda_{AB}$

In an external applied field $\vec{H}$, the fields acting on *A* and *B* sites are

$$\vec{H}_A = \vec{H} - \lambda_{AB}(\alpha\vec{M}_A - \vec{M}_B), \tag{2.9(a)}$$

$$\vec{H}_B = \vec{H} - \lambda_{AB}(\vec{M}_A - \beta\vec{M}_B) \tag{2.9(b)}$$

At temperatures higher than the transition temperature, T_N, $\vec{H}_A, \vec{M}_A$ *and* $\vec{M}_B$ are parallel and we can write,

$$\vec{M}_A = \frac{C_A}{T}[\vec{H} - \lambda_{AB}(\alpha\vec{M}_A - \vec{M}_B)] \tag{2.10(a)}$$

$$\vec{M}_B = \frac{C_B}{T}[\vec{H} - \lambda_{AB}(\vec{M}_A - \beta\vec{M}_B)] \tag{2.10(b)}$$

where $C_A$and $C_B$are the Curie constants for the two sub lattices.

and

$$C_A = N_A g\mu^2{}_B S_A(S_A+1)/3K \tag{2.11(a)}$$

$$C_B = N_B g\mu^2{}_B S_B(S_B+1)/3K \tag{2.11(b)}$$

$N_A$and $N_B$denote the number of magnetic ions on Aand B sites respectively and $S_A$and $S_B$are their spin quantum numbers. Solving for the susceptibility, χ , one gets [2, 5]

$$\begin{aligned}\frac{1}{\chi} &= \frac{T}{C} - \frac{1}{\chi_0} - \frac{b}{T-\theta}\\ \frac{1}{\chi} &= \frac{T+(C/\chi_0)}{C} - \frac{b}{T-\theta}\end{aligned} \tag{2.12}$$

Where C, χ_0 , b and θ are constants for particular substance and are given by

$$C = C_A + C_B$$

$$\frac{1}{\chi_0} = -\frac{1}{C^2}[C_A{}^2\lambda_{AA} + C_B{}^2\lambda_{BB} + 2C_AC_B\lambda_{AB}]$$

$$b = \frac{C_AC_B}{C^3}[C_A{}^2(\lambda_{AA} - \lambda_{BB})^2 + C_B{}^2(\lambda_{BB} - \lambda_{AB})^2 - 2C_AC_B\{\lambda_{AB}{}^2 - (\lambda_{AA} + \lambda_{BB})\lambda_{AB} + \lambda_{AA}\lambda_{BB}\}]$$

$$\theta = -\frac{C_AC_B}{C}(\lambda_{AB} + \lambda_{BB}) - 2\lambda_{AB}$$

Equation (2.5) represents a hyperbola, and the physically meaning part of it is plotted in fig. 2.3. This curvature of the plot of 1/χ versus T is a characteristic feature of a ferrimagnet. It cuts the temperature axis at T_C, called the Ferrimagnetic Curie point. At high temperatures the last term of equation (2.5) become negligible, and reduces to a Curie-Weiss law:

$$\chi = \frac{C}{T + (C / \chi_0)} \tag{2.13}$$

This is the equation of straight line, shown dashed in Fig. 2.4, to which the $1/\chi$ versus T curve becomes asymptotic at high temperatures.

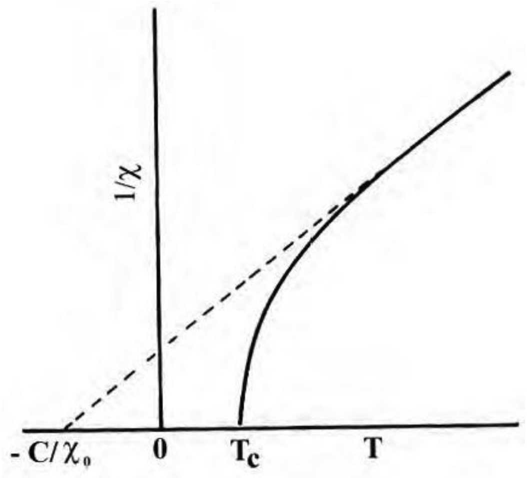

Figure 2.4: The temperature dependence of the inverse susceptibility for ferrimagnets (adapted from ref. [3]).

The Ferrimagnetic Curie Temperature $T_C$is obtained from equations (2.3) and (2.4) with $H = 0$ and setting the determinant of the coefficients of $M_i$equal to zero. This gives,

$$T_C = \frac{1}{2}[C_A\lambda_{AA} + C_B\lambda_{BB} + \{(C_A\lambda_{AA} - C_B\lambda_{BB})^2 + 4C_AC_B\lambda_{AB}{}^2\}^2] \tag{2.14}$$

Equation (2.5) is in good agreement with the experiment, except near the Curie point. The experimental Curie temperature, the temperature at which the susceptibility becomes infinite and spontaneous magnetization appears, is lower than the theoretical Curie temperature [1, 2, and 6]. This disagreement between theory and experiment in the region of Curie point is presumably due to the short-range spin order (spin clusters) at temperatures above experimental T_C[6].

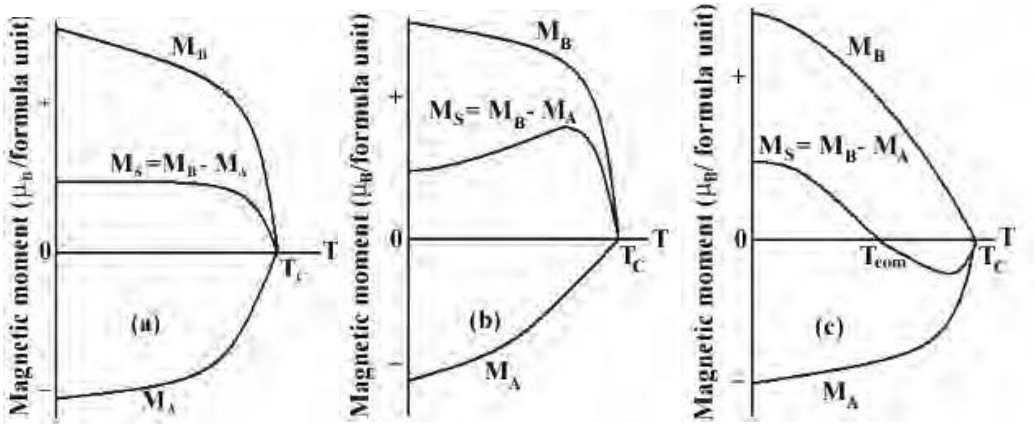

Figure 2.5: Superposition of various combinations of two opposing sub lattice magnetizations producing differing resultants including one with compensation point (schematic) (adapted from ref. [3]).

The sub lattice magnetizations will in general have different temperature dependences because the effective molecular fields acting on them are different. This suggests the possibility of having anomaly in the net magnetization versus temperature curves, Fig. 2.5. For most ferrimagnets the curve is similar to that of ferromagnets, but in a few cases there be a compensation point in the curve, Fig. 2.5(c) [2]. At a point below the Curie temperature point, the two sub lattice magnetizations are equal and thus appear to have no moment. This temperature is called the compensation point. Below this temperature one sub lattice magnetization is larger and provides the net moment. Above this temperature the other magnetization does dominate and the net magnetization reverses direction.

The essential requisite for Néel configuration is a strong negative exchange interaction between *A* and *B* sub lattices which results in their being magnetized in opposite directions below the transition point. But there may be cases where intra sub lattice interactions are comparable with inter sub lattice interaction. Neel's theory predicts paramagnetism for such substances at all temperatures. This is unreasonable since strong *AA* or *BB* interaction may lead to some kind of ordering especially at low temperature. In the cases of no *AB* interaction, antiferromagnetic ordering may be expected either in the *A* or in the *B* sub lattice. Under certain conditions there may be non-collinear spin arrays of still lower energy.

2.2.7 History of ferrite materials

Ferrites are extensively studied materials because of their interesting physical, structural and magnetic properties. For the first time, S. Hilpert described the usefulness of ferrites at high frequency [7]. Ferrites were fabricated into commercially useful magnetic material during 1933 by Snoek [8]. At the same time Takai in 1937 in Japan was seriously engaged in the research work on the same materials [9]. Neel established theoretical treatment on ferrite [6]. We can achieve a brief history of the development of ferrites in books by Gorter [10]. Now a day’s many researchers are trying to enhance the magnetic properties of ferrites.

Very high permeability is restricted to certain temperature ranges and the shapes of permeability versus temperature curves are strongly affected by any inhomogeneity in the ferrite structure as shown by Roess [11]. High permeability is certainly affected by the microstructure of the ferrites. The sintering process plays a dominant role in many magnetic properties of ferrites.

Both the sintering density and the average grain size increased with sintering temperature as reported by Nakamura [12] and Tasaki *et al.* [13].

2.2.8 Spinel structure of ferrites

The spinel ferrites are a large group of oxides which possess the structure of the natural spinel $MgAl_2O_4$. Spinels are predominantly ionic. The particular sites occupied by cations are, however, influenced by several other factors, including covalent bonding effects (e.g- Zn in tetrahedral sites) and crystal field stabilization energies of transition-metal cations. Many different cation combinations may form a spinel structure; it is almost enough to combine any three cations with a total charge of eight to balance the charge of the anions [1]. The most important spinels from the magnetic point of view are the $MeO.Fe_2O_3$or $MeFe_2O_4$where Me is the divalent metal ion [3].

Ferrites have the cubic structure, which is very close to that of the mineral spinel $MgO.Al_2O_3$, and are called cubic spinel. Analogous to the mineral spinel, magnetic spinel has the general formula $MeO.Fe_2O_3$or $MeFe_2O_4$where Me is the divalent metal ion [14].

This crystal structure was first determined by Bragg and by Nishikawa [3, 5]. Formerly, spinels containing *Fe* were called ferrites but now the term has been broadened to include many other ferrimagnets including garnets and hexagonal ferrites these need not necessarily contain iron. The spinel lattice is composed of a close-packed oxygen (radius about 1.3Å) arrangement in which 32 oxygen ions form a unit cell that is the smallest repeating unit in the crystal network.

The unit cell of the ideal spinel structures is given in Fig. 2.6. Between the layers of oxygen ions, if we simply visualize them as spheres, there are interstices that may accommodate the metal ions (radii ranging from 0.6 to 0.8 Å). Now, the interstices are not all the same: some which we call A sites are surrounded by or coordinated with 4 nearest neighboring oxygen ions whose lines connecting their centers form a tetrahedron. Thus, *A* sites are called tetrahedral sites. The other type of sites (*B* sites) is coordinated by 6 nearest neighbor oxygen ions whose center connecting lines describe an octahedron. The *B* sites are called octahedral sites. In the unit cell of 32 oxygen ions there are 64 tetrahedral sites and 32 octahedral sites. If all these were filled with metal ions, of either +2 or +3 valences, the positive charge would be very much greater than the negative charge and so the structure would not be electrically neutral. It turns out that of the 64 tetrahedral sites, only 8 are occupied and out of 32 octahedral sites, only 16 are occupied. Thus the unit cell contains eight formula units AB_2O_4, with 8 *A* sites, 16 *B* sites and 32 oxygen ions, and total of 8 x 7 =56 ions. A spinel unit cell contains two types of subcells, Fig. 2.6. These two types of subcells alternate in a three-dimensional array so that each fully repeating unit cell require eight subcells, Fig. 2.7. The positions of the ions in the spinel lattice are not perfectly regular (as the packing of hard spheres) and some distortion does occur. The tetrahedral sites are often too small for the metal ions so that the oxygen ions move slightly to accommodate them. The oxygen ions connected with the octahedral sites move in such a way as to shrink the size the octahedral cell by the same amount as the tetrahedral site expands. The movement of the tetrahedral oxygen is reflected in a quantity called the oxygen parameter, which is the distance between the oxygen ion and the face of the cube edge along the cube diagonal of the spinel subcell. This distance is theoretically equal to $3/8a_0$where $a_0$is the lattice constant.

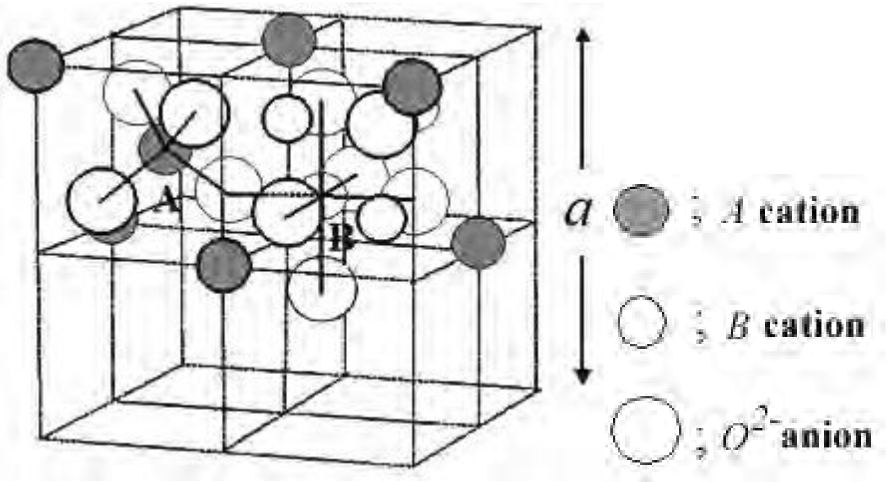

Figure 2.6: Two subcells of a unit cell of the spinel structure [15].

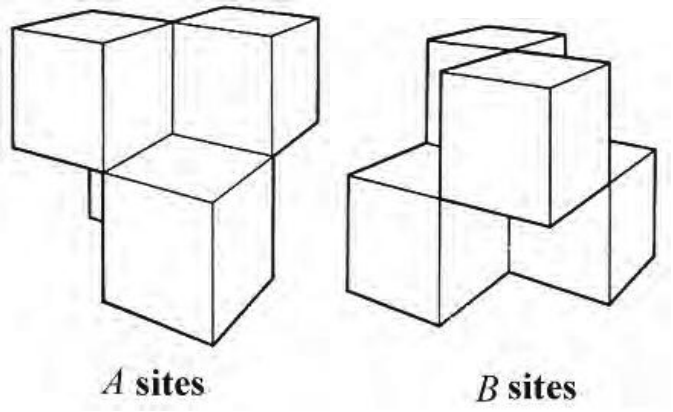

Figure 2.7: Unit cell of spinel ferrite divided into eight subcells with *A* and *B* sites (adapted from ref. [3]).

2.2.9 Cation distribution of spinel ferrites

In spinel structure the distribution of cations over the tetrahedral or *A* sites and octahedral or *B* sites can be present in a variety of ways. If all the Me_{2+}ions in $Me^{2+}Me_2^{3+}O_4$ are in tetrahedral and all Me^{3+}ions in octahedral positions, the spinel is then called normal spinel. Another cation distribution in spinel exists, where one half of the cations $Me^{3+}$are in the *A* positions and the rest, together with the Me^{3+}ions are randomly distributed among the *B* positions. The spinel having the latter kind of cation distribution is known as inverse spinel. The distribution of these spinels can be summarized as [3, 16, and 17]:

1) Normal spinels, i.e. the divalent metal ions are on *A*-sites: $Me^{2+}[Me_2{}^{3+}]O_4$

2) Inverse spinels, i.e. the divalent metal ions are on *B*-sites: $Me^{3+}[Me^{2+}Me_2{}^{3+}]O_4$

A completely normal or inverse spinel represents the extreme cases. *Zn* ferrites have normal spinel structure and its formula may be written as $Zn^{2+}[Fe^{3+}Fe^{3+}]O_4{}^{2-}$.On the other hand, *Ni* ferrites have inverse spinel structure and its formula may be written as $Fe^{3+}[Ni^{2+}Fe^{3+}]O_4{}^{2-}$.

There are many spinel oxides which have cation distributions intermediate between these two extreme cases and are called mixed spinels. The general cation distribution for the spinel can be indicated as:

$$(Me_x{}^{2+}Me_{1-x}{}^{3+})[Me_{1-x}{}^{2+}Me_{1+x}{}^{3+}]O_4$$

where the first and third brackets represent the A and B sites respectively. For normal spinel x=1, for inverse spinel x=0. The quantity x is a measure of the degree of inversion. In the case of some spinel oxides x depends upon the method of preparation.

The basic magnetic properties of the ferrites are very sensitive functions of their cation distributions. Mixed ferrites having interesting and useful magnetic properties are prepared by mixing two or more different types of metal ions. The chemical formula of mixed *Ni-Zn* ferrite may be written as $(Zn_x{}^{2+}Fe_{1-x}{}^{3+})[Ni_{1-x}{}^{2+}Fe_{1+x}{}^{3+}]O_4{}^{2-}$.

Spinel oxides are ionic compounds and hence the chemical bonding occurring in them can be taken as purely ionic to a good approximation. The total energy involved, however, consists of the Coulomb energy, the Born repulsive energy, the polarization and the magnetic interaction energy. The energy terms are all dependent on lattice constant, oxygen position parameter and the ionic distribution. In principle the equilibrium cation distribution can be calculated by minimizing the total energy with respect to these variables.

But the only energy that can be written with any accuracy is the Coulomb energy. The individual preference of some ions for certain sites resulting from their electronic configuration also play an important role. The divalent ions are generally larger than the trivalent (because the larger charge produces greater electrostatic attraction and so pulls the outer orbits inward).

The octahedral sites are also larger than the tetrahedral. Therefore, it would be reasonable that the trivalent ions Fe^{3+}(0.67Å) would go into the tetrahedral sites and the divalent ions Fe^{2+}(0.83Å) go into the octahedral. Two exceptions are found in $Zn^{2+}$and Cd^{2+}which prefer tetrahedral sites because the electronic configuration is favorable for tetrahedral bonding to the oxygen ions. Thus Zn^{2+}(0.82Å) prefer tetrahedral sites over the Fe^{3+}(0.67Å) ions. $Zn^{2+}$and Co^{2+}have same ionic radius but *Zn* prefers tetrahedral sites and *Co* prefers octahedral sites because of the configuration exception. Ni^{2+}(0.78Å) and Cr^{3+}(0.64Å) have strong preferences for octahedral sites [3, 5]. Hence the factors influencing the distribution of cations among the two possible lattice sites are mainly their ionic radii of the specific ions, the size of the interstices, temperature, the matching of their electronic configuration to the surrounding anions and the electrostatic energy of the lattice, the so-called Madelung energy, which has the predominant contribution to the lattice energy under the constrain of overall energy minimization and charge neutrality.

2.2.10 Canting effect in spinel ferrites

The magnetic structure of Ni ferrite, $NiFe_2O_4$, is that of two opposing magnetic sublattices A (tetrahedral sites) and B (octahedral sites), in which the magnetic ions are all coupled antiferromagnetically [18]. The A-B coupling is the strongest and dominates the interactions. There are more B sites than A sites so the net magnetization is simply the difference between the B sub lattice magnetization and the A sub lattice magnetization. The crystalline structure of Ni ferrite is the inverted spinel, where the A sub lattice contains half of the Fe^{3+}ions and the other half together with all the Ni^{2+}ions are in the B sub lattice. Zn ferrite belongs to the 'normal' type of spinels, that is, all the Zn^{2+}ions are in A sites. In a mixed Ni-Zn ferrite, $Zn_xNi_{1-x}Fe_{1-x}O_4$(x being the Zn content per formula unit), the Zn^{2+}ions stay in A sites and the Ni^{2+}ions in B sites [15]. When the Fe^{3+}ions concentration in the A sub lattice is diluted by low concentrations of diamagnetic substitutions (like Zn^{2+}), the net magnetization increases. However, at higher doping levels, a decrease in magnetization occurs. The reason for this is that low Zn concentrations lead to a decrease in the number of spins occupying the A sub lattice causing an increase of the net magnetization. As the Zn content is increased the exchange interactions are weakened and the B spins are no longer held rigidly parallel to the few remaining A spins. The decrease in the B-sub lattice moment, interpreted as a spin departure from collinearity, causes the effect known as *canting*.

Having in mind previous results of Dionne [19], in the present work it is considered that there are two octahedral sub lattices B and B', and only B' is affected by the canting effect. It is assumed that the B' sub lattice is formed only by the nearest neighbors to the A sites which have been occupied by Zn^{2+}ions. In this way the amount of B' sites will increase with higher *z* values. The spins will be canted from the direction of net magnetization an angle θ, forming an angle of 2θ between them, as depicted in fig. 2.8.

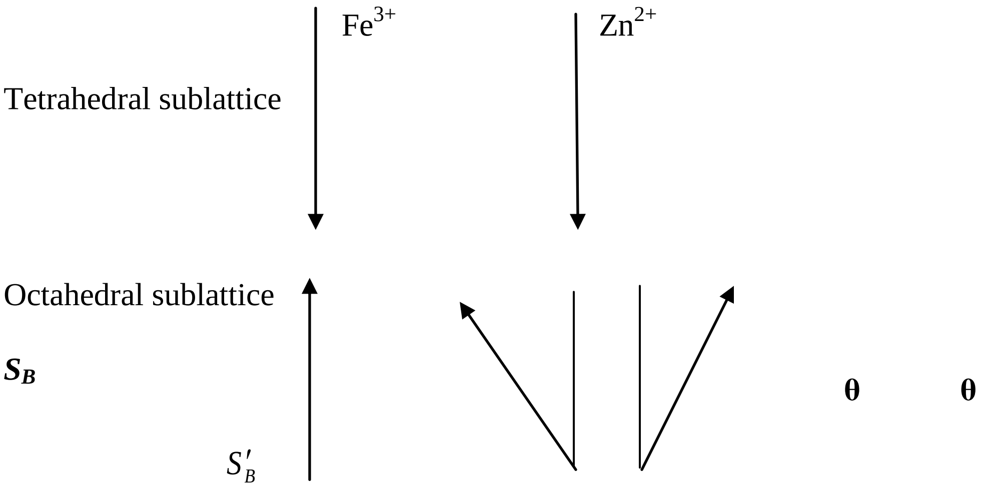

Figure 2.8 Model spin consideration of a Zn substituted ferrites.

Two cases are studied:

(i) *B' is occupied only by Fe^{3+}ions:* As Zn^{2+}ions replace Fe^{3+}ions in A sites it can be argued that, in order to locally keep the total charge neutral, all the ferric ions that had been displaced will tend to stay near the Zn^{2+}ions that have taken their place. In this way, $B^{/}$sites will be occupied by Fe^{3+}ions. In this case it is considered that all B' sites have ferric ions; therefore, in sub lattice B there will be equal proportion of $Fe^{3+}$and Ni^{2+}.

(ii) $B_{/}$ is occupied by $Fe^{3+}$and $N^{2+`}$ ions: It can be thought that all the ions in octahedral sites which are nearest-neighbors of Zn ions keep an 'average character', so B' sites are occupied by $Fe^{3+}$and Ni^{2+}ions in the proportion given by the average composition of the ferrite.

Geller [20] proposed a localized canting approach, in which individual moments on one sub lattice are canted at different angles, depending on the specifics of the local magnetic environment. Patton *et al.* [21] provided a mathematical formulation of random localized canting, starting from a nearest-neighbor Heisenberg-Hamiltonian. The model spin configuration of a Zn-substituted ferrite is shown in fig. 2.8.

The number of Bohr magnetons per formula unit, $n_B$as a function of Zn content can then be expressed for T= 0 K in the following way $n_B= M_B\text{Cos}\theta_{Y\text{-}K}- M_{A.}$

The expressions are for cases (i) and (ii), and for comparison the case was included in which there are only two sub lattices, A and B, and the entire sub lattice B is affected by canting [22].

2.2.11 Interaction between magnetic moments on lattice sites

Spontaneous magnetization of spinels (at 0K) can be estimated on the basis of their composition, cation distribution, and the relative strength of the possible interaction. Since cation-cation distances are generally large, direct (ferromagnetic) interactions are negligible.

Because of the geometry of orbital involved, the strongest super exchange interaction is expected to occur between octahedral and tetrahedral cations.

The strength of interaction or exchange force between the moments of the two metal ions on different sites depends on the distances between these ions and the oxygen ion that links them and also on the angle between the three ions. The nearest neighbors of a tetrahedral, an octahedral and an anion site are shown in fig. 2.9. The interaction is greatest for an angle of 180° and also where the interionic distances are the shortest. fig. 2.10 shows the interionic distances and the angles between the ions for the different type of interactions.

In the *A-A* and *B-B* cases, the angles are too small or the distances between the metal ions and the oxygen ions are too large. The best combination of distances and angles are found in *A-B* interactions.

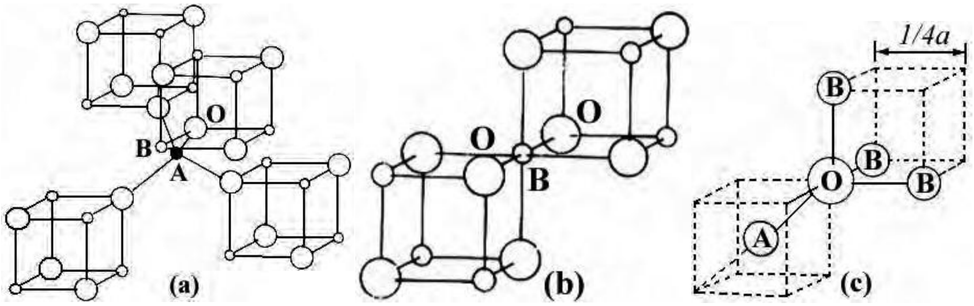

Figure 2.9: Nearest neighbours of (a) a tetrahedral site, (b) an octahedral site and (c) an anion site (adapted from ref. [15]).

For an undistorted spinel, the *A-O-B* angles are about $125^0$and 154^0[2, 3, and 14]. The *B-O-B* angles are $90^0$and 125^0but the latter, one of the *B-B* distances is large. In the *AA* case the angle is about 80^0. Therefore, the interaction between moments on the *A* and *B* site is strongest. The *BB* interaction is much weaker, and the most unfavorable situation occurs in the *AA* interaction. By examining the interaction involving the major contributor, or the *A-B* interaction which orients the unpaired spins of these ions antiparallel, Néel was able to explain the ferrimagnetism of ferrites [6].

2.2.12 Magnetism in spinel ferrite

The magnetic moment of a free atom is associated with the orbital and spin motions of electrons in an incomplete sub-shell of the electronic structure of the atom. In crystals the orbital motions are quenched, that is the orbital planes may be considered to be fixed in space relative to the crystal lattice, and in such a way that in bulk the crystal has no resultant moment from this source. Moreover, this orbital-lattice coupling is so strong that the application of a magnetic field has little effect upon it. The spin axes are not tightly bound to the lattice as are the orbital axes.

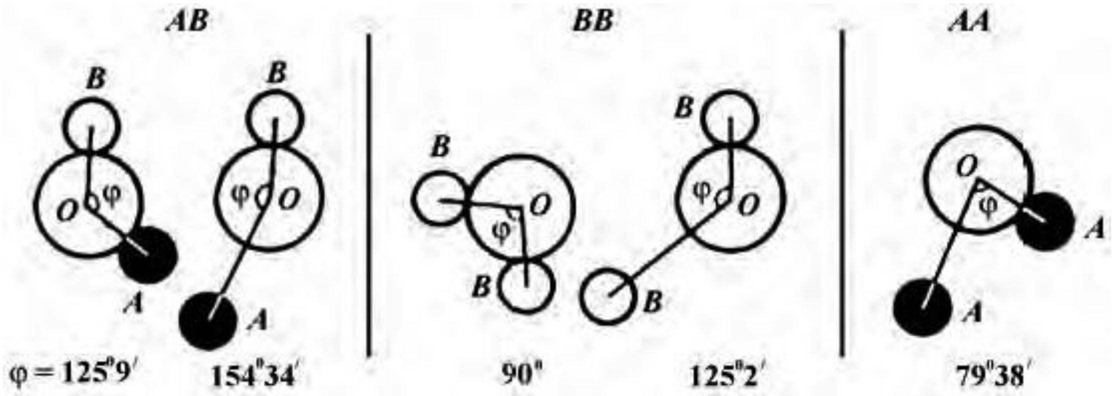

Figure 2.10: Interionic angles in the spinel structure for the different type of lattice site interactions (adapted from ref. [15]).

The anions surrounding a magnetic cation subject it to a strong inhomogeneous electric field and influence the orbital angular momentum. However, the spin angular momentum remains unaffected. For the first transition group elements this crystal field effect is intense partly due to the large radius of the 3d shell and partly due to the lack of any outer electronic shell to screen the 3d shell whose unpaired electrons only contribute to the magnetic moment. We have originally defined the magnetic moment in connection with permanent magnets. The electron itself may well be called the smallest permanent magnet [2]. For an atom with a resultant spin quantum number *S*, the spin magnetic moment will be

$$\mu = g\,S(S+1)\mu_B, \qquad (2.15)$$

where g is the Landé splitting factor and μ_B, known as the Bohr magneton, is the fundamental unit of magnetic moment. The value of g for pure spin moment is 2 and the quantum number associated with each electron spin is ± 1/2. The direction of the moment is comparable to the direction of the magnetization (from South to North poles) of a permanent magnet to which the electron is equivalent. Fig.2.11 illustrates the electronic configuration of Fe atoms and Fe^{3+} ions. Fe atom has four unpaired electrons and Fe^{3+} ion has five unpaired electrons. Each unpaired electron spin produced 1 Bohr magneton. In compounds, ions and molecules, account must be taken of the electrons used for bonding or transferred in ionization. It is the number of unpaired electrons remaining after these processes occur that gives the net magnetic moment [1]. According to the Hund‘s rules the moment of Fe atom and Fe^{3+}ion are $4\mu_B$and $5\mu_B$respectively. Similarly, the moment of $Fe^{2+}$and Ni^{2+}ion is $4\mu_B$and $2\mu_B$respectively.

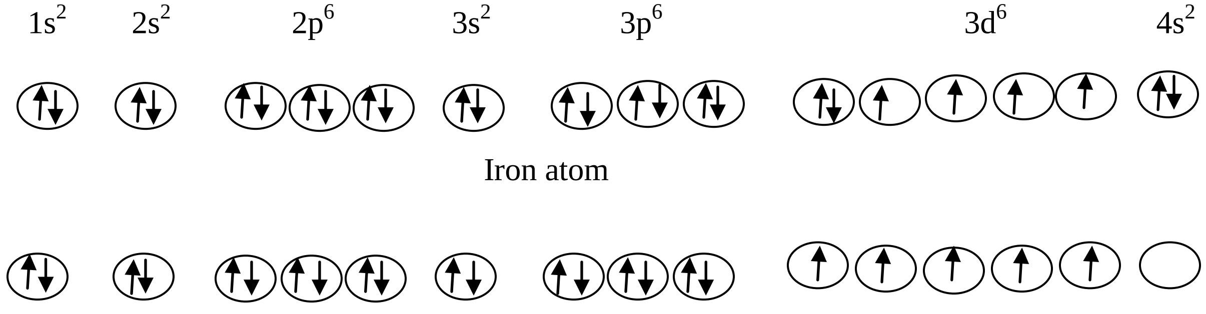

Figure 2.11: Electronic configuration of atoms and ions (adapted from ref. [2]).

Fe^{3+} Ion

2.2.13 Super exchange interactions in spinel

The intense short-range electrostatic field, which is responsible for the magnetic ordering, is the exchange force that is quantum mechanical in origin and is related to the overlapping of total wave functions of the neighboring atoms. The total wave function consists of the orbital and spin motions. Usually the net quantum number is written as *S*, because the magnetic moments arise mostly due to the spin motion as described above. The exchange interactions coupling the spins of a pair of electrons are proportional to the scalar product of their spin vectors [14, 17, and 23],

$$V_{ij} = -2J_{ij}\,\mathbf{S}_{i}..\mathbf{S}_{j} \qquad (2.16)$$

where J_{ij} is the exchange integral given in a self-explanatory notation by

$$J_{ij} = \int \psi_i^*(1)\psi_j^*(2)\left[\frac{1}{r_{12}} + \frac{1}{r_{ij}} - \frac{1}{r_{i1}} - \frac{1}{r_{j2}}\right]\psi_i(2)\psi_j(2)dv_1dv_2 \qquad (2.17)$$

In this expression r's are the distances, subscripts *i* and *j* refer to the atoms, 1 and 2 refers to the two electrons. If the *J* in equation (1) is positive, we achieve ferromagnetism. A negative *J* may give rise to anti-ferromagnetism or ferrimagnetism.

Magnetic interactions in spinel ferrites as well as in some ionic compounds are different from the one considered above because the cations are mutually separated by bigger anions (oxygen ions). These anions obscure the direct overlapping of the cation charge distributions, sometimes partially and sometimes completely making the direct exchange interaction very weak. Cations are too far apart in most oxides for a direct cation-cation interaction. Instead, super exchange interactions appear, i.e., indirect exchange via anion *p*-orbitals that may be strong enough to order the magnetic moments. Apart from the electronic structure of cations this type of interactions strongly depends on the geometry of arrangement of the two interacting cations and the intervening anion. Both the distance and the angles are relevant. Usually only the interactions with in first coordination sphere (when both the cations are in contact with the anion) are important. In the Neél theory of ferrimagnetism the interactions taken as effective are inter- and intra-sub lattice interactions *A-B*, *A-A* and *B-B.* The type of magnetic order depends on their relative strength.

The superexchange mechanism between cations that operate via the intermediate anions was proposed by Kramer for such cases and was developed by Anderson [24]. A simple example of super exchange is provided by *MnO* which was chosen by Anderson. From the crystal structure of *MnO* it will be seen that the antiparallel manganese ions are collinear with their neighboring oxygen ions. The O^{2-}ions each have six $2p$ electrons in three antiparallel pairs. The outer electrons of the Mn^{2+}ions are in $3d$ sub-shells which are half filled with five electrons in each. The phenomenon of super exchange is considered to be due to an overlap between the manganese $3d$ orbits and the oxygen $2p$ orbits with a continuous interchange of electrons between them. It appears that, for the overall energy of the system to be a minimum, the moments of the manganese ions on either side of the oxygen ion must be antiparallel. The manganese magnetic moments are thus, in effect, coupled through the intervening oxygen ion. The idea is illustrated in fig. 2.12.

In figs. 2.12(a) and 2.12(c) the outer electrons in a pair of Mn^{2+}ions, and in an intervening O^{2-}ion in the unexcited state, are shown by the arrows. One suggested mode of coupling is indicated in Fig. 2.12(b). The two electrons of a pair in the oxygen ion are simultaneously transferred, one to the left and the other to the right. If their directions of spin are unchanged then, by Hund‘s rules, the moments of the two manganese ions must be antiparallel as shown. Another possibility is represented in Fig. 2.12(d). One electron only has been transferred to the manganese ion on the left. The oxygen ion now has a moment of $1\mu_B$ and if there is negative interaction between the oxygen ion and the right-hand manganese ion then again the moments of the manganese ions will be antiparallel. If these ideas are accepted, then the oxygen ions play an essential part in producing antiferromagnetism in the oxide. Moreover, because of the dumbbell shape of the $2p$ orbits, the coupling mechanism should be most effective when the metal ions and the oxygen ions lie in one straight line, that is, the angle between the bonds is 180°, and this is the case with MnO.

In the case of spinel ferrites, the coupling is of the indirect type which involves overlapping of oxygen wave functions with those of the neighboring cations.

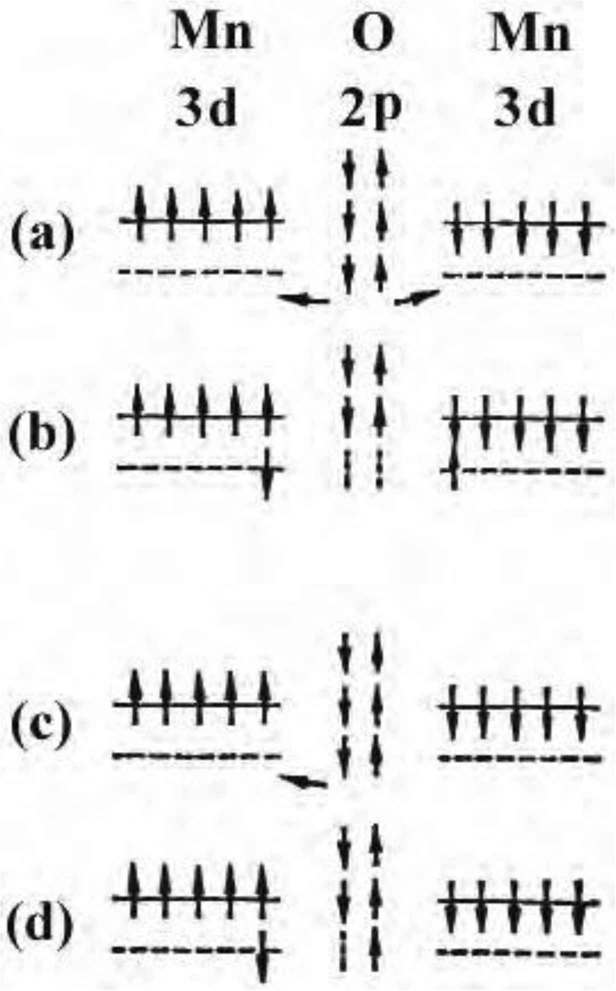

Figure 2.12: Illustrating super exchange in MnO (adapted from ref. [3]).

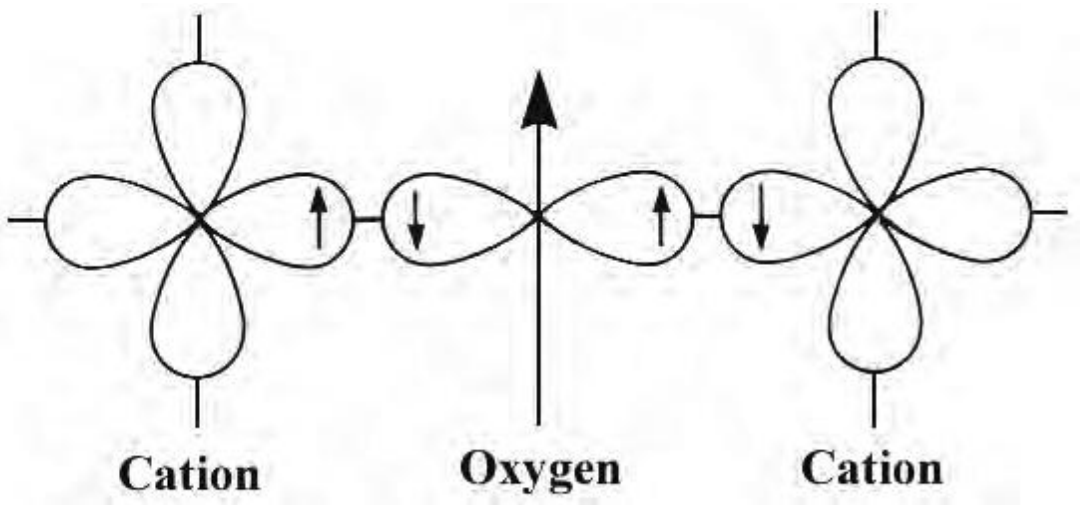

Figure 2.13: Schematic representation of the super exchange interaction in the magnetic oxides. The p orbital of an anion (center) interact with the d orbitals of the transitional metal cations (adapted from ref. [3]).

Consider two transition metal cations separated by an *O*, Fig. 2.13. The O^{2-}has no net magnetic moment since it has completely filled shells, with *p*-type outermost orbitals. Orbital $p_x$has two electrons: one with spin up, and the other with spin down, consistent with pauli‘s exclusion principle. The essential point is that when an oxygen *p* orbital overlaps with a cation *d* orbital, one of the *p* electrons can be accepted by the cations. When one of the transition metal cations is brought close the O^{2-}, partial electron overlap (between a *3d* electron from the cation and a *2p* electron form the O^{2-}) can occur only for antiparallel spins, because electrons with the same spin are repelled. Empty *3d* states in the cation are available for partial occupation by the O^{2-}electron, with an antiparallel orientation. Electron overlap between the other cation and the O^{2-}then occurs resulting in antiparallel spins and therefore antiparallel order between the cations. Since the *p* orbitals are linear, the strongest interaction is expected to take place for *cation*– O^{2-}– *cation* angles close to 180^0 [2].

2.2.14 Magnetic moments in spinel ferrites

Fe_3O_4has a ferromagnetic property because of its inverse structure which leads to the formation of domains. A unit cell of Fe_3O_4contains eight formula units each of which may be written in the $Fe^{3+}[Fe^{2+}Fe^{3+}]O_4^{2-}$[16]. Snoek and his co-workers found that oxides of inverse structure could be artificially produced in which the divalent ions of another element, for example *Mn*, *Ni*, *Co*, *Mg* or *Cu*, could be substituted for the divalent Fe_{2+} ions in Fe_3O_4. An extensive range of ferrites could thus be made having the general formula $- \vec{Fe}^{3+}[\overleftarrow{M}^{2+}\overleftarrow{Fe}^{3+}]O_4{}^{2-}$, where arrows indicate spin ordering. Since the trivalent iron ions are equally distributed on *A* and *B* sites they cancel each other out magnetically, and the magnetic moment per formula unit is then theoretically the same as the magnetic moment of the divalent ion. The *Ni* ferrite has a moment of $2.3\mu_B$compared with a theoretical value of $2\mu_B$ [2]. *Zn* ferrite is a normal spinel, with Zn_{2+} ($3d_{10}$)ions in *A* sites have zero magnetic moment; Fe_{3+} ions in *B* sites have a magnetic moment $_B 5\mu$. The cation distribution can be written as $Zn^{2+}[\vec{Fe}^{3+}\overleftarrow{Fe}^{3+}]O_4$, where spin ordering is indicated by arrows. The zero magnetic moment of Zn^{2+}ions leaves trivalent iron ions on *B* sites with a negative *BB* interaction between equal ions. Therefore, *Zn* ferrite is not ferromagnetic. Zinc ferrite therefore be expected to be antiferromagnetic and thus to have a Néel point, though measurements show it to be paramagnetic only [1- 4, 16].

Magnetic properties can be modified widely by cation substitution. An illustrative case is substitution of *Ni* by *Zn* in *Co* ferrite to form solid solutions $Ni_{1-x}Zn_xFe_2O_4$. The cation distribution can be written as $(Zn_x{}^{2+}Fe_{1-x}{}^{3+})[Ni_{1-x}{}^{2+}Fe_{1+x}{}^{3+}]O_4{}^{2-}$ [2]. $Zn^{2+}$is diamagnetic and its main effect is to break linkages between magnetic cations. Another effect is to increase interaction distance by expanding the unit cell, since it has an ionic radius larger than the *Ni* and *Fe* radii. The most remarkable effect is that substitution of this diamagnetic cation (*Zn*) results in a significant increase in magnetic moment in a number of spinel solid solutions, Fig. 2.14. Magnetic moment as a function of *Zn* content shows an increase for small substitutions, goes through a maximum for intermediate values, decreases and finally vanishes for high *Zn* contents. A simple analysis shows that this increase can be expected for an antiparallel alignment. As the *Zn* content increases, magnetic moments decrease in sub lattice *A* and increase in sub lattice *B*. If the magnetic moment of *Fe* and *Ni* are 5 and ~2.3 μ_B/ion, respectively, then, per formula unit, the total moment in Bohr magnetons on *B* sub lattice is $2.3(1-x)+5(1+x)$ and on *A* sub lattice the total antiparallel moment is $5(1-x)$. If the resultant moment per formula unit is (0) M_S, then by taking the difference of *A* and *B* moments [16],

$$Ms(0)= 2.3(1-x)+5(1+x)-5(1-x)=x(10-2.3)+2.3$$

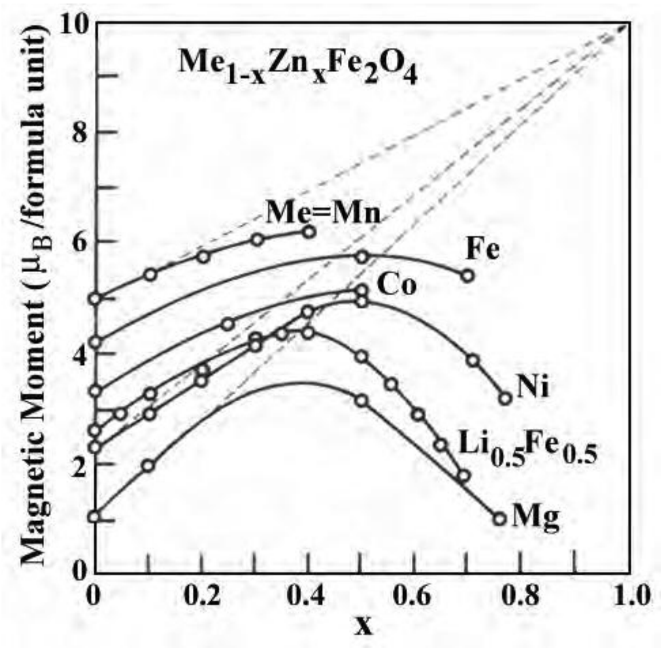

Figure 2.14: Variation of Magnetic moment (in Bohr magnetons per formula unit) with increasing zinc substitution (adapted from ref. [25]).

A linear relationship is obtained with a slope of 7.7, predicting a moment value of $_B$ 10μ per formula unit for *Zn* substitution *x* =1, as shown by the broken lines in Fig. 2.14. This relationship is not followed over the entire composition range. However, as the *Zn* content increases, *A–O–B* interactions become too weak and *B–O–B* interactions begin to dominate. That is, the average distance between the interacting spins gets larger. As a consequence, the system becomes frustrated causing a perturbation to the magnetically ordered spins as large number of *B* sites spins gets non-magnetic impurity atoms as their nearest neighbors.

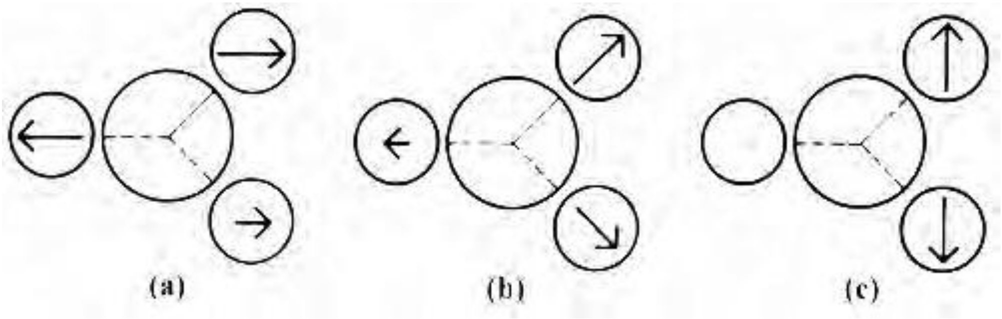

Figure 2.15: Schematic representation of spin arrangements in $Ni_{1-x}Zn_xFe_2O_4$; (a) ferrimagnetic (for $x \le 0.5$); (b) triangular or Yafet-Kittel (for $x > 0.5$); and (c) antiferromagnetic for $x \approx 1$(adapted from ref.[22]).

The *B* spins are no longer held in place due to this weak anti-ferromagnetic *A*-*B* interaction leading to non-collinearity or canting among the *B* sub lattice. Thus for $x > 0.5$ *Zn* content, instead of a collinear antiparallel alignment, canted structure appears, where spins in *B* sites are no longer parallel [2], Fig. 2.15. Evidence of this triangular structure has been observed by neutron diffraction [23]; a theoretical analysis showed that departure from collinear order depends on the ratio of the *A*–*O*– *B* to *B* –*O*– *B* molecular field coefficients, $\lambda_{AB} / \lambda_{BB}$ [22]. For high *Zn* concentration, *B* –*O*– *B* interactions dominant and the ferrite become antiferromagnetic for $x = 1$ [2].

2.3 Surface morphology of ferrites

2.3.1 Microstructures

A polycrystal is much more than many tiny crystals bonded together. The interfaces between the crystals, or the grain boundaries which separate and bond the grains, are complex and interactive interfaces. The whole set of a given materials properties (mechanical, chemical and especially electrical and magnetic) depend strongly on the nature of the microstructure. In the simplest case, the grain boundary is the region, which accommodates the difference in crystallographic orientation between the neighboring grains. For certain simple arrangements, the grain boundary is made of an array of dislocations whose number and spacing depends on the angular deviation between the grains. The ionic nature of ferrites leads to dislocation patterns considerably more complex than in metals, since electrostatic energy accounts for a significant fraction of the total boundary energy [3].

For soft ferrites, the grain boundaries influence the properties are [26-30]

1) creating a high resistivity inter granular layer,

2) acting as a sink for impurities which may act as a sintering aid and grain growth modifiers,

3) providing a path for oxygen diffusion, which may modify the oxidation state of cations near the boundaries.

Interfaces play a central role in sintering and any other diffusion phenomena; for instance, diffusion along grain boundaries can be 100 times faster than across them.

Interfaces are a common location for segregated second phases; in fact, grain boundaries in ceramics are more prone to segregation than their counterpart in metals because segregation can be promoted by electrostatic interactions). When segregation occurs, grain boundaries become Inhomogeneous, as their chemical composition is different from that of the grains.

The uniformity in the grain size and the average grain diameter can control properties such as the magnetic permeability. An undesirable effect of certain sintering conditions is the formation of the so-called duplex microstructure, where a very large grain is surrounded by smaller ones as shown in the fig. 2.17. When this occurs, the large grain has a high defect concentration.

In addition to grain boundaries, ceramic imperfections can impede domain wall motion and thus reduce the magnetic property. Among these are pores, cracks, inclusions, second phases, as well as residual strains. Imperfections also act as energy wells that pin the domain walls and require higher activation energy to detach. Stresses are microstructural imperfections that can result from impurities or processing problems such as too rapid a cool. They affect the domain dynamics and are responsible for a much greater share of the degradation of properties than would expect [1].

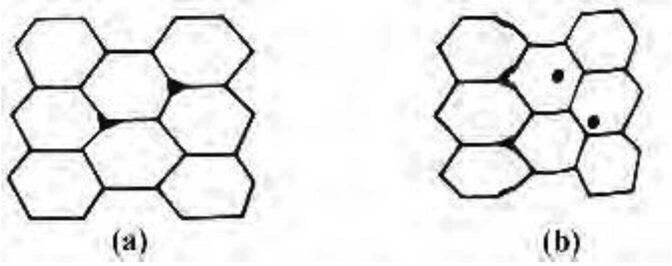

Figure 2.16: Porosity character: (a) intergranular, (b) intragranular (adapted from ref. [3]).

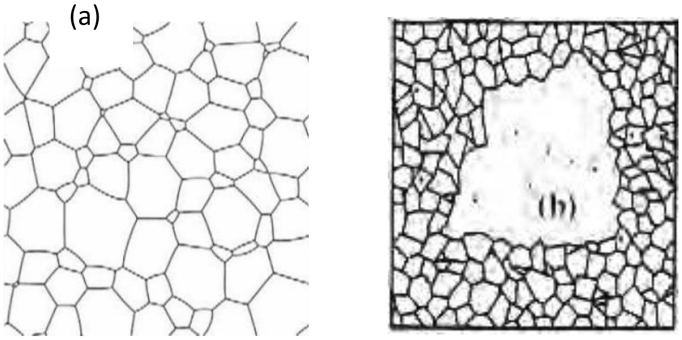

Figure 2.17: Grain growth (a) discontinuous, (b) duplex (schematic) (adapted from ref. [2]).

2.3.2 Sintering and grain formation

Sintering is defined as the process of obtaining a dense, tough body by heating a compacted powder for a certain time at a temperature high enough to significantly promote diffusion, but clearly lower than the melting point of the main component. The ideal sintering process results in a fully dense material by elimination of the porosity.

The driving force for sintering is the reduction in surface free energy of the powder. Part of this energy is transformed into interfacial energy (grain boundaries) in the resulting polycrystalline body. An important contribution to the understanding of sintering phenomena in the last few years has been the recognition of the role of surfaces and interfaces, which determine not only the macroscopic driving force, but also the microscopic diffusion mechanisms.

To obtain a dense, tough polycrystalline aggregate it is necessary to eliminate the voids between the particles of the ferrite and form grain boundaries. Although there is a continuous evolution of the microstructure during sintering, it is commonly divided into three stages,

Stage 1 Contact area between particles increases

Stage 2 Porosity changes from open to closed porosity

Stage 3 Pore volume decreases; grains grow

In the initial stage, neighboring particles form a neck by surface diffusion and presumably also at high temperatures by an evaporation- condensation mechanism, Fig. 2.18. Grain boundaries begin to form at the interface between particles with different crystallographic orientation. Pores appear as voids between at least three contacting particles. Shrinkage occurs.

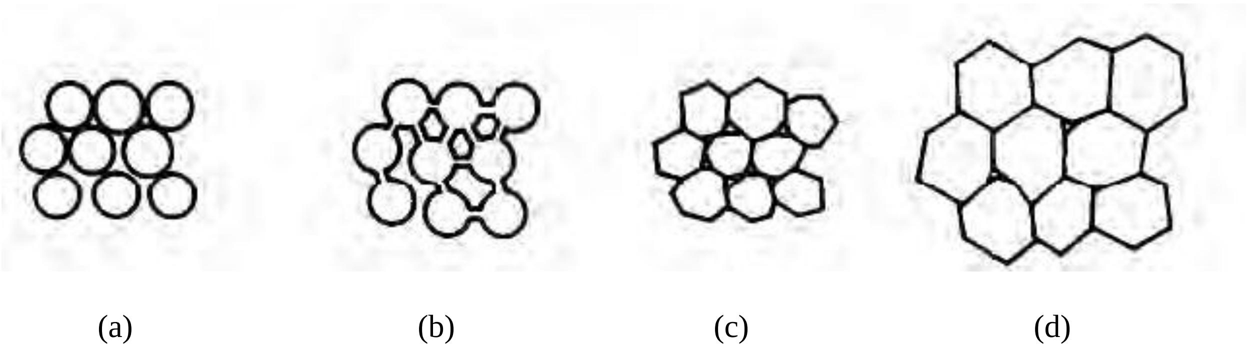

Figure 2.18: Schematic representation of sintering stages (a) green body, (b) initial stage, (c) intermediate stage, and (d) final stage (adapted from ref. [3]).

The second stage of sintering begins when a three-dimensional network of necks is achieved. During this stage, most of the densification occurs. To decrease and eventually eliminate pore volume, a net transport of material to the pores by volume diffusion is required. The mobility of the atoms (or ions) is greatly enhanced by the presence of lattice defect. The sintering mechanism involves creation of vacancies in the curved surfaces of pores, their transport through the grain and their absorption at grain boundaries, which play the role of sinks. Material transport in ionic compounds requires the simultaneous flux of both cations and anions to preserve both electro-neutrality and stoichiometry. The theory of sintering for ionic solids is more complex because of the constraints imposed by the electrical charges of the diffusing species. A difference in mobility between diffusing ions, for instance, gives rise to electric fields opposing the flux of fast species. Material transport is therefore controlled by the slowest diffusing species.

Grain growth begins during the intermediate stage of sintering. Since grain boundaries are the sinks for vacancies, grain growth tends to decrease the pore elimination rate due to the increase in distance between pores and grain boundaries, and by decreasing the total grain boundary surface area.

In the final stage, grain growth is considerably enhanced and the remaining pores may become isolated. When the grain growth rate is very high, pores may be left behind by rapidly moving grain boundaries, resulting in pores that are trapped inside the grains, and not between the grains. This intragrunular porosity, fig. 2.16, is practically impossible to eliminate, leading to poor magnetic and mechanical properties. Exaggerated or discontinuous grain growth is characterized by the excessive growth of some grains at the expense of small, neighboring ones, trapping all the pores present in that volume, fig. 2.17.

Grain growth kinetics depends strongly on the impurity content. A minor dopant can drastically change the nature and concentration of defects in the matrix, affecting grain boundary motion, pore mobility and pore removal [3, 5]. The effect of a given dopant depends on its valence and solubility with respect to host material. If it is not soluble at the sintering temperature, the dopant becomes a second phase, which usually segregates to the grain boundary.

The porosity of ceramic samples results from two sources, intragranular porosity and intergranular porosity, fig. 2.16. An undesirable effect in ceramic samples is the formation of exaggerated or discontinuous grain growth which is characterized by the excessive growth of some grains at the expense of small, neighboring ones, fig. 2.17. When this occurs, the large grain has a high defect concentration. Discontinuous growth is believed to result from one or several of the following: powder mixtures with impurities; a very large distribution of initial particle size; sintering at excessively high temperatures; in ferrites containing *Zn* and /or *Mn*, a low O_2 partial pressure in the sintering atmosphere. When a very large grain is surrounded by smaller ones, it is called ‘duplex’ microstructure.

2.4 Permeability of ferrites

2.4.1 Theories of permeability

Permeability is the degree of magnetization of a material that responds linearly to an applied magnetic field. Magnetic permeability is typically represented by the Greek letter μ.

The reciprocal of magnetic permeability is magnetic reluctivity. In SI units, permeability is measured in Newton per Ampere squared (NA^{-2}). The constant value μ_0 is known as the magnetic constant or the permeability of free space, and has the exact (defined) value $\mu_0 = 4\pi\times10^{-7}\,N\cdot A^{-2}$. In electromagnetism, the applied magnetic field H represents how a magnetic induction B influences the organization of magnetic dipoles in a given medium, including dipole migration and magnetic dipole reorientation [2, 22 and 26]. Magnetic induction, magnetic permeability and magnetic field can be related by

$$B = \mu H \tag{2.18}$$

where the permeability μ is a scalar if the medium is isotropic or a second rank tensor for an anisotropic linear medium.

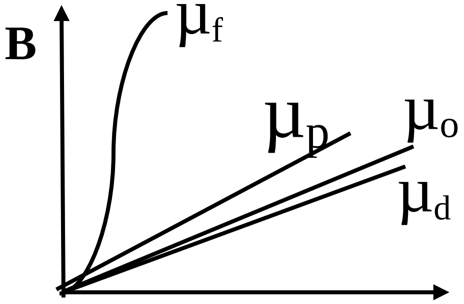

Figure 2.19: Simplified comparison of permeabilities for: ferro or ferri magnets (μ_f), paramagnets (μ_p), free space(μ_0) and diamagnets (μ_d)

In general, permeability is not a constant, as it can vary with the position in the medium, the frequency of the field applied, humidity, temperature, and other parameters. In a nonlinear medium, the permeability can depend on the strength of the magnetic field in Fig. 2.19. Permeability as a function of frequency can take on real or complex values [31,32]. In ferromagnetic materials, the relationship between B and H exhibits both nonlinearity and hysteresis: B is not a single-valued function of H, but depends also on the history of the material. When frequency is considered the permeability can be complex, corresponding to the in phase and out of phase response.

2.4.2 Initial permeability

An important characteristic of magnetization produced by wall bowing is that it is reversible. Walls recover their planar shape when the field is removed; field removal leads to zero magnetization as shown in the Fig. 2.20. In addition to reversibility, the permeability for this particular field range tends to be a linear function of the field; it is known as the initial permeability, μ_i and is defined as:

$$\mu_i = (\frac{\Delta B}{\Delta H})_{H \to 0} \tag{2.19}$$

The initial permeability corresponds to the slope of the B = f(H) relation at the origin and the critical field to the slope change, respectively, Fig 2.20 (usually, it is the relative initial permeability, $\mu_i = (\frac{\Delta B}{\mu_0 \Delta H})$ that is used). The strong increase in magnetization at fields larger than the critical value is therefore a consequence of wall unpinning and displacement.

Wall displacement sweeps volumes significantly larger than wall bowing and leads therefore to a greater slope in the M(H) plot. A plot of permeability as a function of field is often useful to determine characteristics such as initial permeability, μ_i , and maximum permeability, μ_{max}(Fig. 2.20). This plot represents the slope of the B(H) relationship, as a function of H. The initial part at low fields is the initial permeability, μ_i and the maximum corresponds therefore to μ_{max} Fig. 2.20. As H increases above this value, magnetization approaches saturation and permeability decreases as 1/H.

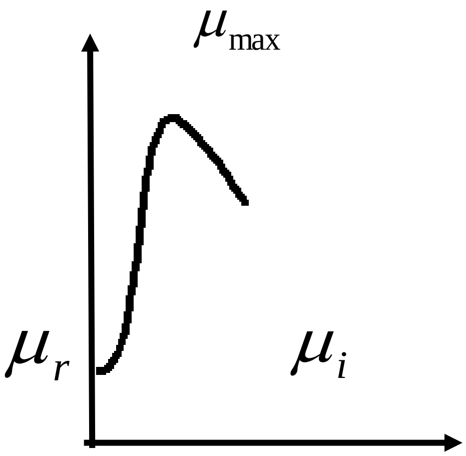

Figure 2.20: Relative permeability as a function of field.

$H(A/m)$

2.4.3 Relative permeability

Relative permeability, sometimes denoted by the symbol μ_r, is the ratio of the permeability of a specific medium to the permeability of free space given by the magnetic constant $\mu_B = 1\pi\times10^{-7}$

$$\mu_r = \frac{\mu}{\mu_0} \tag{2.20}$$

In terms of relative permeability, the magnetic susceptibility is:

$$\chi_m = \mu_r - 1 \tag{2.21}$$

χ_m, a dimensionless quantity, is sometimes called volumetric or bulk susceptibility, to distinguish it from χ_P (magnetic mass or specific susceptibility) and χ_M (molar or molar mass susceptibility).

2.4.4 Complex permeability

A useful tool for dealing with high frequency magnetic effects is the complex permeability. While at low frequencies in a linear material the magnetic field and the auxiliary magnetic field are simply proportional to each other through some scalar permeability, at high frequencies these quantities will react to each other with some lag time.

These fields can be written as

$$H = H_0 e^{-j\omega t} B = B_0 e^{-j(\omega t - \delta)} \tag{2.22}$$

where δ is the phase delay of B from *H*. Understanding permeability as the ratio of the magnetic field to the auxiliary magnetic field, the ratio of the phasors can be written and simplified as

$$\mu = B/H = B_0 e^{-j(\omega t - \delta)} / H_0 e^{-j\omega t} = B/He^{-j\delta} \tag{2.23}$$

so that the permeability becomes a complex number. By Euler's formula, the complex permeability can be translated from polar to rectangular form,

$$\mu = B/H \cos\delta - j\, B/H \sin\delta = \mu^{/} - \mu^{//} \tag{2.24}$$

The real part ($\mu^{/}$) of complex permeability (μ), as expressed in equation (2.8) represents the component of *B* which is in phase with *H*, so it corresponds to the normal permeability. If there are no losses, we should have $\mu = \mu^{/}$. The imaginary part $\mu_{//}$ corresponds to that of *B*, which is delayed by phase angle $90^0$from *H* [5]. The presence of such a component requires a supply of energy to maintain the alternating magnetization, regardless of the origin of delay [33]. The ratio of the imaginary to the real part of the complex permeability is called the loss tangent,

$$\tan\delta = \mu^{//}/\mu^{/} \tag{2.25}$$

which provides a measure of how much power is lost in a material versus how much is stored. The quality factor is defined as the reciprocal of this loss factor, i.e.

$$\text{Quality factor} = 1/\tan\delta \qquad (2.26)$$

And the relative quality factor, $Q = \mu^{/}/\tan\delta$ (2.27)

The curves show the variation of both $\mu^{/}$and $\mu^{//}$with frequency are called the magnetic spectrum or permeability spectrum of the material [5]. The variation of permeability with frequency is referred to as dispersion. The measurement of complex permeability gives us valuable information about the nature of domain wall and their movements. In dynamic measurements the eddy current loss is very important. This occurs due to the irreversible domain wall movements. The permeability of a ferrimagnetic substance is the combined effect of the wall permeability and rotational permeability mechanisms.

2.4.5 Mechanisms of permeability

The mechanisms can be explained as follows: A demagnetized magnetic material is divided into number of Weiss domains separated by Bloch walls [1-3, 34-36]. In each domain all the magnetic moments are oriented in parallel and the magnetization has its saturation value M_s. In the walls the magnetization direction changes gradually from the direction of magnetization in one domain to that in the next. The equilibrium positions of the walls result from the interactions with the magnetization in neighboring domains and from the influence of pores; crystal boundaries and chemical inhomogeneities which tend to favor certain wall positions. There are two mechanisms in the phenomenon of permeability; spin rotation in the magnetic domains and wall displacements [3, 12]. The uncertainty of contribution from each of the mechanisms makes the interpretation of the experimental results difficult. Globus [27, 37] shows that the intrinsic rotational permeability μ_r and 180_0 wall permeability μ_w may be written as: $\mu_r = 1 + 2\pi M_s^2/K$ and $\mu_w = 1 + 3\pi M_s^2 D/4\gamma$, where M_s is the saturation magnetization, K is the total anisotropy, D is the grain diameter and $\gamma \equiv K\delta_w$ is the wall energy [33, 38, 39].

2.5 Magnetic domain and magnetization process

2.5.1 Magnetic domain

Domain is a region within a magnetic material which has uniform magnetization. In a ferromagnetic domain, there is parallel alignment of the atomic moments. In a ferrite domain, the net moments of the antiferromagnetic interactions are spontaneously oriented parallel to each other (even without an applied magnetic field). The term, spontaneous magnetization or polarization is often used to describe this property. Each domain becomes a magnet composed of smaller magnets (ferromagnetic moments). Domains are formed basically to reduce the magnetostatic energy which is the magnetic potential energy contained in the field lines (or flux lines as they are commonly called) connecting north and south poles outside of the material. Fig. 2.21 (a) shows a single domain. The arrows indicate the direction of the magnetization and consequently the direction of spin alignment in the domain [2]. We can substantially reduce the length of the flux path. The Fig. 2.21 shows domain divided into two or more smaller domains. This splitting process continues to lower the energy of the system until the point that more energy is required to form the domain boundary than is decreased by the magnetostatic energy change.

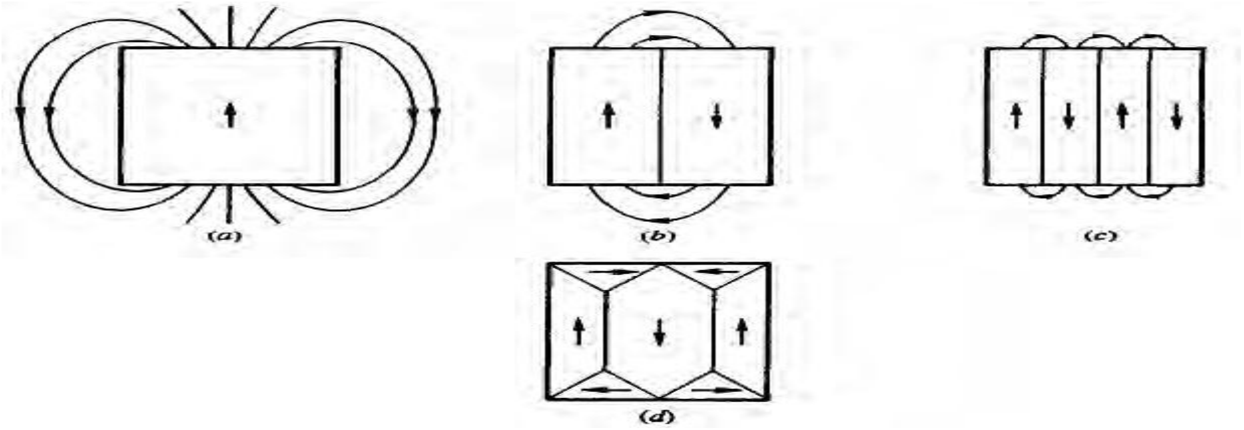

Figure 2.21: (a)—(c) Reduction in magnetostatic energy, *Em*, by subdivision into magnetic domains, (d) virtual elimination of *Em*by creation of closure domains (adapted from ref. [3]).

The size and shape of a domain may be determined by the minimization of several types of energies. They are [3]:

1. Magnetostatic Energy
2. Magnetocrystalline Anisotropy Energy
3. Magnetostrictive Energy
4. Domain Wall Energy

A domain wall is an interface separating magnetic domains. It is a transition between different magnetic moments and usually undergoes an angular displacement of 90° or 180°.

Domain wall is a gradual reorientation of individual moments across a finite distance. The domain wall thickness depends on the anisotropy of the material, but on average spans across around 100-150 atoms. The energy of a domain wall is simply the difference between the magnetic moments before and after the domain wall was created. This value is usually expressed as energy per unit wall area. The width of the domain wall varies due to the two opposing energies that create it: the magnetocrystalline anisotropy energy and the exchange energy (J_{ex}), both of which tend to be as low as possible so as to be in a more favorable energetic state. The anisotropy energy is lowest when the individual magnetic moments are aligned with the crystal lattice axes thus reducing the width of the domain wall. Whereas the exchange energy is reduced when the magnetic moments are aligned parallel to each other and thus makes the wall thicker, due to the repulsion between them (Where anti-parallel alignment would bring them closer working to reduce the wall thickness). In the end equilibrium is reached between the two and the domain wall's width is set as such.

2.5.2 Magnetization process

The response of any magnetic material to an applied magnetic field can be understood on the basis of magnetic domains and domain walls [2]. Magnetization processes are essentially similar in ferromagnetic metals and ferrimagnetic ceramics. The division of a magnetic material into domains explains why, when no field is applied, the magnetic flux is entirely contained within the sample and there is no external manifestation of it. The application of an external field, however, can result in a dramatic increase of magnetization in the sample; an extreme ease appears for a Ni—Fe alloy. A small field of 2 A/m can lead to a magnetization of 400 kA/m, quite close to its saturation value, M~ 477kA/m, which represents a susceptibility, M/H, of 200000. In ferro- and ferrimagnetic materials, it is more common to use the permeability, μ instead of the susceptibility, because the induction, B, is measured directly. Induction, magnetization and field are related by [2- 4]:

$$B_0 = (\mu_0 H + M) \qquad (2.28)$$

If the permeability and susceptibility are defined by $\mu = \frac{B}{H}$ and $\chi = \frac{M}{H}$,then they are related by

$\mu = \mu_0(1+\chi)$ or $\mu_r = 1+\chi$, where $\mu_r(=\frac{\mu}{\mu_0})$ is a relative permeability.

The value of the relative permeability gives a good indication of how easily a given material can be magnetized, since =1 μ_r represents the free space. An additional advantage of using μ_r is that it has exactly the same value in both CGS and SI unit systems. But the important fact in the magnetization curve of Fig. 2.22 is that a small field can lead to an enormous magnetization change.

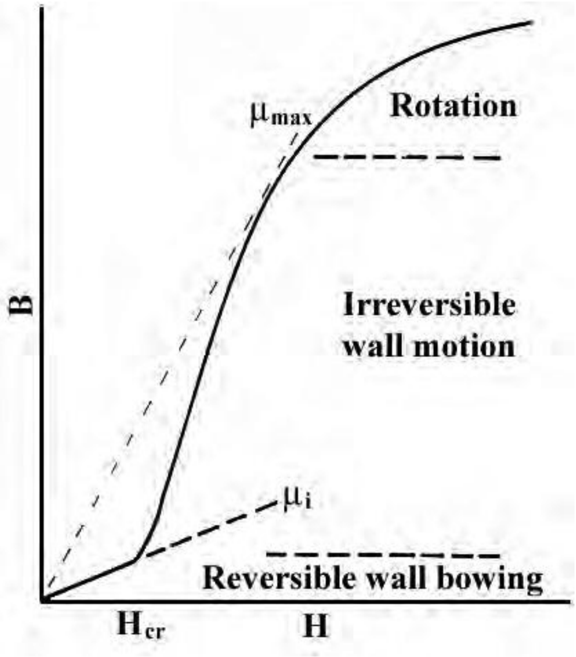

Figure 2.22: Schematic magnetization curve showing the important parameter: initial permeability, μ_i (the slope of the curve at low fields) and the main magnetization mechanism in each magnetization range (adapted from ref. [3]).

Large permeability or substantially large magnetization produced by small fields can only occur because of domain walls [2- 4]. Suppose that a small field, H, with +z orientation is applied to (the magnetic material of Fig. 2.23, which has two domains separated by a Bloch wall (one domain with spins oriented along +z, parallel to the field and the other domain along - z, opposite to H).

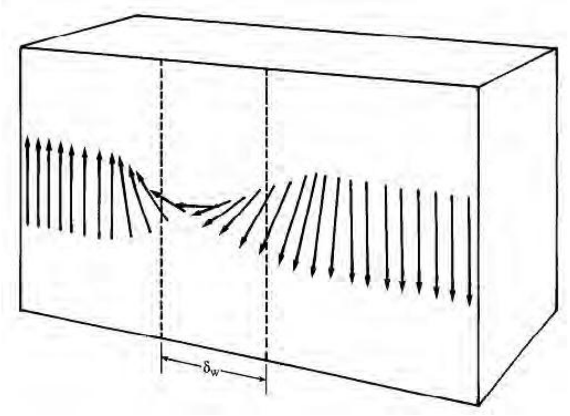

Figure 2.23: Model of a Bloch domain wall thickness (adapted from ref. [23]).

Since H is small, it has a negligible effect on the spins; these spins are coupled to the - *z* easy direction by the magnetocrystalline anisotropy. However, the effect of the field on wall spins can be important; these spins are in a sensitive equilibrium state between two easy directions (both + *z* and -z: are easy directions) and can easily be reoriented by the field. The result is that the wall moves from left to right, increasing the volume of the +z domain at the expense of the -z domain. There is no actual displacement of the wall, but a progressive reversal of spins, as in a wave. However, as in many other collective phenomena, it is easy to visualize it in terms of wall movement. Magnetization variations are large because even a small wall displacement involves the reversal of spins within a substantial domain volume. Also, the volume change results in two fold magnetization variation since the increase in volume with the field orientation occurs at the expense of domains with the opposite orientation. The increase in magnetic field leads to domain wall displacements until all the domains with orientations opposite to the field have been substituted by domain with direction parallel to H. However, there might be domains with orientation neither opposite nor parallel; also, the applied field can have an orientation which does not coincide with an easy direction. In the general case, to attain the saturation state (in which the sample becomes a single domain oriented along the field direction), a rotation mechanism is required, as indicated in Fig. 2.23. This magnetization mechanism takes place at high fields; it involves higher energies because the field has to overcome the anisotropy field to produce spin reversal. In contrast, domain wall motion occurs by the progressive reversal of a small fraction of spins, from an easy direction to another one.

Magnetization processes can be affected by stress [2-4]. These phenomena, known as stress anisotropy, are related to magnetostriction and can also be explained on the basis of the spin-orbit coupling. The domain wall displacement is not started by any field. There exists a threshold or critical field (H_{cr}), below which the wall is not displaced. This critical field depends on sample defects; walls are affected by any deviation from the lattice periodicity: point defects, dislocations, other phases, porosity and even the sample’s external surface act as pinning sites. The effect of defects can be understood by considering that any discontinuity in magnetic flux represents an additional contribution to the magnetostatic energy. So the defects lead to a higher critical field. Another important consequence of defects is that even if a wall is displaced, it is pinned in a new position when the field is removed. To obtain a new wall displacement, a larger field than the initial one is usually required.

The critical field appears as a change of slop in the magnetization curve (fig. 2.22).

For fields lower than the critical value, there is a net magnetization. This means that even a pinned wall can give a response to an applied field. The mechanism responsible for this magnetization is domain wall bowing or bulging & a pinned wall can be bent as a flexible membrane under the field ‘pressure’ in the energy balance, the increase in total wall energy (due to the increase in wall surface area) is overcome by the decrease in potential energy (as a result of the increase in magnetic moments in the field direction).

2.5.3 Hysteresis loop

In polycrystalline materials, the hysteresis loop can be described by a combination of bowing, unpinning and displacement processes on grain boundaries [2-6, 27]. Starting from the demagnetized state, Fig. 2.22, the sample is represented by a single grain divided into two domains, separated by a diametral Bloch wall. Application of a small field leads to reversible wall bowing, corresponding to initial permeability. For $H>H_{cr}$, the wall is unpinned and displaced within the grain, resulting in a strong increase in magnetization. Removal of the strong field (larger than the critical value) does not lead to elimination of magnetization, but in a remanent state, Br, which is shown in the Fig. 2.24. The wall is now pinned in a new position within the grain; the small reduction in magnetization towards the remanent state is due to the fact that the wall recovers its planar shape. A new wall displacement requires a new critical field.

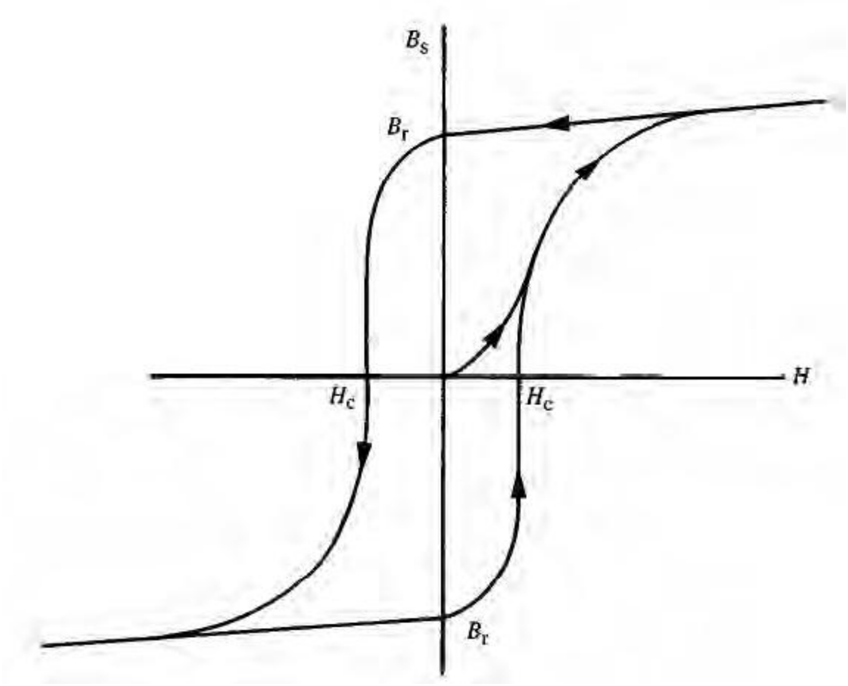

Figure 2.24:B-H loop. Bs, Br, Hc are the saturation induction, remanent induction and coercive field, respectively (adapted from ref. [2]).

A field with the opposite orientation is now applied. Wall bowing occurs for small fields; the critical field value for this new position is generally larger than for the initial displacement from the zero magnetization state. This field is known as coercive field, coercive force or coercivity, Hc. When the value of this field is overcome, a reversal of magnetization is produced (the wall is unpinned and displaced towards the other end of the grain) and a tendency to saturation in the new orientation areas (wall is pinned again).

Removal of the field leads to the symmetric remanent magnetization. A cyclic field results therefore in a loop; this is the hysteresis loop, which is in some way a synthesis of almost all magnetic phenomena.

2.6 Dielectrics

Dielectrics are insulators, plain and simple. The two words refer to the same class of materials, but are of different origin and are used preferentially in different contexts. Inserting a layer of nonmetallic solid between the plates of a capacitor increases its capacitance. The Greek prefix *di* or *dia* means "across". A line across the angles of a rectangle is a diagonal. The material placed across the plates of a capacitor like a little nonconducting bridge is a *dielectric*.

When a metal is placed in an electric field the free electrons flow against the field until they run out of conducting material. In no time at all, we'll have an excess electron on one side and a deficit on the other. One side of the conductor has become negatively charged and the other positively charged. Release the field and the electrons on the negatively charged side now find themselves too close for comfort. Like charges repel and the electrons run away from each other as fast as they can until they're distributed uniformly throughout; one electron for every proton on average in the space surrounding every atom. Conducting electrons are free to roam around as much as they want.

When the atoms or molecules of a dielectric are placed in an external electric field, the nuclei are pushed with the field resulting in an increased positive charge on one side while the electron clouds are pulled against it resulting in an increased negative charge on the other side. This process is known as polarization and a dielectric material in such a state is said to be polarized. There are two principal methods by which a dielectric can be polarized: stretching and rotation.

Stretching an atom or molecule results in an induced dipole moment added to every atom or molecule.

Rotation occurs only in polar molecules — those with a permanent dipole moment.

Polar molecules generally polarize more strongly than nonpolar molecules.

This happens for two reasons — one of which is usually trivial. First, all molecules stretch in an electric field whether they rotate or not. Nonpolar molecules and atoms stretch, while polar molecules stretch *and* rotate.

2.6.1 Dielectric properties

Studies of dielectric properties provide a great deal of information about the acceptance of the material for vaious applications. Dielectric constant (ε')is an important parameter for dielectric materials.

Dielectric constant

Dielectric constant**,** property of an electrical insulating material (a dielectric) equal to the ratio of the capacitance of a capacitor filled with the given material to thecapacitance of an identical capacitor in a vacuum without the dielectric material. The insertion of a dielectric between the plates of, say, a parallel-plate capacitor always increases its capacitance, or ability to store opposite charges on each plate, compared with this ability when the plates are separated by a vacuum. If C is the value of the capacitance of a capacitor filled with a given dielectric and C_0 is the capacitance of an identical capacitor in a vacuum, the dielectric constant, symbolized by the Greek letter kappa, κ, is simply expressed as $\kappa = C/C_0$. E is always less than or equal to E_o,so the dielectric constant is greater than or equal to 1. The larger the dielectric constant, the more charge can be stored.

Completely filling the space between capacitor plates with a dielectric increases the capacitance by a factor of the dielectric constant:

$C = k\, C_o$, where C_o is the capacitance with no dielectric between the plates.

For a parallel-plate capacitor containing a dielectric that completely fills the space between the plates, the capacitance is given by:

$$C = \frac{k\varepsilon_0 A}{d} \qquad (2.29)$$

This is the only variable left with the material scientist to increase the capacitance per unit volume value of capacitor for modern electronics application.

Dependence of dielectric constant on frequency

Electrons have very much smaller mass than that of ions, so they respond more rapidly to a changing electric field. For electric field that oscillates at extremely high frequencies (like light) only electronic polarization can takes place. At lesser frequencies, the relative displacement of positive and negative ions can take place. Orientation of permanent dipoles, which require the rotation of a molecule can occur only if the oscillation is relatively show (MHz range or slower). The total polarization P, total polarizability and the relative permittivity of a dielectric in an alternating field all depend on the ease with which the dipoles can reverse alignment with each other reversal of the field. Some polarizability mechanisms do not permit sufficiently rapid reversal of the dipole alignment. In such a process the time required to reach the equilibrium orientation is called the relaxation time and its reciprocal the relaxation frequency. It can be also defined as the time specific polarization to occur is called the relaxation time. When the frequency of the applied field exceeds that of the relaxation frequency of a particular polarization process, the dipoles cannot reorient fast enough and operation of the process ceases.

2.7 X-Ray Diffraction

The XRD data consisting of θ_{hkl} and d_{hkl} values corresponding to the different crystallographic planes are used to determine the structural information of the samples like lattice parameter and constituent phase. Normally, lattice parameter of a composition is determined by the Debye-Scherrer method after extrapolation of the curve. We would like to understand how the value of lattice parameter changes with the increase of yttrium content in the Mn-Ni-Zn ferrites. We determine the lattice spacing (inter planer distance), d using the following equation [23] which is related to the measurement of lattice parameter, X-ray density and porosity.

$$2d_{hkl}\sin\theta = \lambda$$

i.e. $d_{hkl} = \frac{\lambda}{2\sin\theta}$, (2.30)

(i) Lattice parameter

The lattice parameters from XRD of the samples are calculated by using the following relations;

$$\frac{1}{d_{hkl}^2} = \frac{h^2+k^2+l^2}{a^2} \text{(For cubic)} \quad (2.31)$$

$$\frac{1}{d_{hkl}^2} = \frac{4(h^2+hk+k^2)}{3a^2} + \frac{l^2}{c^2} \text{ (For rhombohedral)} \quad (2.32)$$

$$\frac{1}{d_{hkl}^2} = \frac{h^2}{a^2} + \frac{k^2}{b^2} + \frac{l^2}{c^2} \text{ (For orthorhombic)} \quad (2.33)$$

$$\frac{1}{d_{hkl}^2} = \frac{h^2+k^2}{a^2} + \frac{l^2}{c^2} \text{(For tetragonal)} \quad (2.34)$$

Here, *h*, *k*, *l* are miller indices of the crystal plane.

In this work, we have considered 8 prominent reflection planes for a cubic crystal,

$a = d_{hkl}\sqrt{h^2+k^2+l^2}$ (2.35)

Where, a is the lattice parameter and hkl are the Miller indices.

To get the exact value of lattice parameters we have used Nelson-Riley method [40]. The Nelson-Riley function can be written as,

$$F(\theta) = \frac{1}{2}\left(\frac{cos^2\theta}{sin\theta} + \frac{cos^2\theta}{\theta}\right) \qquad (2.36)$$

We have drawn 'a' vs $F(\theta)$ graph. From this graph we have determined the value of 'a' at $F(\theta) = 0$ by using the linear least fitting method. This is the exact value of 'a'.

(ii) X-ray Density, Bulk Density and porosity

Using the value of 'a' we have calculated the X-ray density of Mn-Ni-Zn ferrites. The X-ray density is defined as

$$\rho_x = \frac{8M}{Na^3} gm/cm^3 \qquad (2.37)$$

Where, N is the Avogadro's number and M is the molecular mass.

The bulk density of the samples were also calculated by using the formula

$$\rho_B = \frac{M}{V} \qquad (2.38)$$

And finally we have measured the porosity of the samples using the formula given below[41],

$$P = \left(1 - \frac{\rho_B}{\rho_x}\right) \times 100\% \qquad (2.39)$$

2.8 Resistance and Resistivity

The electrical resistance of an electrical conductor is a measure of the difficulty to pass an electric current through that conductor. Electrical resistance shares some conceptual parallels with the notion of mechanical friction.

An object of uniform cross section has a resistance proportional to its resistivity and length and inversely proportional to its cross-sectional area. All materials show some resistance, except for superconductors, which have a resistance of zero.

The resistance of a given object depends primarily on two factors: what material it is made of, and its shape. For a given material, the resistance is proportional to the length; for example, a long copper wire has higher resistance than an otherwise-identical short copper wire. The resistance can be computed as

$$R = \rho \frac{l}{A} \tag{2.40}$$

Where l is the length of the object, A is the cross-sectional area of the object and ρ is the electrical resistivity of the material.

2.8.1 Temperature dependence of Resistivity

Resistivity varies with temperature. Near room temperature, the resistivity of metals typically increases as temperature is increased, while the resistivity of semiconductors typically decreases as temperature is increased. The resistivity of insulators and electrolytes may increase or decrease depending on the system.

If the temperature does not vary too much, a linear approximation is typically used:

$$R(T) = R_0[1 + \alpha(T - T_0)] \tag{2.41}$$

Where α is called as the temperature coefficient of resistance, T_0 is a fixed temperature (usually room temperature), and R_0 is the resistance at room temperature T_0.

References:

[1] K. H. J. Buschow, and F. R. De Boer, Physics of Magnetism and Magnetic Materials, Kluwer Academic Publishers, New York, USA (2004).

[2] A. Goldman, Modern ferrites Technology, 2nd Edition, Pittsburgh, PA, USA (1999).

[3] R. Valenzuela, Magnetic Ceramics, Cambridge University Press, Cambridge (1994).

[4] N. A. Spaldin, Magnetic Materials, Fundamentals and device applications, Cambridge University Press (2003).

[5] B. D. Cullity, Introduction to Magnetic Materials, Addison-Wesley Publishing Company, Inc., California (1972).

[6] L. Něel, Annales de Physique, 3 (1948) 137.

[7] S. Hilpert, Ber. Deutseh. Chem. Ges. Bd 2, 42 (1909) 2248.

[8] J. L. Snoek, New developments in ferromagnetism, Elsevier, (1949) 139.

[9] T. Takai, J. Electrochem. Ass. Japan., 5 (1937) 411.

[10] E. W. Gorter, Some properties of ferrites in connection with their Chemistry, Proc. I. R. E., 43 (1955) 1945.

[11] E. Roess, Ferrites, U. of Tokyo Press, Tokyo, 187 (1971).

[12] T. Nakamura, J. Mag.Mag. Mater., 168 (1997) 285.

[13] J. Tasaki, and T. Ito, Intl. Conf. on Ferrite, Japan, (1970).

[14] M. A. Wahab, Solid State Physics: Structure and Properties of Materials, Narosa Publishing House, New Delhi, (1999).

[15] J. Smit, H. Wijn, Ferrites, Wiley, the Netherlands (1959).

[16] F. Brailsford, Physical Principles of Magnetism, D. Van Nostrand Company Ltd., London (1966).

[17] A. J. Dekker, Solid State Physics, Macmillan India Ltd., New Delhi, (1998).

[18] P. G. Bercoff, and H. R. Bertorello, J. Magn.Magn. Mater., 213 (2000) 56.

[19] G. F. Dionne, J. Al. Phys., 41 (1970) 4874.

[20] S. Geller, J. Al. Phys., 37 (1966) 1408.

[21] C.E. Patton, Y. Liu, J. Phys. C: Solid State Phys., 16 (1983) 5995.

[22] Y. Yafet, and C. Kittel, Antiferromagnetic arrangement in ferrites, J. Phys. Rev., 87 (1952) 290.

[23] C. Kittel, Introduction to Solid State Physics, 7th edition, Jhon Wiley and Sons, Inc., Singapore (1996).

[24] P. W. Anderson, Phys. Rev., 79 (1950) 350.

[25] C. Guilland, J. Phys. Rad., 12 (1951) 239.

[26] D. Hadfield, Permanent Magnets and Magnetism, Jhon Wiley and Sons, Inc., New York, (1962).

[27] A. Globus, 2nd EFS Conf. on Soft Magnetic Materials, Wolfson Center for Magnetic Technology, Cardiff, Wales, (1975).

[28] M. F. Yan, and D. W. Johnson, J. Am. Ceram. Soc., 61(342) (1978).

[29] A. K. Singh, T. C. Goel, and R. G. Mendiratta, J. Al. Phys., 92 (2002) 3872.

[30] R C. Kambale, P A. Shaikh, C. H. Bhosale, K. Y. Rajpure, and Y. D. Kolekar, Smart Mater. Struct., 18 (2009).

[31] Z. Krysicki, T. Luban'ska, J. Magn. Magn. Mater., 19 (1980) 107.

[32] T. Pannaparayil, R. Marande, and S. Komarneni, J. Al. Phys., 69 (1991) 5349.

[33] P. J. Vander Zaag, M. Kolenbrander, and M. T. Rekveldt, J. Al. Phys., 83 (1998) 6870.

[34] S. T. Alone, and K. M. Jadhav, Pramana–J. Phys., 70 (2008) 173.

[35] A. M. Abo El Ataa, M. K. El Nimra, , S. M. Attiab, , D. El Konya, , and. A. H. Al-Hammadic, J. Mang. Mang. Mater., 297 (2006) 33.

[36] W. Bayoumi, J. Mater. Sci., 42 (2007) 8254.

[37] T. Nakamura, J. Al. Phys., 88 (2000) 348.

[38] T. Nakamura, and Y. Okano, J. Al. Phys., 79 (1996) 7129.

[39] V. K. Babbar, and R. K. Puri, IEEE transactions on magnetics, 28 (1992) 21.

[40] A. Khan, M.A. Bhuiyan, G.D. Al-Quaderi, K.H. Maria, S. Choudhury, K.A. Hossain, S. Akther and D.K. Saha, J. Bang. Aca. Sci, 37 (2013) 73.

[41] I. I. McColm, N. J. Clark, "Forming, Shaping and Working of High Performance Ceramics", Glasgow: Blackic (1988).

CHAPTER 3

SAMPLE PREPARATION

CHAPTER 3

SAMPLE PREPARATION

There are various methods to the successful preparation of ferrite samples of high quality. The well-known fabrication process of ferrites comprises to the conventional ceramic method. Recently, many processing techniques have been proposed by different research groups to enrich the structural, magnetic and electrical properties few versatile applications [1,2]. These techniques are mainly grouped into two classes:

i. Conventional ceramic method

The widely known name is solid state reaction technique. This method involves milling such as hand or ball milling of the reactants with followed by heating at elevated temperature range.

i. Non-conventional method

Fabrication of the ceramic powders by wet method is-

Some popular non-conventional methods are:

1. Sol-gel synthesis [3]
2. Co-precipitation method [4]
3. Organic precursor method [5]
4. Hydrothermal precipitation calcinations technique [6]
5. Microwave sintering technique [7]
6. Auto Combustion method [8]
7. Glass crystalization method [9]
8. Sputtering technique [10]
9. Salt-melt technique [11]

Here, the solid state reaction technique will be used in this research work whathas been discussed.

3.1 Solid state reaction method

Solid state reaction is a chemical reactionsystem in the absence of a solvent. In the typical solid state reaction process,the reactants are first mixed in a mortar and pressed in a pellets at highpressure. Then the pellets are sintered in furnace. After that the products arecrushed, ground, pressed into pellets, and sintered again several times. The most common type of mill is the ball mill, which consists of a lined pot with hard spheres or rod inside. In this case the grinding media is the ball of stainless steel with different sizes in diameter. Another milling process is carried out by mortar or pestle. In order to increase the degree of mixing, these milling can be performed in a wet medium. This method depends on the solid state inter-diffusion between the raw materials. Solids do not usually react at room temperatures for the diffusion length $(2Dt)^{1/2}$ to exceed the particle size, where D is the diffusion constant for the fast-diffusing species, and t is firing time. The ground powders are then calcined in air or oxygen at the required temperature. For some time, this process is continued until the mixture is converted into the correct crystalline phase. The calcined powders are calcined powders using die-punch assembly or hydrostatic or isostatic pressure. Then sintering is carried put at different temperatures for times of typically 2-5 h in various atmospheres [12-14]. The solid state preparation process generally comprised of the following four major steps:

i. Milling of raw materials for homogeneous mixing and particle size reduction
ii. Pre-sintering of the mixture to form ferrite
iii. Milling and pressing the powder in to the required shapes
iv. Sintering to produce a highly densified product

3.2 Composition of the studied Ferrites

Polycrystalline samples $Co_{1-x}Zn_xFe_2O_4$ (x=0.0,0.5) are synthesized by standardsolid state reaction technique. The samples of various compositions have been fabricated by conventional ceramic method keeping in view of their ionic radii and valences for maintaining the charge neutrality. The high purity oxides of CoO, ZnO and Fe_2O_3powders has been mixed and ground in an agate mortar till a homogeneous mixture is formed. This mixture is calcined at 750 °C for 3 hours in a programmable furnace. The powders are pressed into pellets using a uniaxial hydraulic press and sintered at 1050 °C for 2 hours. The sintered powders and pellets are used to measure the required structural, morphological, dielectric and magnetic properties. The overall preparation process and sintering facility available at the Materials Science Division, Atomic Energy Center, Dhaka, has been utilized for the preparation of samples. The weight percentage of the oxide to be mixed for various samples was calcined by using formula:

$$\text{Weight \% of oxide} = \frac{\text{M. wt. of oxide X required weight of the sample}}{\text{Sum of Mol. Wt. of each oxide in a sample}}$$

Content X	Weight % of CoO(gm)	Weight % of ZnO(gm)	Weight % of Fe_2O_3(gm)	Total weight (g)
0.00	3.7848	0.0	8.1675	11.9522
0.1	3.4397	0.4152	8.1450	11.9999
0.2	3.0491	0.8281	8.1226	11.9998
0.3	2.6607	1.2388	8.1004	11.9999
0.4	2.2743	1.6473	8.0782	11.9998
0.5	1.8901	2.0535	8.0562	11.9998

Table 3.1: Compositional details of $Co_{1-x}Zn_xFe_2O_4$ (x=0.0,0.5) ferrites for 12 grams sample

3.3 Milling of Raw Materials

In this step, the extension of sample mixing process greatly depends on the starting materials. The component oxides of the materials are mixed by both hand milling and ball milling. The raw materials for the preparation of Cobalt Ferrites and Zinc doped Cobalt Ferrites are high purity powders of CoO, Fe_2O_3 and ZnO. The constituent in required stoichiometric proportions was weighted first and the weighted powders were mixed thoroughly using ceramic mortar and pestle for 1 hour. The obtained powders were then ball milled for 6 hours in distilled water media with stainless steel balls of different sizes in diameter to produce fine powders. After ball milling, the wet sample was dried and again hand milled for 1 hour to reduce particle size. The overall milling process was done with intensive care to get homogeneous mixture and to avoid unwanted contamination.

Figure 3.1: Hand milling and ball milling of rare earth ferrite synthesis in the Materials Science Division laboratory of Atomic Energy Centre, Dhaka (captured with permission).

3.4 Calcination

Calcination is the process in which a material is heated to a temperature below its melting point to effect the thermal decomposition or the phase transition other than melting point, or removal of a volatile fraction. The process of calcination derives its name from the Latin calcinare (to burn lime) [15] due to its most common application The product of calcination is usually referred to in general as "calcine," regardless of the actual minerals undergoing thermal treatment. Calcination is different from roasting, in which more complex gas-solid reactions take place between the furnace atmosphere and the solids.

Synthesis of the phase of a compound takes place by solid phase reaction, which involves the chemical reaction through atomic diffusion among grains at temperature below the melting points of the raw materials [16]. Calcination reactions usually take place at or above the thermal decomposition temperature or the transition temperature (for phase transitions). In the materials which have volatile constituents, to avoid loss of the volatile parts, the calcination temperature must be kept low enough.

The prepared samples of $Co_{1-x}Zn_xFe_2O_4$ (x=0.0,0.5) was palletized and then placed to the porcelain crucible for pre -sintering at temperature 750℃ for 3 hours. This was performed in a furnace named Gallen Camp at Materials Science Division, Atomic Energy Center, Dhaka (AECD). Pre-sintering is important to occur Solid State Reaction between the component oxides and to impurities from the sample that is achieved by counter diffusion.

During the calcination process, the reaction of Fe_2O_3 with metal oxide (say, MO or M_2O_3) takes place in the solid state to form spinal phase according to the following reactions:

$$MO + Fe_2O_3 \rightarrow MFe_2O_4$$

$$2M_2O_3+4Fe_2O_3 \rightarrow 4MFe_2O_4 + O_2$$

The reaction involved to the proposed sample are,

$$CoO+Fe_2O_3 \longrightarrow CoFe_2O_4$$

$$CoO+Fe_2O_3+ZnO \longrightarrow Co_{1-x}Zn_xFe_2O_4$$

In order to produce chemically homogeneous, dense and effectively better material of required shape and size, sintering temperature is needed.

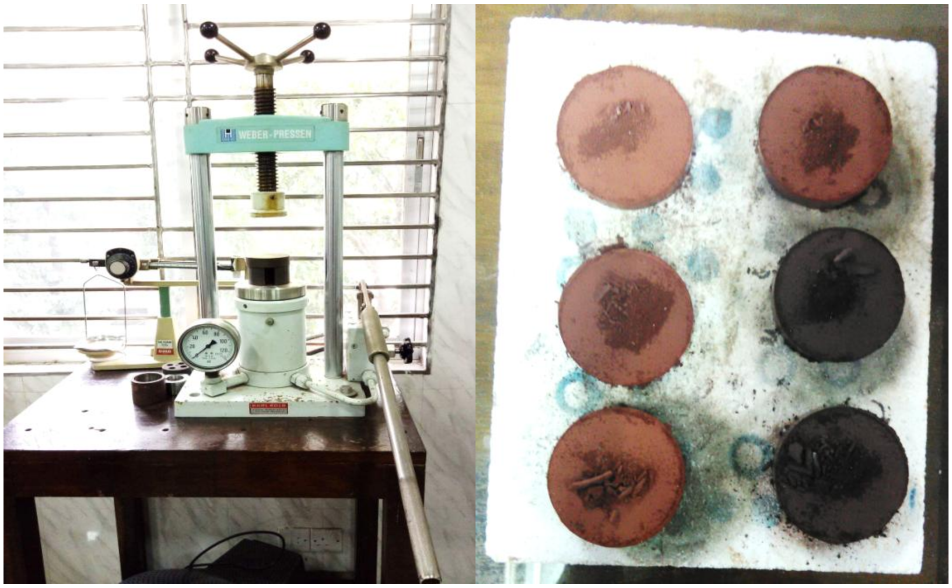

Figure 3.2: The preparation of palletized shape sample by hydraulic method in the Materials Science Division laboratory of Atomic Energy Centre, Dhaka (captured with permission).

3.5 Preparing pellets

Calcined powders are ball mixed again to give a suitable shaping to the powder. After pre-sintering, all the samples are hand milled for 1 hour using ceramic mortar and pestle. Grinding reduces the particle size to ≈ 1 micron and also eliminates intra-particle porosity. Now to the mixed homogeneous powder a small amount of saturated solution of polyvinyl alcohol is added as a binder. Then uniaxial pressing is used to make compacts of small sizes with simple shapes of the calcined powder. It is carried out in a die having movable top. A cavity is formed at the bottom in lower portion. This cavity is filled with free flowing granulated powder and it is stuck with the top to die. With the help of the top-punch, pressure in the range of 20-5- MPa is applied using a hydraulic press.

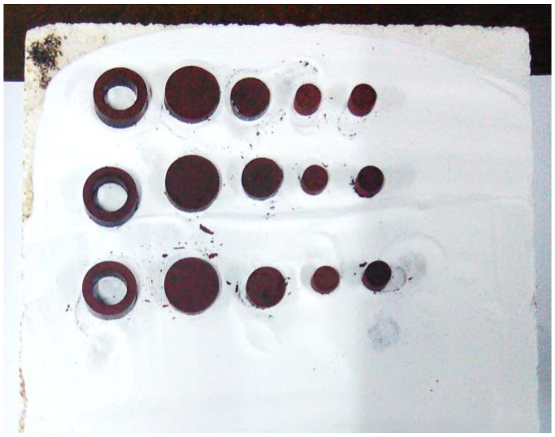

Figure 3.3: Preparation of different shapes of samples under hand milling process after sintering in the Materials Science Division laboratory of Atomic Energy Centre, Dhaka (captured with permission).

Table 3.2: Shape, weight, diameter, pressure and purpose of prepared sample.

Shape	Weight (gm)	Pressure (kN)	Purpose
Ring	2.4	15	Permeability
Tablet	2.4	20	XRD
Tablet	2.4	20	VSM
Tablet	2.4	20	SEM, Resistivity, Dielectric constant

3.6 Sintering

Process of forming objects from a metal powder by heating the powder at a temperature below its melting point [17,18]. In the production of small metal objects, it is often not practical to cast them. Through chemical or mechanical procedures, a fine powder of the metal can be produced. When the powder is compacted into the desired shape and heated, i.e., sintered, for up to three hours, the particles composing the powder join together to form a single solid object.

When thermal energy is applied to powder compact, the compact is densified, and the average grain size is increased. Basic phenomena occurring from this process is densification and grain growth. This is the process used to produced density control materials or compound from metal or ceramic powder by applying thermal energy. During sintering at an appreciable temperature, the atomic motion is more violent and the area between grains in contact inverses due to the thermal expansion of the grains and finally only one interface between two grains remains. This corresponds to a state with much lower surface energy. In this state, the atoms on the grain surfaces are affected by neighboring atoms in all directions which results in densified ceramic [19].

Sintering aims to produce sintered part with reproducible and if possible, designed a microstructure through control the sintering variables.

Microstructural control means control of gain size, sintered density, and size and distribution of other phases including pores. In most of the cases microstructural control prepare a full dense body with fine grain structure.

The main objectives of the sintering are:

(i) Formation of the chemical bonds among particles so as to impart sufficient strength to the product.

(ii) Increasing the grain density by eliminating the pores and

(iii) Completion of the reactions that remains unfinished in the calcination step.

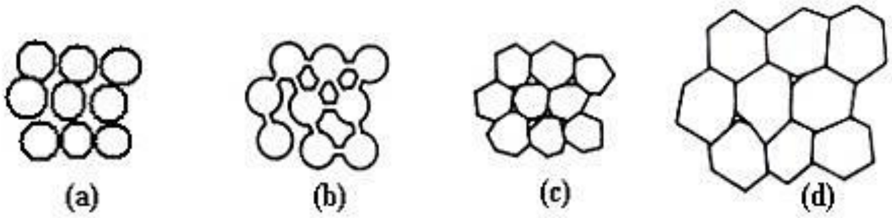

Figure 3.4: Schematic representation of sintering stages: (a) green body, (b) initial stage, (c) intermediate stage, and (d) final stage.

Sintering is divided into three stages, Fig. 3.5 [20, 21].

Stage 1. Contact area between particles increases,

Stage 2. Porosity changes from open to closed porosity,

Stage 3. Pore volume decreases; grains grow.

Advantages of Sintering

The advantages of sintering method are listed in below:

- Stabilization of high levels of purity in the materials.
- Increase of inter-particle contact area with time.

- In most cases, the approach of particle centers resulting overall densification.

- Decrease in volume of inter connected pores.

- Making homogeneous distribution of grain number, grain size and shape.

- Forming a stable chemical composition and crystal structure.

3.7 Synthesis of Composition

The Zn doped $CoFe_2O_4$ ceramic were prepared by solid state reaction method by taking four raw materials such as (i) Cobalt oxide (CoO), (ii) Iron oxide (Fe_2O_3) and (iii) Zinc Oxide (ZnO). For the combination of these three raw materials $Co_{1-x}Zn_xFe_2O_4$ (x=0.0,0.5) ceramic compound were formed, where "x" is the Zn concentration in $CoFe_2O_4$ ceramic compound. For synthesis of $CoFe_2O_4$ ceramic compound-

1. We grinded the milled powder into extremely fine powder for 4 hours.

2. The prepared powder were kept in programmable furnace for calcinations process and heated at temperature below melting point of the sample for the phase formation and removal of a volatile fraction. Here the calcination temperature is 750˚C and it was calcined for 3 hours.

3. Then we make pellets by using hydraulic pressure.

4. We sintered the samples for 2 hours at 1050˚C to get the structural, dielectric and magnetic properties of the ceramics.

5. To know the phase formation of prepared sample used XRD analysis technique. We have used SEM for surface morphology of $CoFe_2O_4$ and Zn doped $CoFe_2O_4$ ceramic compound. We also measured the electrical properties i.e, dielectric properties and at last magnetic properties of the samples.

The flow chart for the preparation of samples by solid-state reaction technique is shown in the following flow chart.

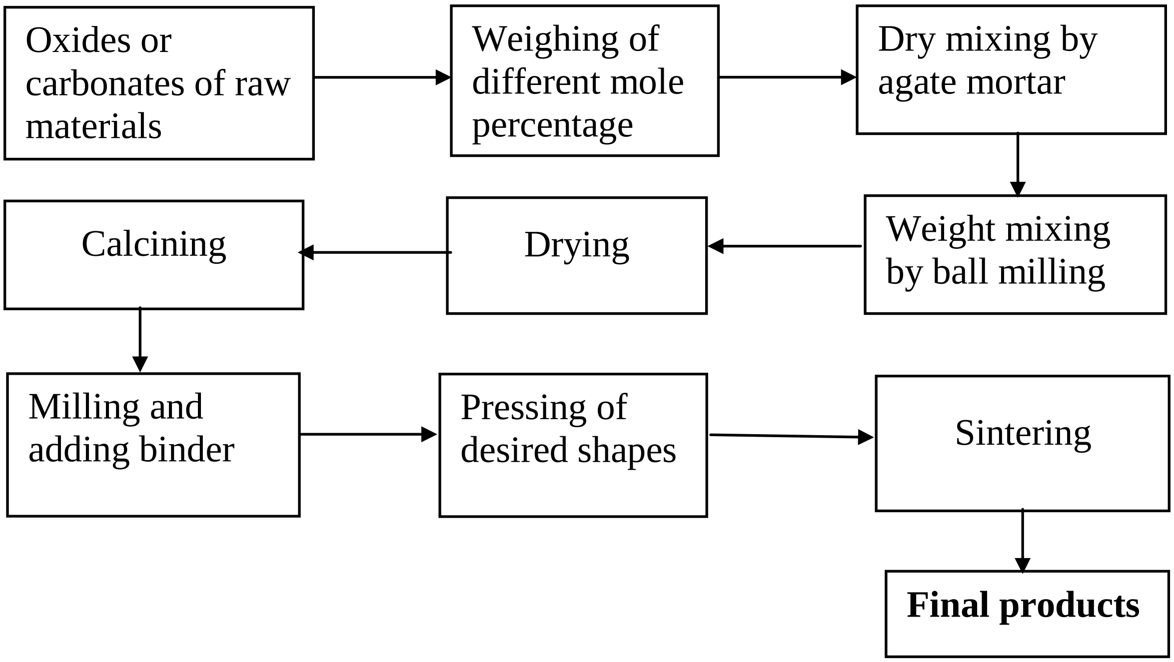

References:

[1] O. Kubo, T. Ido, H. Yokoyama, IEEE Trans. Magn., 18 (1982) 1122.

[2] Tohoku Metal Industries Ltd., Magnetic Recording Powders, 6 (1984) 59207.

[3] T. Ogasawara, M.A.S. Oliveria, J. Magn. Magn. Meter., 27 (2000) 147.

[4] J. C. Bemica, Mater. Sic. Eng. A, 109 (1989) 233.

[5] G. K. Thompson, B. J. Evans, J. Appl. Phys., 73 (1993) 6295.

[6] D. Mishra, Ph D thesis, Bergampur University, Bergampur, India, (2003).

[7] A. Bhaskar, B. Rajini Kanth, S.R. Murthy, J. Magn. Magn. Mater., 283 (2004) 109.

[8] Z. Yue, J. Zhou, Z. Gui, J. Magn. Magn. Mater., 233 (2001) 224.

[9] B. T. Shirk, W. R. Buessem, J. Am. Ceram. Soc., 53 (1970) 192.

[10] M. Mastuoka, et (11., IEEE Trans. Magn., 18 (1982) 1119.

[11] R. H. Anendt, J. Solid State Chem, 8 (1973) 339.

[12] M. C. Blesa, U. Amador, E. Moran, N. Menendez, J. D. Tornero, J. Rodriguez- Carvajal, Sol. Stat. Ion. 63 (1993) 429.

[13] Houpert, M. Hervieu, D. Groult, F. Studer, and M. Toulemonde, Nuclear Instruments and Methods in Physics Research Section B: Beam Intera. With Mater. And Atoms, 32 (1988) 393.

[14] F. Brailsford. Physical Priciples of Magnetism. London: D Nan Nostrand Company Ltd. (1966).

[15]. Mosby’s Medical; Nursing and Allied Health Dictionary; Fourth Edition, Mosby-Year Book Inc. (1994) 243.

[16] Y. Xu ;“Ferroelectric Materials and Their Applications”; Elsevier Science Pub Co., New York, USA (1991).

[17] V. Sinter, "Oxford English Dictionary Second Edition on CD-ROM", Oxford University Press, Version 4.0 (2009).

[18] "Sinter", The Free Dictionary, (2014).

[19] Y. Xu, “Ferroelectric Materials and their Applications”, Elsevier science Pub. Co., New York, USA (1991).

[20] J. F. Duncan, K. J. D. MacKenzie, D. J. Stewart, In Symposia of the Faraday Soci. Royal Soci. Chem., 1 (1967) 103.

[21] M. Zaharescu, M. Balasoiu, M. Crisan, D. Crisan, T. Tavala, V. Moser, Revue roumaine de chimie, 29 (1984) 247.

CHAPTER 4

EXPERIMENTAL PROCEDURES

CHAPTER 4

EXPERIMENTAL PROCEDURES

4.1 X Ray diffraction analysis

X-Ray diffraction is one of the X-Ray scattering techniques, which are nondestructive analytical technique revealing information about the crystallographic structure, chemical composition, and physical properties of materials. When X-rays interact with a crystalline substance (Phase), one gets a diffraction pattern. An electron in an alternating electromagnetic field will oscillate with the same frequency as the field. When an X-ray beam hits an atom, the electrons around the atom start to oscillate with the same frequency as the incoming beam. In almost all directions we will have destructive interference, that is, the combining waves are out of phase and there is no resultant energy leaving the solid sample.

XRD is based on constructive interference of monochromatic X-Rays and a crystalline sample. The monochromatic X-rays are generated by a cathode ray tube, filtered to produce monochromatic radiation, collimated to concentrate them and directed toward the sample. Let us consider an incident X-ray beam interacting with the atoms arranged in a periodic manner as shown in two dimensions in figure 4.1.

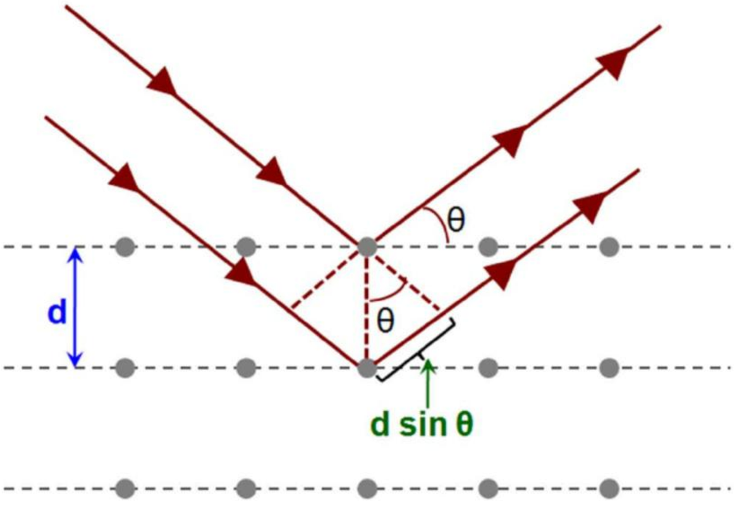

Figure 4.1: Bragg’s law of diffraction (adapted from ref. [1])

The interaction of the incident rays with the sample produces constructive interferences (and a diffracted ray), when conditions satisfy Bragg’s law. In accordance with Bragg's law when X-rays hit an atom, they make the electronic cloud move as does any electromagnetic wave. The interference is constructive when the phase shift is a multiple of 2π; this condition can be expressed by Bragg's law [2,3]:

$$n\lambda = 2d \sin\theta \tag{4.1}$$

Where, d is the distance between the crystal planes and n is an integer, λ is the wavelength of the x-ray. From different peaks in XRD spectra, the phase identification can be possible in terms of different sets of d spacing for a certain material. From the law, we find that the diffraction is only possible when $\lambda < 2d$ [4].

This law relates the wavelength of electromagnetic radiation(λ) to the diffraction angle(Θ) , and the lattice spacing (d) in a crystalline sample. these diffracted X-rays are then detected, processed and counted.

By scanning the sample through a range of angles(Θ), all possible diffraction directions of the lattice should be attained, due to the random orientation of the powdered material. conversion of the diffraction peaks to d-spacing allows identification of the mineral because each mineral has a set of unique d-spacing. Typically, this is achieved by comparison of d-spacing with standard reference pattern.

The orientation and inter planar spacing of these planes are defined by the three integers (h k l) called indices. A given set of planes with indices (h k l) cut the a-axis of the unit cell in h sections, the b-axis in k sections and the c-axis in l sections. A zero indicates that the planes are parallel to the corresponding axis. e.g. the (2 2 0) planes cut the a– and the b– axes in half, but are parallel to the c– axis.

The structural characterization was carried out by X-ray diffractometer with CuKα radiation of wavelength, λ= 1.54178Å. XRD patterns of all samples were collected over a 2θ range of 15–60º using a step size 0.01 degree.

The lattice parameter for each peak of each sample was calculated by using the formula (for cubic spinel structure)

$$a = d\sqrt{h^2 + k^2 + l^2} \tag{4.2}$$

where h, k and l are the indices of the crystal planes. To determine the exact lattice parameter for each sample, Nelsion-Riley method was used. The Nelsion-Riley Function F(θ) is given as

$$F(\theta) = \frac{1}{2}[(Cos^2\theta / Sin\theta) + (Cos^2\theta / \theta)] \tag{4.3}$$

The values of lattice constant 'a' of all the peaks for a sample are plotted against F(θ). Then using a least square fit method exact lattice parameter 'a_o' is determined. The point where the least square fit straight line cut the y-axis (i.e. at F(θ) = 0) is the actual lattice parameter of the sample [4]. The theoretical density ρ_{th} was calculated using following expression:

$$\rho_{th} = \frac{8M}{N_A a_0^3} g/cm^3 \quad (4.4)$$

where N_A is Avogadro's number (6.023×10^{23} moleculesmol^{-1}), M is the molecular weight. The porosity was calculated from the relation $\{100(\rho_{th} - \rho_B)/\rho_{th}\}\%$ where ρ_B is the bulk density measured by the Archimedes' principle. Bulk density of sintered specimens was determined by Archimedes principle. Sintered samples were weighed in air. Samples were immersed in water to ensure that water filled up the open pores completely. The bulk density was calculated as follows:

$\rho_B = \frac{W_1}{W_1 - W_2} \times \rho$, where ρ the density of water at room temperature, W_1 is the weight of the sample in air and W_2 is the weight of the sample in water.

4.1.1 Interpretation of the XRD Data

The XRD data consisting of θ_{hkl} and d_{hkl} values corresponding to the different crystallographic planes are used to determine the structural information of the samples like lattice parameter and constituent phase. Normally, lattice parameter of a composition is determined by the Debye-Scherrer method after extrapolation of the curve. We would like to understand how the value of lattice parameter changes with the increase of yttrium content in the Mn-Ni-Zn ferrites. We determine the lattice spacing (inter planer distance), d using the following equation [5] which is related to the measurement of lattice parameter, X-ray density and porosity.

$$2d_{hkl} \sin\theta = \lambda$$

i.e. $d_{hkl} = \frac{\lambda}{2 \sin\theta}$ (4.5)

(i) Lattice parameter

The lattice parameters from XRD of the samples are calculated by using the following relations;

$\frac{1}{d_{hkl}^2} = \frac{h^2+k^2+l^2}{a^2}$(For cubic) (4.6)

$$\frac{1}{d_{hkl}^2} = \frac{4(h^2+hk+k^2)}{3a^2} + \frac{l^2}{c^2} \text{ (For rhombohedral)} \qquad (4.7)$$

$$\frac{1}{d_{hkl}^2} = \frac{h^2}{a^2} + \frac{k^2}{b^2} + \frac{l^2}{c^2} \text{ (For orthorhombic)} \qquad (4.8)$$

$$\frac{1}{d_{hkl}^2} = \frac{h^2+k^2}{a^2} + \frac{l^2}{c^2} \text{(For tetragonal)} \qquad (4.9)$$

Here, *h, k, l* are miller indices of the crystal plane.

In this work, we have considered 8 prominent reflection planes for a cubic crystal,

$$a = d_{hkl}\sqrt{h^2 + k^2 + l^2} \qquad (4.10)$$

Where, a is the lattice parameter and hkl are the Miller indices.

To get the exact value of lattice parameters we have used Nelson-Riley method. The Nelson-Riley function can be written as,

$$F(\theta) = \frac{1}{2}\left(\frac{cos^2\theta}{sin\theta} + \frac{cos^2\theta}{\theta}\right) \qquad (4.11)$$

We have drawn 'a' vs $F(\theta)$ graph. From this graph we have determined the value of 'a' at $F(\theta) = 0$ by using the linear fitting method. This is the exact value of 'a'.

(ii) X-ray Density, Bulk Density and porosity

Using the value of 'a' we have calculated the X-ray density of Mn-Ni-Zn ferrites. The X-ray density is defined as

$$\rho_x = \frac{8M}{Na^3} gm/cm^3 \qquad (4.12)$$

Where, N is the Avogadro's number and M is the molecular mass.

The bulk density of the samples were also calculated by using the formula

$$\rho_B = \frac{M}{V} \qquad (4.13)$$

And finally we have measured the porosity of the samples using the formula given below[6],

$$P = \left(1 - \frac{\rho_B}{\rho_x}\right) \times 100\% \qquad (4.14)$$

4.1.2 Phillips X'Pert PRO X-ray diffractometer

X-ray diffraction (XRD) provides extensive information on the crystal structure. The wavelength of an X-ray is of the same order of magnitude as that of the lattice constant of crystals and this makes it so useful in structural analysis of crystal structure.

To study the crystalline phases of the prepared samples Phillips Pro XRD system PW 3040 diffraction meter 50 was used in the Bangladesh Atomic Energy Center, Dhaka.

Figure 4.2: Internal arrangement of a PHILIPS PW3040 X' Pert PRO X-ray diffractometer (Adapted from ref. [7])

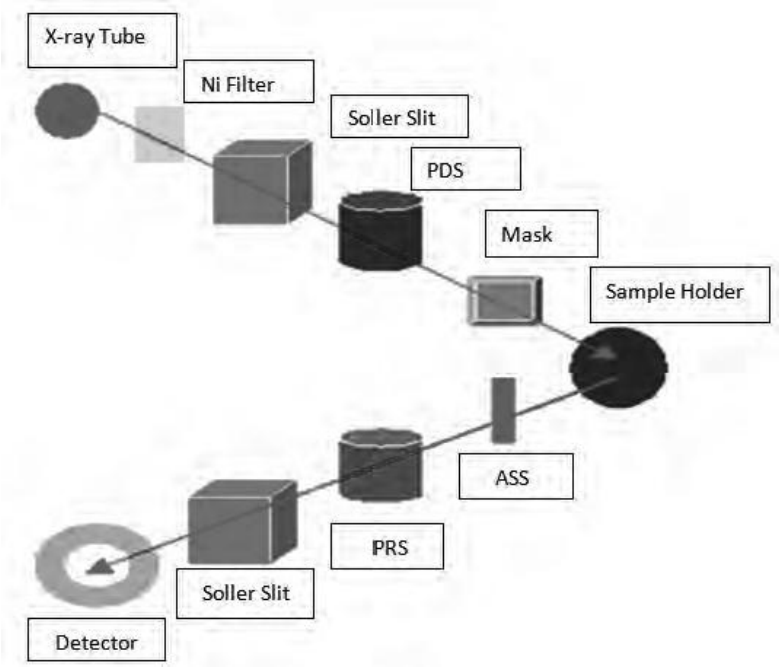

Figure 4.3: Block diagram of the PHILIPS PW 3040 XPert PRO XRD system (Adapted from ref. [8])

The specimens were exposed to CuKα radiation of wavelength, λ = 1.54178 Å with a primary beam of 40 kV and 30 mA with a sampling pitch of 0.02° and time for each step data collection was 1.0 sec.

4.1.3 Powder X-ray diffractometer

Powder X- ray diffraction is perhaps the most widely used x –ray diffraction technique for characterizing materials, Powder diffraction is commonly used to identify unknown substances, by comparing diffraction database maintained by the International Center for Diffraction Data. It may also be used to characterize heterogeneous solid mixtures to determine relative abundance of crystalline compounds and, when coupled with lattice refinement technique, such as Rietvelt refinement, can provide structural information on unknown materials. Powder diffraction is also a common method for determining strains in crystalline materials.

Powder diffraction data can be collected using either transmission or reflection geometry. Because the particles in the powder sample are randomly oriented, these two methods will yield the same data. Powder diffraction data are measured using the Philips XPERT PRO diffractometer, which measures data in the reflection mode and is used mostly with powder or solid samples. Diffraction can occur when electromagnetic radiation interacts with a periodic structure whose distance is about the same as the wavelength of the radiation. This technique uses the principle that waves interacting with atomic planes in a material will exhibit the phenomenon of diffraction. X-rays incident on a sample are scattered off at an equal angle. At certain angles of incidence, x-rays scattering off of neighboring parallel planes of atoms will interferer destructively. At other angles, these waves will interfere constructively and result in a large output signal at those angles. The XRD technique is based on Bragg's principle. Bragg reflection is a coherent elastic scattering in which the energy of the X-ray is not changed on reflection.

Figure 4.4: Phillips Pro XRD system PW 3040 diffraction meter 50 [picture taken from Bangladesh Atomic Energy Centre, Dhaka]

4.2 Scanning electron microscope

The scanning electron microscope (SEM) is a type of electron microscope that images the sample surface by scanning it with a high energy beam of electrons in a raster scan pattern. The scanning electron microscope (SEM) uses a focused beam of high-energy electrons to generate a variety of signals at the surface of solid specimens. The electrons interact with the atoms that make up the sample producing signals that contain information about the sample's surface topography, composition and other properties such as electrical conductivity. The electron gun at the top of the column produces a high-energy beam, which is focused into a fine spot (4 nm in diameter) on the specimen. Secondary electrons are produced on the specimen surface and are detected by a suitable detector. The amplitude of the secondary electron signal varies with time according to the topography of the specimen surface. then the signal is amplified and used to display the corresponding specimen information. The SEM has a large depth of field, which allows a large amount of the sample to be in focus at one time. The SEM also produces images of high resolution, which means that closely spaced features can be examined at a high magnification. Preparation of the samples is relatively easy since most SEMs only require the sample to be conductive. The types of signals produced by an SEM include secondary electrons, back-scattered electrons (BSE), characteristic X-rays, light (cathode luminescence), specimen current and transmitted electrons. Secondary electron detectors are standard equipment in all SEMs, but it is rare that a single machine would have detectors for all other possible signals [9]. The signals result from interactions of the electron beam with atoms at various depths within the sample.

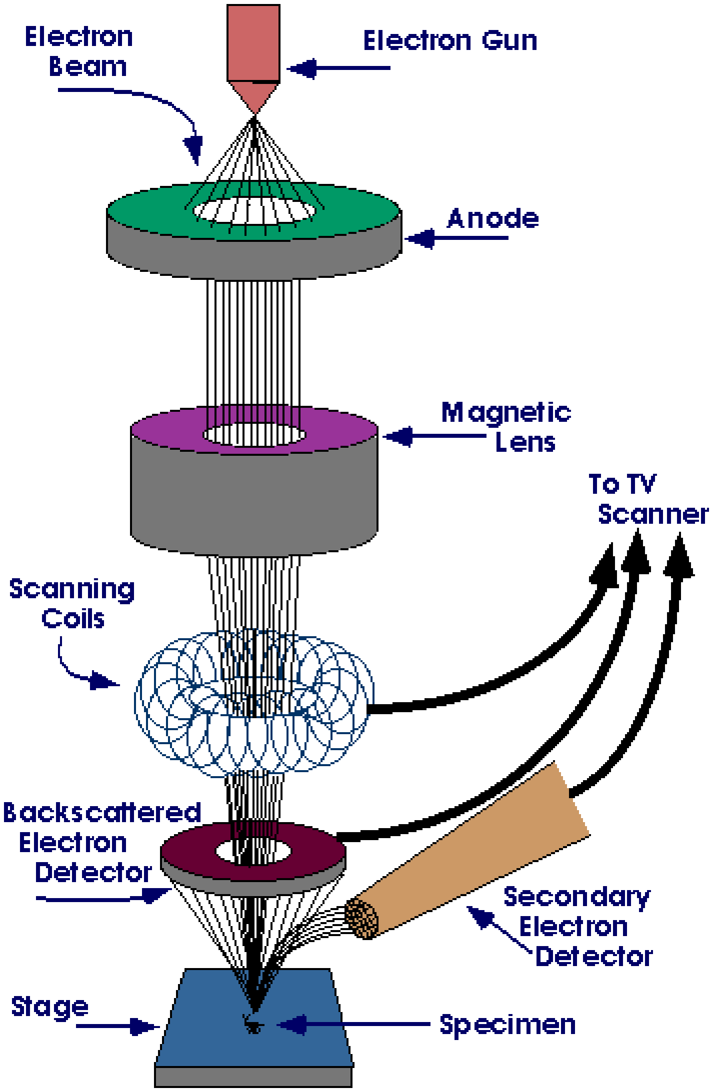

Figure 4.5: Schematic diagram of Scanning electron microscope (adapted from ref. [10])

Essential components of all SEMs include the following:

- Electron Source ("Gun")
- Electron Lenses
- Sample Stage

- Detectors for all signals of interest
- Display / Data output devices

Infrastructure Requirements:

- Power Supply
- Vacuum System
- Cooling system
- Vibration-free floor
- Room free of ambient magnetic and electric fields

SEMs always have at least one detector (usually a secondary electron detector), and most have additional detectors. The specific capabilities of a particular instrument are critically dependent on which detectors accommodates it. In the most common or standard detection mode, secondary electron imaging or SEI, the secondary electrons are emitted from very close to the specimen surface. Consequently, SEM can produce very high-resolution images of a sample surface, revealing details less than 1 nm in size. Back-scattered electrons (BSE) are beam electrons that are reflected from the sample by elastic scattering. They emerge from deeper locations within the specimen and consequently the resolution of BSE images is generally poorer than SEM images. However, BSE are often used in analytical SEM along with the spectra made from the characteristic X-rays, because the intensity of the BSE signal is strongly related to the atomic number (Z) of the specimen. BSE images can provide information about the distribution of different elements in the sample. For the same reason, BSE imaging can image colloidal gold immuno-labels of 5 or 10 nm diameter, which would otherwise be difficult or impossible to detect in secondary electron images in biological specimens. Characteristic X-rays are emitted when the electron beam removes an inner shell electron from the sample, causing a higher-energy electron to fill the shell and release energy. These characteristic X-rays are used to identify the composition and measure the abundance of elements in the sample. Due to the very narrow electron beam, SEM micrographs have a large depth of field yielding a characteristic three-dimensional appearance useful for understanding the surface structure of a sample. This is exemplified by the micrograph of pollen shown above. A wide range of magnifications is possible, from about 10 times (about equivalent to that of a powerful handles) to more than 500,000 times, about 250 times the magnification limit of the best light microscopes.

4.2.1 Scanning Process and Image Formation

In a typical SEM, an electron beam is thermionically emitted from an electron gun fitted with a tungsten filament cathode. Tungsten is normally used in thermionic electron guns because it has the highest melting point and lowest vapor pressure of all metals, thereby allowing it to be electrically heated for electron emission, and because of its low cost. Other types of electron emitters include lanthanum hexaboride (LaB_6) cathodes, which can be used in a standard tungsten filament SEM if the vacuum system is upgraded or field emission guns (FEG), which may be of the cold-cathode type using tungsten single crystal emitters or the thermally assisted Schottky type, that use emitters of zirconium oxide.

The electron beam, which typically has an energy ranging from 0.2 kV to 40 kV, is focused by one or two condenser lenses to a spot about 0.4 nm to 5 nm in diameter. The beam passes through pairs of scanning coils or pairs of deflector plates in the electron column, typically in the final lens, which deflect the beam in the x and y axes so that it scans in a raster fashion over a rectangular area of the sample surface. When the primary electron beam interacts with the sample, the electrons lose energy by repeated random scattering and absorption within a teardrop-shaped volume of the specimen known as the interaction volume, which extends from less than 100 nm to approximately 5 μm into the surface. The size of the interaction volume depends on the electron's landing energy, the atomic number of the specimen and the specimen's density. The energy exchange between the electron beam and the sample results in the reflection of high-energy electrons by elastic scattering, emission of secondary electrons by inelastic scattering and the emission of electromagnetic radiation, each of which can be detected by specialized detectors.

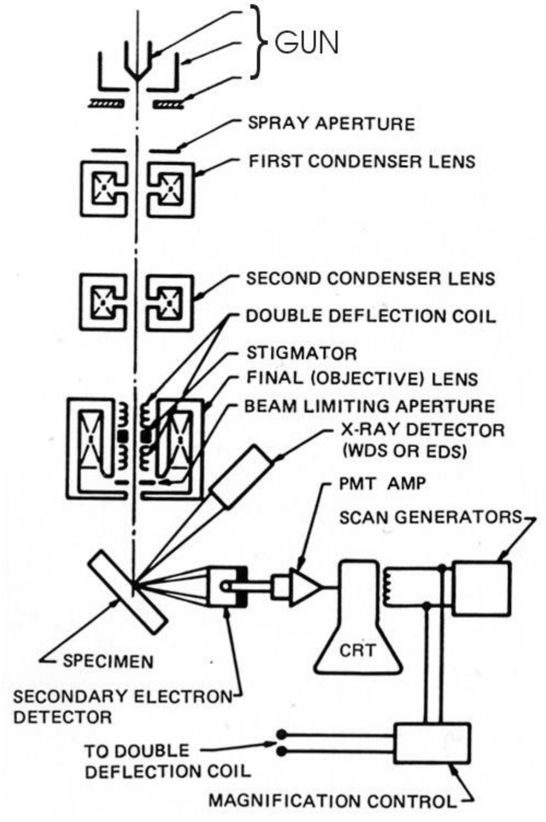

Figure 4.6: Schematic diagram of Scanning electron microscope (adapted from ref. [11])

The beam current absorbed by the specimen can also be detected and used to create images of the distribution of specimen current. Electronic amplifiers of various types are used to amplify the signals, which are displayed as variations in brightness on a computer monitor (or, for vintage models, on a cathode ray tube). Each pixel of computer video memory is synchronized with the position of the beam on the specimen in the microscope, and the resulting image is therefore a distribution map of the intensity of the signal being emitted from the scanned area of the specimen. In older microscopes images may be captured by photography from a high-resolution cathode ray tube, but in modern machines they are digitized and saved as digital images [12].

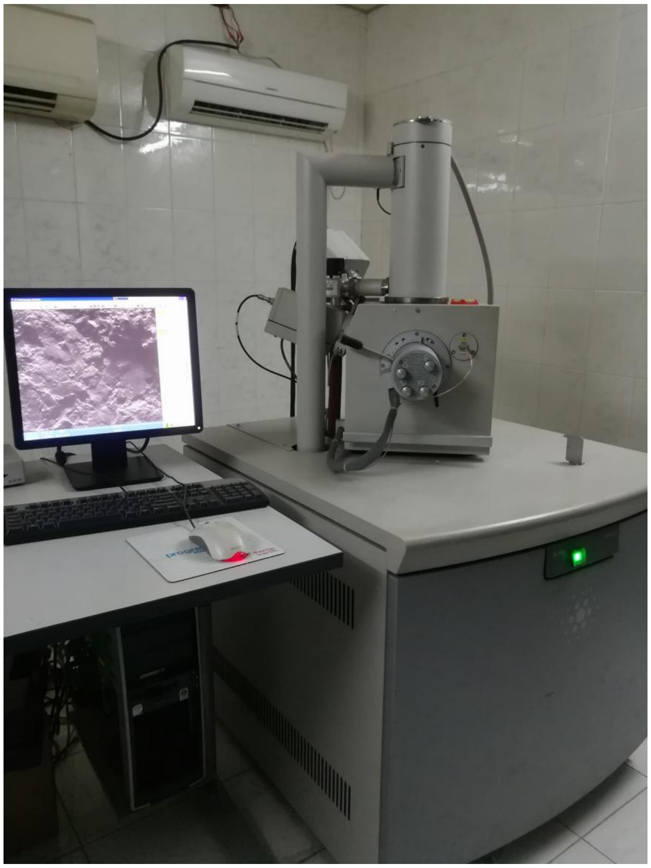

Figure 4.7: FEI scanning electron microscope [picture taken from Bangladesh Atomic Energy Centre, Dhaka]

4.3 Dielectric properties measurement

A dielectric is an electrical insulator that may be polarized by the action of an applied electric field. When a dielectric material is placed in an electric field, electric charge does not flow through the material, as in a conductor, but only slightly shift from their average equilibrium positions causing dielectric polarization: positive charges are displaced along the field and negative charges shift in the opposite direction.

dielectric typically means materials with a high polarizability. The latter is expressed by a number called the relative permittivity (also known in older texts as dielectric constant). A common example of a dielectric is the electrically insulating material between the metallic plates of a capacitor. The polarization of the dielectric by the applied electric field increases the capacitor's surface charge for the given electric field strength.

The dielectric properties were measured using Wayne Kerr impedance analyzer 6500 B series. Experimental set up is shown in Figure 4.9.

To measure the dielectric constants, at first we have polished the pellet shaped samples to remove any roughness and coated the two surfaces of each pellet with silver paste as contact material. We have measured the dielectric constants as a function of frequency for various samples in the range of 1 KHz-120 MHz at room temperature by using WAYNE KERR PRECISION IMPEDANCE ANALYZER 6500B at Atomic Energy Centre, Dhaka. The real part of dielectric constant was calculated using the formula,

$$\varepsilon' = \frac{CL}{\varepsilon_0 A} \qquad (4.15)$$

Where, C is the capacitance of the pellet, L is the thickness or height of the pellet, A is the area of cross-section of the flat surface of the pellet, ε_0 is the dielectric constant at free space.

The imaginary part of the dielectric constant is defined as,

$$\varepsilon'' = \varepsilon' \times \tan\delta \qquad (4.16)$$

The quality factor was measured using the formula

$$Q = \frac{1}{\tan\delta} \qquad (4.17)$$

And the relative quality factor,

$$RQF = \frac{\varepsilon'}{\tan\delta} \qquad (4.18)$$

4.4 Resistivity Measurement:

Conventional two-probe method was used to measure the resistivity of the pellet shaped sample. At first we have polished the pellet shaped samples to remove any roughness and coated the two surfaces of each pellet with silver paste as contact material for measuring resistivity. Resistivity was calculated as a function of both frequency and temperature. To determine the temperature dependent resistivity, we have used "KEITHLEY 6514 SYSTEM ELECTROMETER" a small oven and a thermocouple based thermometer.

The resistivity was calculated using the formula,

$$R = \frac{\rho L}{A} \qquad (4.19)$$

Where, ρ is the specific resistance, L is the length of the specimen and A is the area of cross section.

From the temperature dependent resistivity, we have calculated the activation energy using the formula given below,

$$\rho = \rho_o e^{\left(\frac{E_a}{K_B T}\right)} \qquad (4.20)$$

Where, E_a represents the activation energy, ρ is the specific resistance in ohm-cm, K_B is the Boltzmann constant and T is the temperature in Kelvin.

Figure 4.8: Keithley 6514 System Electrometer [picture taken from Bangladesh Atomic Energy Centre, Dhaka]

4.5 Impedance Analyzer

The dielectric constant, the permeability and frequency dependent resistance have been measured by the Weyne Kerr Impedance Analyzer. The term "impedance" was coined by Oliver Heaviside in July 1886 [13,14]. Arthur Kennelly was the first to represent impedance with complex numbers in 1893 [15]. Electrical impedance is the measure of the opposition that a circuit presents to a current when a voltage is applied. In quantitative terms, it is the complex ratio of the voltage to the current in an alternating current (AC) circuit. Impedance extends the concept of resistance to AC circuits, and possesses both magnitude and phase, unlike resistance, which has only magnitude. When a circuit is driven with direct current (DC), there is no distinction between impedance and resistance; the latter can be thought of as impedance with zero phase angle. Depending on the sample material, the requirements to the impedance analyzer are extraordinary high and the result quality and availability strongly depends on its performance. In practice one is generally not so much interested in extreme high accuracy, but to measure both components of impedance $Z(\omega)$, permittivity $\varepsilon(\omega)$ or conductivity $\sigma(\omega)$ at all. Beside the frequency range, the permittivity, the permeability and the tanδ or phase accuracy are the most important performance parameters.

4.6 Permeability Measurement

For high frequency application, the desirable property of a ferrite is high permeability with low loss. One of the most important goals of ferrite research is to fulfill this requirement. The techniques of permeability measurement and frequency characteristics of the present samples are described in the following way. Measurements of permeability normally involve the measurements of the change in self-inductance of a coil in presence of the magnetic core. The behavior of a self-inductance can now be described as follows. We assume an ideal loss less air coil of inductance 0 L. On insertion of a magnetic core with permeability μ, the inductance will be μL_0. The complex impedance Z of this coil [16] can be expressed as follows:

$$Z = R + jX = j\omega\mu L_0 = j\omega L_0(\mu' - j\mu'') \qquad (4.21)$$

Where R is the resistance and

$$R = \omega L_0 \mu'' \qquad (4.22)$$

And, the reactive part is,

$$X = \omega L_0 \mu' (4.23)$$

Here ω represents the angular frequency. The permeability of the samples can be calculated from the complex impedance of the coil, Z, given by equation (4.21).

Figure 4.9: Wayne Kerr Impedance Analyzer [picture taken from Bangladesh Atomic Energy Centre, Dhaka]

4.7 Frequency Characteristics of the Present Samples

The powder samples were pressed into torroid shape with inner and outer diameter to measure the initial permeability of the samples. The torroid shaped samples were sintered at 1050^{o}C for 2 hours. 5 turns of super enameled doubly insulated copper wire wounded on each torroid to carry out initial permeability μ_i and relative quality factor at room temperature as a function of frequency.

The initial permeability was measured by using the formula [17, 18]

$$\mu_i = \frac{2\pi L_s}{\mu_o N^2 t} \ln\left(\frac{D_{outer}}{D_{inner}}\right) \qquad (4.24)$$

Where, L_s is the inductance in Henry, N is the number of turns of copper wire in the torroid, D_{outer} is the outer diameter and D_{inner} is the inner diameter of the torroid.

Imaginary part of complex permeability is

$$\mu'' = \frac{\mu'}{Q} \qquad (4.25)$$

And the quality factor,

$$Q = \frac{1}{\tan\delta} \qquad (4.26)$$

Relative quality factor,

$$RQF = \frac{\mu'}{\tan\delta} \qquad (4.27)$$

4.8 Magnetic properties measurements

The vibrating sample magnetometer(VSM) is a fast and sensitive DC magnetometer. It is a scientific instrument that measures magnetic properties, invented in 1955 by Simon Foner at Lincoln Laboratory MIT. The paper about his work was published shortly afterward in 1959 [19]. The basic measurement is accomplished by oscillating the sample near a detection coil and synchronously detecting the voltage induced. By using a compact gradiometer pick-up coil configuration, a relatively large oscillation amplitude (1-3 mm peak), and a frequency of 40 Hz, the system can resolve magnetization changes of less than 10-6 emu at a data range of 1 Hz.by vibrating the sample sinusoidally, the induced voltage due to the magnetic moment in the pickup coil is proportional to the samples magnetization but does not depend on the strength of the applied magnetic field. Therefore, by detecting the induced magnetic voltage, it is possible to measure the magnetic field-dependent magnetization hysteresis curve of the materials.

We have measured magnetization as a function of applied magnetic field by using EV9 MICROSENSE VIBRATING SAMPLE MAGNETOMETER in this work and the measurement was carried out at Material Science Division, Atomic Energy Center, Dhaka.

Figure 4.10: EV9 Micro sense vibrating sample magnetometer [Picture taken from Bangladesh Atomic Energy Centre, Dhaka].

4.8.1 Working Principle of vibrating sample magnetometer (VSM)

If a sample is placed in a uniform magnetic field, between the poles of an electromagnet, a dipole moment will be induced. If the sample vibrates with sinusoidal motion a sinusoidal electrical signal can be induced in suitable placed pickup coils. The signal has the same frequency of vibration and its amplitude will be proportional to the magnetic moment, amplitude, and relative position with respect to the pick-up coils system. Figure 4.7 shows the block diagram of vibrating sample magnetometer. The sample is fixed to a sample holder located at the end of a sample rod mounted in an electromechanical transducer. The transducer is driven by a power amplifier which itself is driven by an oscillator at a frequency of 90 Hz. So, the sample vibrates along the Z axis perpendicular to the magnetizing field. The latter induced a signal in the pick-up coil system that is fed to a differential amplifier. The output of the differential amplifier is subsequently fed into a tuned amplifier and an internal lock-in amplifier that receives a reference signal supplied by the oscillator.

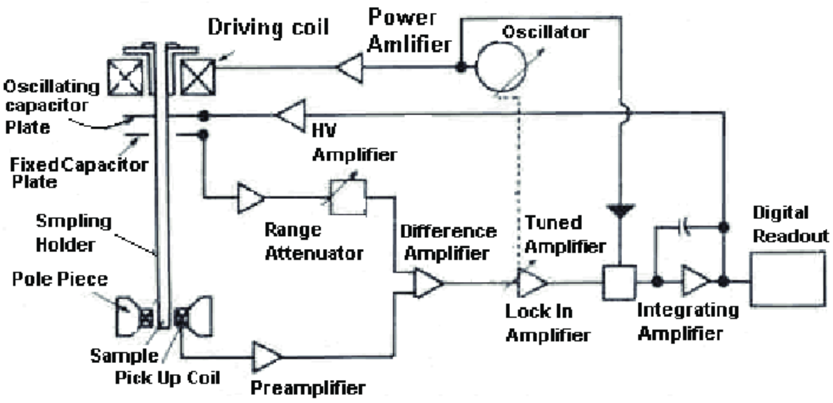

Figure 4.11: Block diagram of Vibrating Sample Magnetometer (adapted from ref. [20]).

The output of this lock-in amplifier, or the output of the magnetometer itself, is a DC signal proportional to the magnetic moment of the sample being studied. The electromechanical transducer can move along X, Y and Z directions in order to find the saddle point. Calibration of the vibrating sample magnetometer is done by measuring the signal of a pure Ni standard of known saturation magnetic moment placed in the saddle point. The basic instrument includes the electromechanical system and the electronic system (including a personal computer). Laboratory electromagnets or superconducting coils of various maximum field strengths may be used.

References:

[1]https://www.researchgate.net/figure/Figure-12-Braggs-law-A-two-dimensional-crystal-lattice-and- a-set-of-imaginary-planes-is-r_47418334_fig10

[2] F. B. E. Warren, X-ray diffraction (Addison-Wesley Publishing Company, Massachusetts, (1968).

[3] B. D. Cullity and S. R. Stock, Elements of x-ray diffraction (Prentice Hall, NJ, 2002).

[4] T. Abbas, M. U. Islam, M. Ch Ashraf, Mod. Phy. Letts. B 9 (1995) 1419.

[5] C. Kittel, “Introduction to Solid State Physics”, 7th Edition, John Wiley and Sons, Inc., Singapore, (1996).

[6] I. I. McColm, N. J. Clark, “Forming, Shaping and Working of High Performance Ceramics”, Glasgow: Blackic, (1988).

[7] http://forum.sci.ccny.cuny.edu/cores/x-ray-diffractometer.

[8] http://html.scirp.org/file/1-4400204x8.png.

[9] C.W. Oatley, W.C. Nixon, Pease RFW, Scanning electron microscopy. Adv Electronics Electron Phys 21 (1965) 181.

[10] http://www.purdue.edu/ehps/rem/rs/sem.htm.

[11]http://d32ogoqmya1dw8.cloudfront.net/images/research_education/geochemsheets/techniques/SEM_schematic.JPG.jpg.

[12] O.C. Wells, The construction of a scanning electron microscope and its application to the study of fibres. PhD Dissertation, Cambridge University (1957).

[13] Science, 18, 1888.

[14] O. Heaviside, "The Electrician", Electrical papers, 212 (1886).

[15] A. Kennelly, "Impedance", AIEE, 1893.

[16] A. Goldman, Handbook of Modern Ferromagnetic Materials, Kulwer Acad. Pub, Boston, U.S.A (1999)

[17] P. Puspitasari, Y. Yahya, N. A. M. Zabidi and N. A. Ahmad, J.Appl. Sci, 11 (2011) 1199.

[18] Agilent Technology Japan, 2003. Agilent 4294A Precision Impedance Analyzer Operational Manual, 7th Edition, Kobe Instrument Division, Hyogo, Japan.

[19] S. Foner, "Versatile and Sensitive Vibrating-Sample Magnetometer". Rev.Sci. Instrum., 30 (1959) 548.

[20]https://www.researchgate.net/figure/319256244_Block-diagram-of-vibrating-sample magnetometer-VSM.

CHAPTER 5

RESULT AND DISCUSSION

Chapter 5

Results and Discussion

5.1 X-Ray Diffraction (XRD)

Zn substituted Cobalt Ferrites with general formula $Co_{1-x}Zn_xFe_2O_4$(x=0.0-0.5) were synthesized by Double Sintering Solid State Reaction method. All ferrites are sintered at 1050˚C for two hours in air. Structural and surface morphology are studied by XRD and high resolution optical microscope. XRD patterns confirm their single phase and cubic spinel structure. The effects of Zn ion substitution on the structural parameters of ferrites $Co_{1-x}Zn_xFe_2O_4$(x=0.0-0.5) are discussed below.

Structural characterization and identification of phases are prior for the study of ferrite properties. Optimum magnetic and transport properties of ferrites necessitate having single phase cubic structure. X-ray, neutron and electron diffraction are useful techniques to evaluate the various phases of the synthesized ferrites as well as their unit cell parameters.

The nature of the peak changes in composition. The absence of extra peaks indicates that all the compositions contains only single phase of spinel structure. The well- defined peaks confirm spinel cubic structure formation. The small half width of each peak indicated the large crystalline size [1].

The X-Ray diffraction (XRD) patterns of the studied samples are given in Fig.5.1-5.3 which was obtained from θ-2θ geometry with Cu-K_α radiation. The fundamental reflections from the planes of (220), (311), (511), (440) characterizing the cubic spinel structures are strongly observed. Reflection from the other planes (400), (422) has been observed with weak intensities. Some impurity peaks are detected due to Fe_2O_3 and CoO [2]. It is conjectured that these impurity peaks are the result of few unwanted chemical reactions at the time of sintering . The analysis of XRD patterns indicate that the studied Co-Zn ferrite samples have spinel cubic structures with a single phase [3]. The sharp peak reveals that the samples are in good crystalline form.

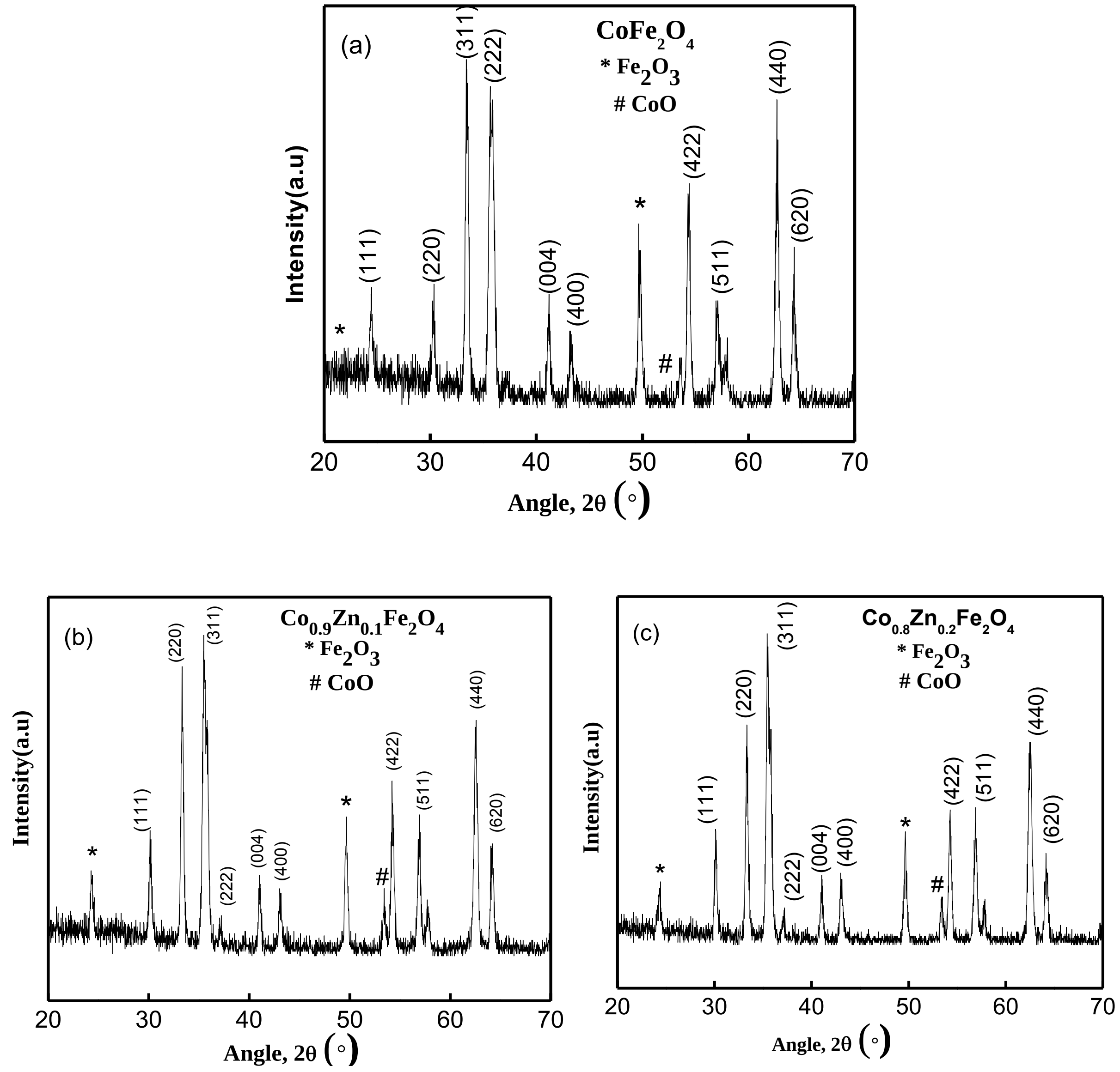

Figure 5.1: X-ray diffraction patterns for (a)x=0.0, (b)x=0.1, (c)x=0.2 of $Co_{1-x}Zn_xFe_2O_4$ferrites.

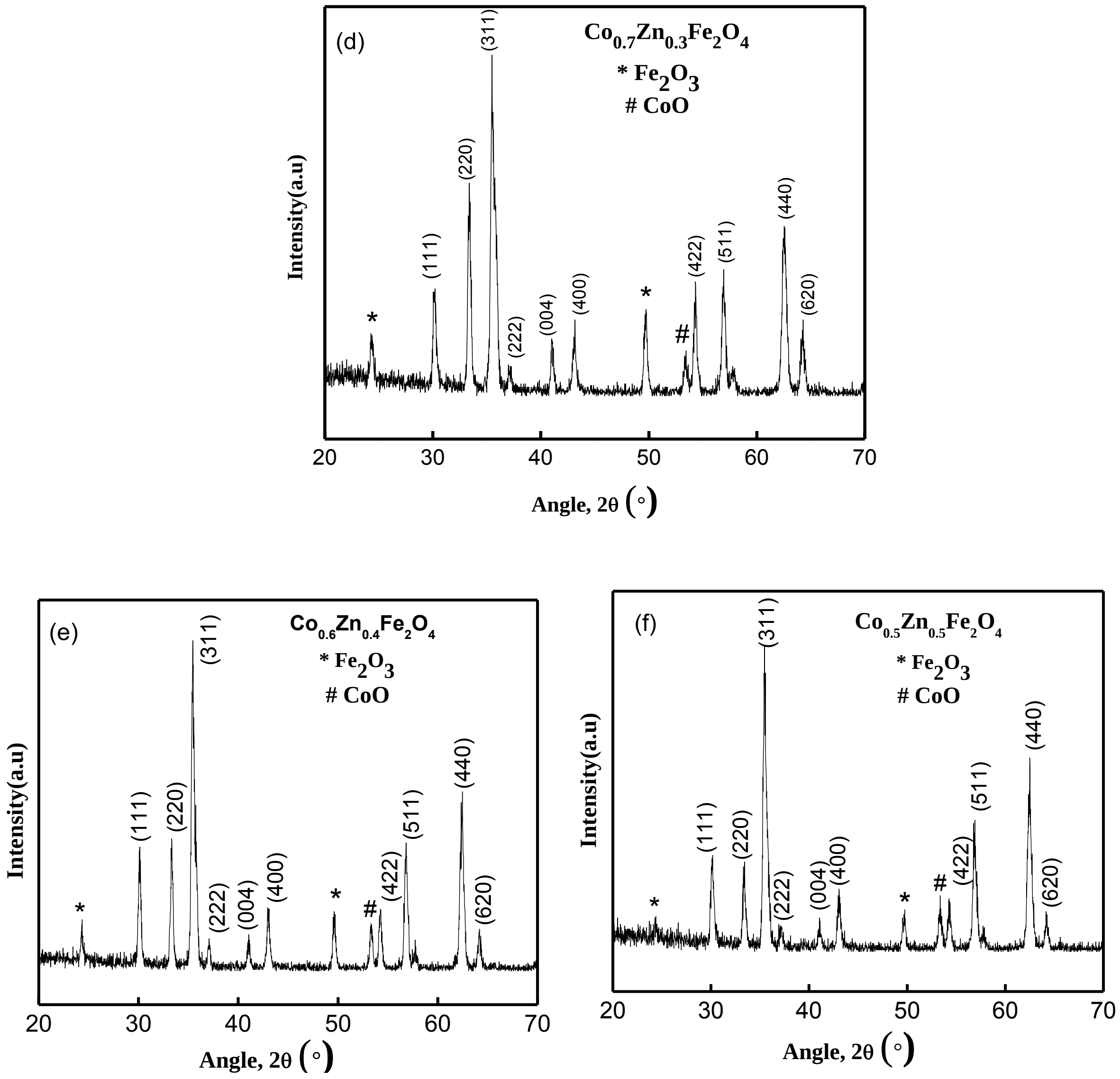

Figure 5.2: X-ray diffraction patterns for (d)x=0.4, (e)x=0.5, (f)x=0.6 of $Co_{1-x}Zn_xFe_2O_4$ferrites.

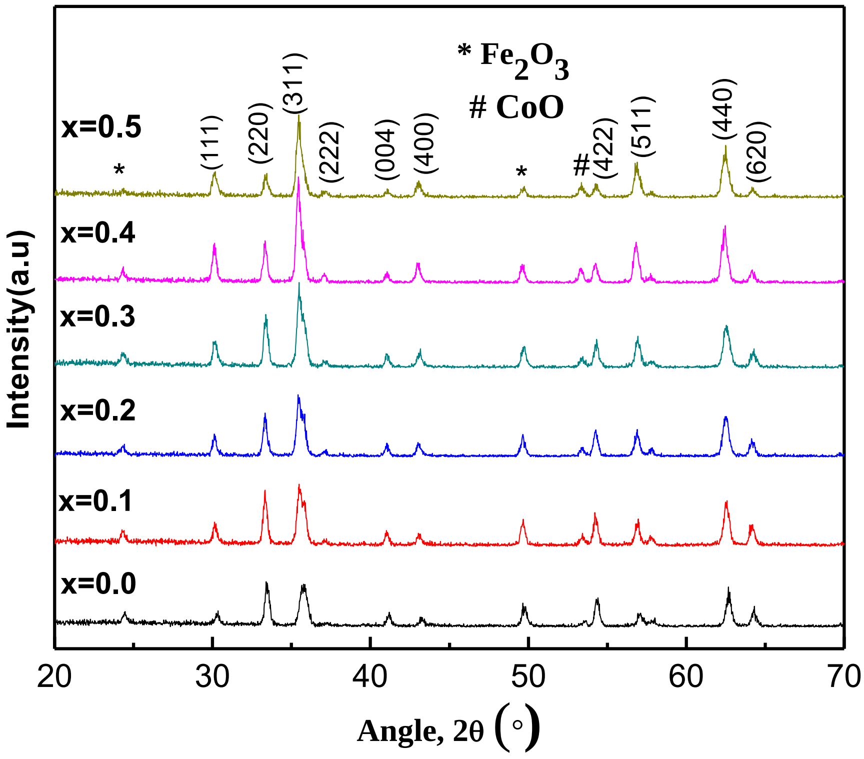

Figure 5.3: X-ray diffraction patterns for $Co_{1-x}Zn_xFe_2O_4$(x=0.0-0.5) ferrites.

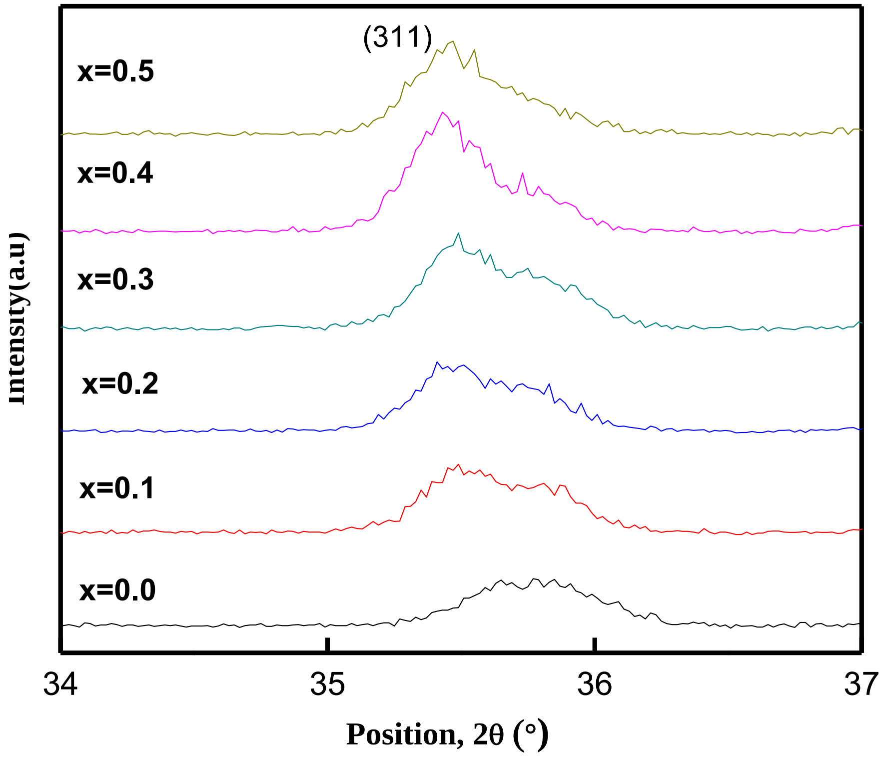

Figure 5.4: Phase shifting for the highest peak of (311).

.

It is observed from Fig.5.4 that the highest intensity (311) is found at 35.77°,35.49°,35.41°, 35.49°,35.43°and 35.47° for x = 0.00, x = 0.01, x = 0.02, x = 0.03, x = 0.04, and x = 0.05 respectively. In this sample, the highest intensity peak shifted to lower angle with the increase of Zn content. Shifting of highest intensity peak towards lower angle is due to this inter-planar distance and increase in cell volume. The intensity of the highest peak is found to increase with increase of Zn content which indicates the crystallization and spatial position of the substituted atom.

Lattice parameters:

The values of lattice parameters of the samples related to different planes are determined using the equation, $a = d_{hkl}\sqrt{(h^2 + k^2 + l^2)}$. To determine the exact value of lattice parameter, Nelson-Riley (N-R) extrapolation method was used. The N-R function, *F(θ)* is represented by the equation $F(\theta) = \frac{1}{2}[\frac{cos^2\theta}{sin^2\theta} + \frac{cos^2\theta}{\theta}]$, where, θ is the Bragg's angle [4]. The lattice parameters were plotted against the N-R function (Fig 5.5, 5.6, 5.7) to calculate the precise value of lattice parameter using linear least square fit method.

The measured lattice parameter of $Co_{1-x}Zn_xFe_2O_4$(x=0.0-0.5) are 8.01778 Å, 8.06168 Å, 8.10261 Å, 8.76753 Å, 9.25644 Å, and 9.54624 Å respectively. The effect of Zinc substitution on the lattice constant is shown in Fig. 5.6. From this Figure, it is found that the lattice parameter increases with increasing Zn content. This increment may be related to the replacement of Co^{2+} ion with smaller ionic radius (0.745Å) [5] by Zn^{2+} ion with larger ionic radius (0.83 Å) [5]. The remarkable effect in the anomaly shift may arise due to the redistribution of the cations. It can be explained by the redistribution of the ions between the interstitial A-site and B-site of the spinel lattice. Another possible explanation for the observed increase in lattice parameters may be originated from iron vacancies in the samples during the crystallization process due to the introduction of large ions in the octahedral site [6]. Similar trend is observed in the $Co_{1-x}Zn_xFe_2O_4$ nanoparticles synthesized by the co-precipitation method [7].

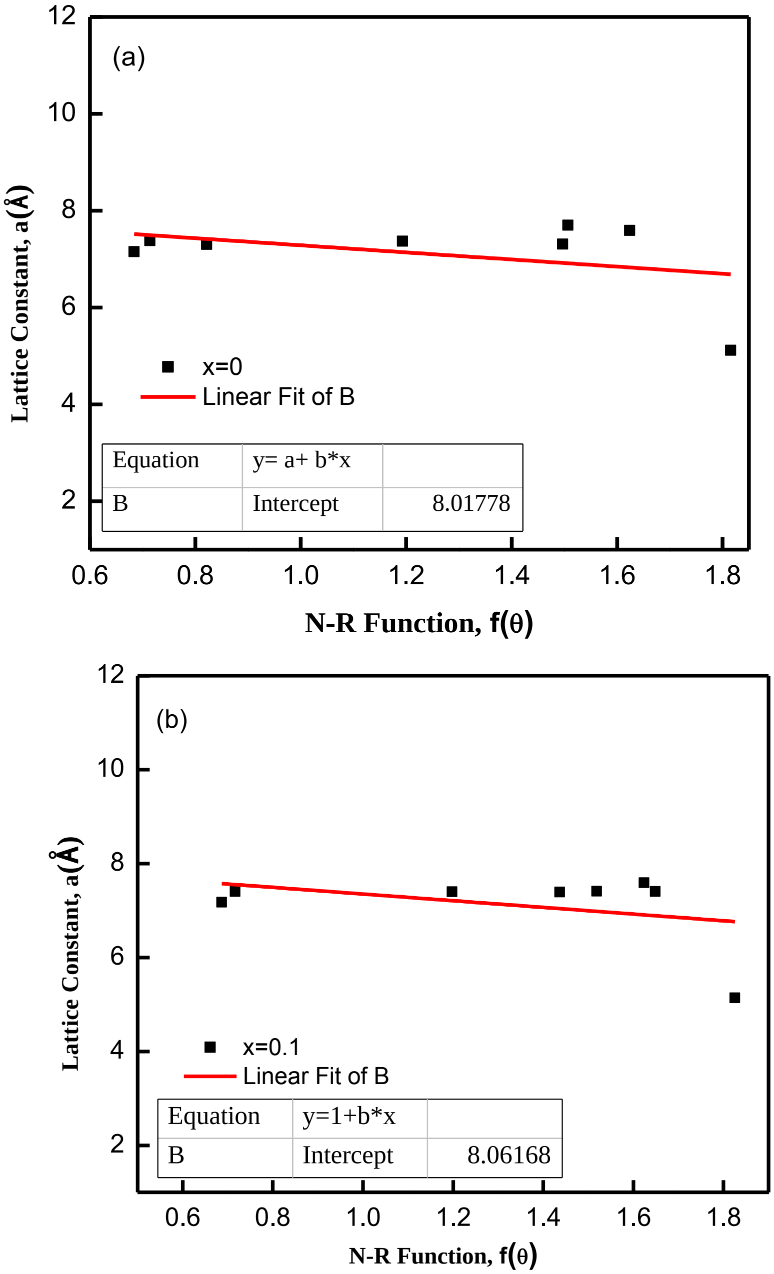

Figure 5.5: Lattice parameter versus N-R function for (a) x = 0.0 and (b) x = 0.1.

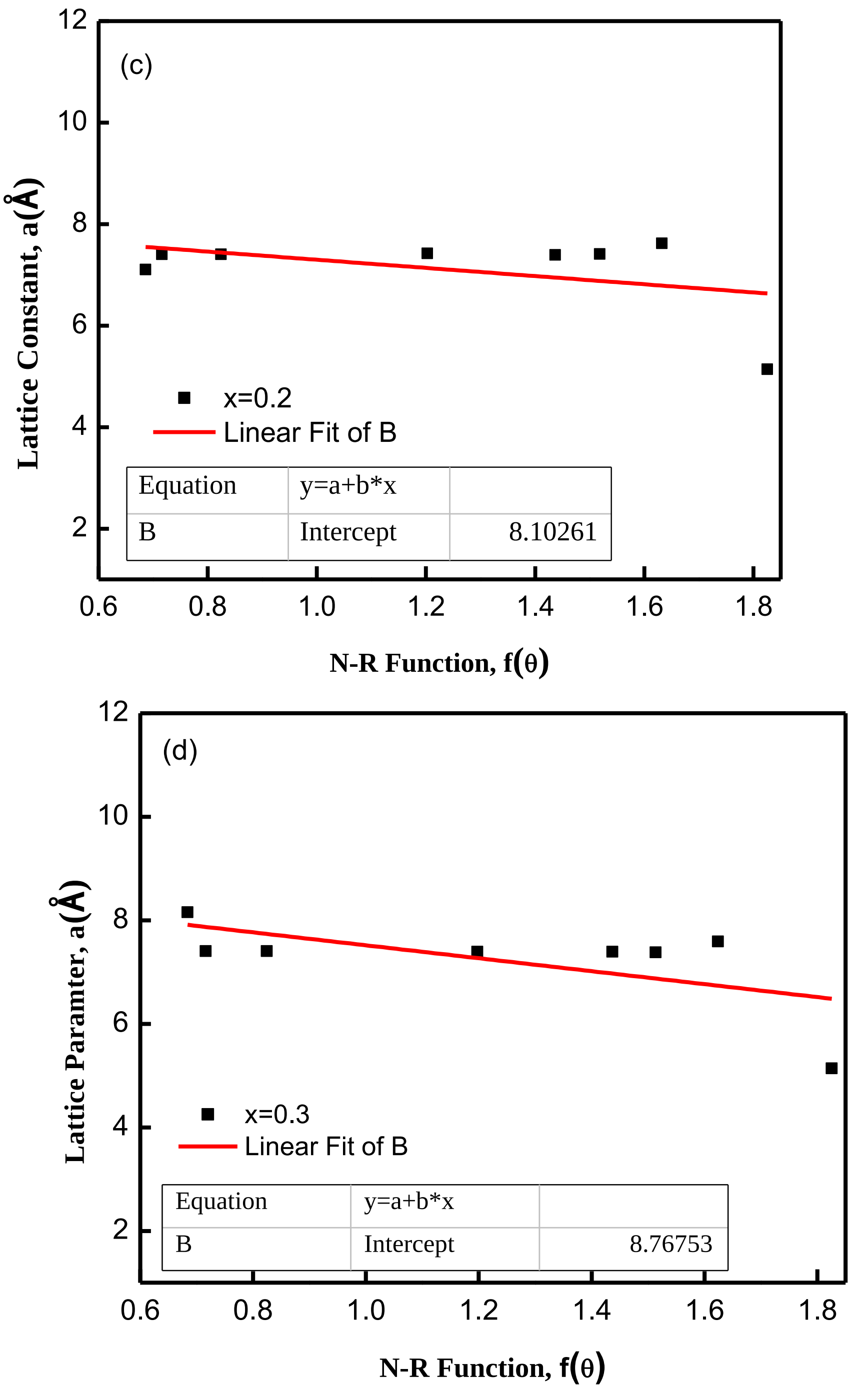

Figure 5.6: Lattice parameter versus N-R function for (c) x = 0.2 and (d) x = 0.3.

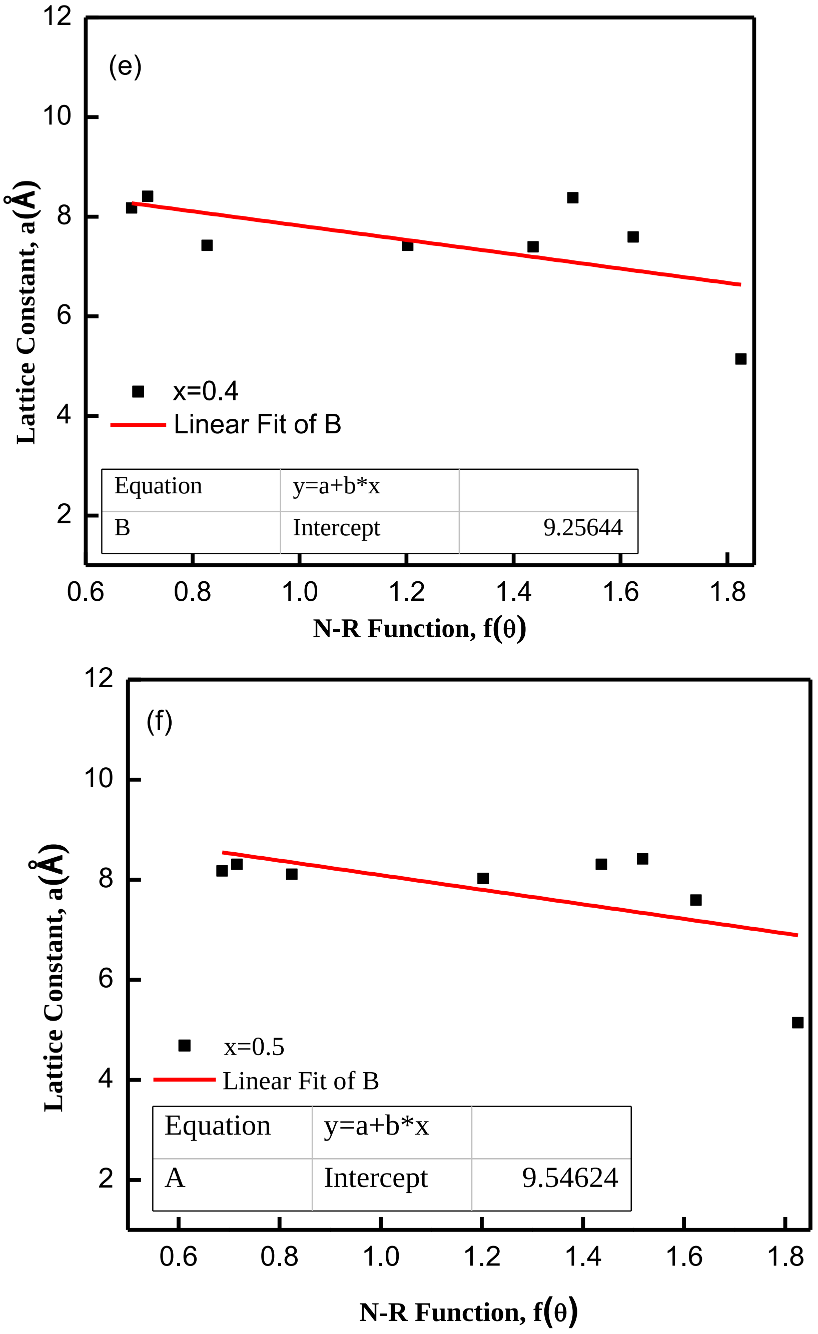

Figure 5.7: Lattice parameter versus N-R function for (e) x = 0.4 and (f) x = 0.5

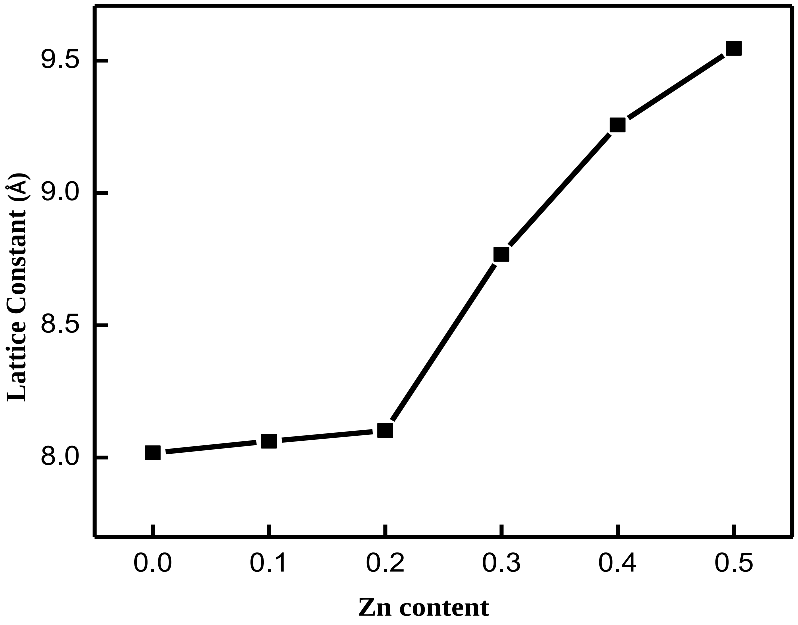

Figure 5.8: Lattice parameter vs Zinc content of $Co_{1-x}Zn_xFe_2O_4$(x=0.0-0.5) ferrites.

The effect of Zn substitution on lattice parameter, X-ray density, Bulk density and porosity is shown in Table -1.

Table 1: Lattice parameter, molecular mass, theoretical density, bulk density and porosity for the samples with the composition $Co_{1-x}Zn_xFe_2O_4$(x=0.0-0.5) (Total mass of samples=12g)

Zn content, x	Molecular mass, M	Sintering temperature T_S	Lattice Constant a(Å)	X-Ray density g/cc	Bulk density g/cc	Porosity P %
0	0	1050˚C	8.01778	5.29	4.181	20.96
0.1	0.41523		8.06168	5.30	4.423	16.54
0.2	0.8281		8.10261	5.36	4.526	15.56
0.3	1.2388		8.76753	5.40	4.821	10.72
0.4	1.6743		9.25644	5.43	5.131	5.51
0.5	2.0535		9.54624	5.54	5.402	2.49

Density Measurement

Density of ferrite samples played a crucial role in the determination of electrical as well as magnetic properties. The bulk density (ρ_B) was measured by usual mass and volume ratio while X-ray density (ρ_x) was calculated from the exact value of the lattice parameter and the molecular weight of the investigated sample. The variation of the X-ray and bulk densities of $Co_{1-x}Zn_xFe_2O_4$(x=0.0-0.5) ferrites with increasing Zinc content has been shown in Fig. 5.9. It is observed from Fig. 5.9 that the X-ray density increases with increasing Zinc content. The bulk density is also found to increase with Zinc inclusion in the lattice. The increase in X-ray and bulk density may be due to the increase in molecular weight of the various compositions of Co-Zn ferrites. Generally, the homogeneous distribution of any element in other element may increase the density. It is also observed from this Figure that the X-ray density is higher than the bulk density. This might be evolved with the existence of pores on the macroscopic scale and vacancies in the lattice on atomic scale during the sintering process [8]. The smaller value of bulk density, $\rho_B$compared to the X-ray density, ρ_x might be due to the presence of inter-granular porosity which is apparent in the SEM image observation.

Porosity measurement

The existence of porosity in the samples is highly influenced by the amount of applied pressure, sintering temperature and prolonged sintering time during the sample preparation.The porosity of the ferrite samples is a result of the combination of intra-granular porosity and the inter-granular porosity [9]. Thus the total porosity could be written as

$$P=P_{intra} + P_{inter} \qquad (5.1)$$

The inter-granular porosity mainly depends on the grain size [10]. It is observed from Fig. 5.10 that the porosity of all samples decreases with the increasing Zinc content. The decreasing trend of porosity with doping content is clearly opposite to the changing trend of bulk density which is indicated in Fig.5.11. This can be explained by the growth of grain boundary.

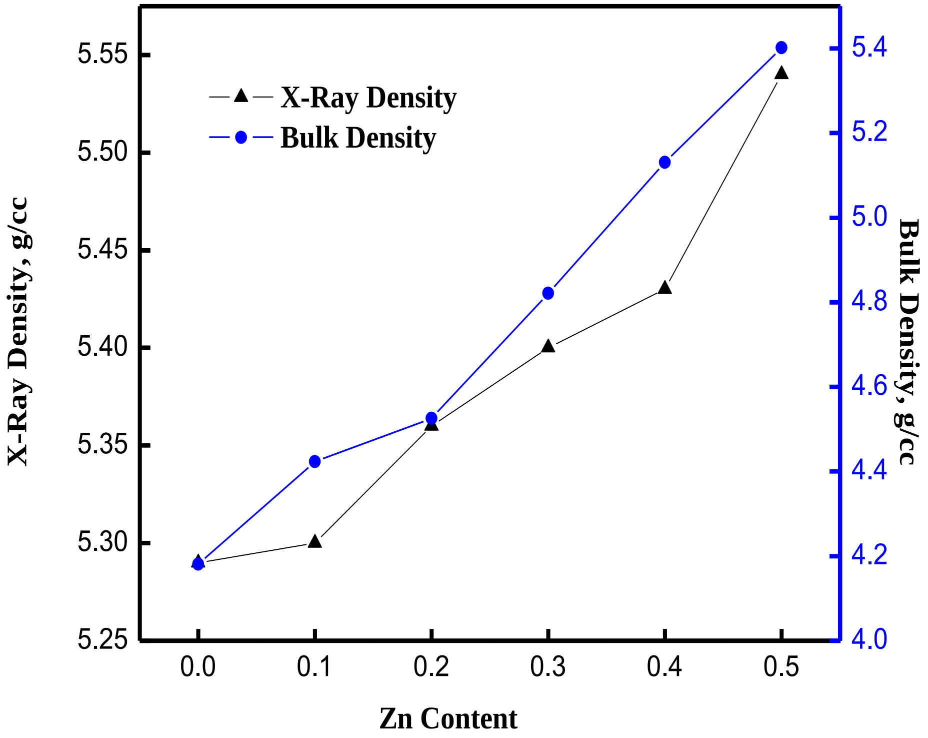

Figure 5.9: Variation of X-ray density and Bulk density as function of Zn Content.

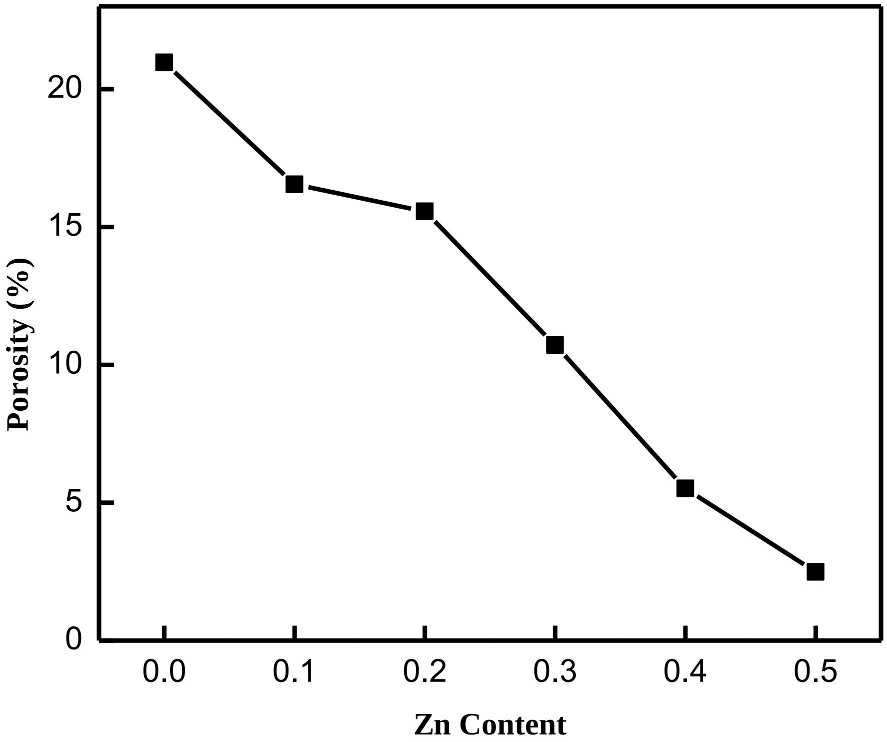

Figure 5.10: Variation of porosity of $Co_{1-x}Zn_xFe_2O_4$(x=0.0-0.5) ferrites as function of Zinc.content

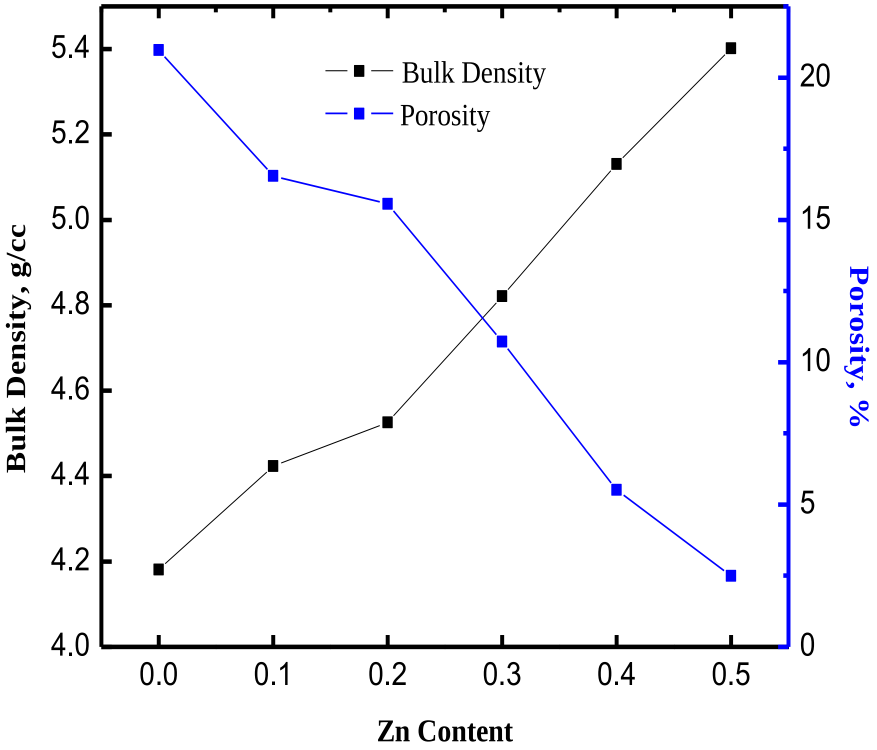

Figure 5.11: Variation of Bulk density and Porosity of $Co_{1-x}Zn_xFe_2O_4$(x=0.0-0.5) ferrites As function of Zn content

5.2 Microstructure study

It is well known that most of the electromagnetic characteristics of a ferrite material strongly depend on the microstructure of the fired body. The microstructures of the investigated materials are given in Fig.5.12, 5.13 and 5.14. It is observed that crystallization of the spinel phase has been aided by CoO. Also the role of ZnO in $CoFe_2O_4$ is to stabilize the microstructure i.e. hinders the grain growth during sintering.

The grain size of pure $CoFe_2O_4$ is almost independent of sintering temperature. The grain size remained almost same for the lower Zinc substitution (x = 0 to 0.3) in Cobalt ferrites. For higher Zn content (x = 0.4, 0.5), the grain size found to be decreased. This is due to the fact that the ions like Cd^{2+}, Zn^{2+}, Ti^{4+}, Nd^{2+} do not favor grain growth when present in excess quantities [10,11]. Thus $Co_{0.5}Zn_{0.5}Fe_2O_4$ has lowest grainsize.

For the samples with large grain, the majority of pores are trapped inside the grain at large distance from the grain boundary, which affects the value of permeability, resistivity and density [12]. It is observed from the Figures that within the grain there is some black spot which are the pores. These pores play an important role to determine the properties of the material. The values of permeability of Co-Zn ferrites decreases with decreasing grain size because domain wall motion influenced with changing grain size.

Resistivity of sample depends on the porosity. For the samples with large grains, the majority of pores are trapped inside the grains at large distance from the grain boundaries, which affects the value of permeability, resistivity and density [13].

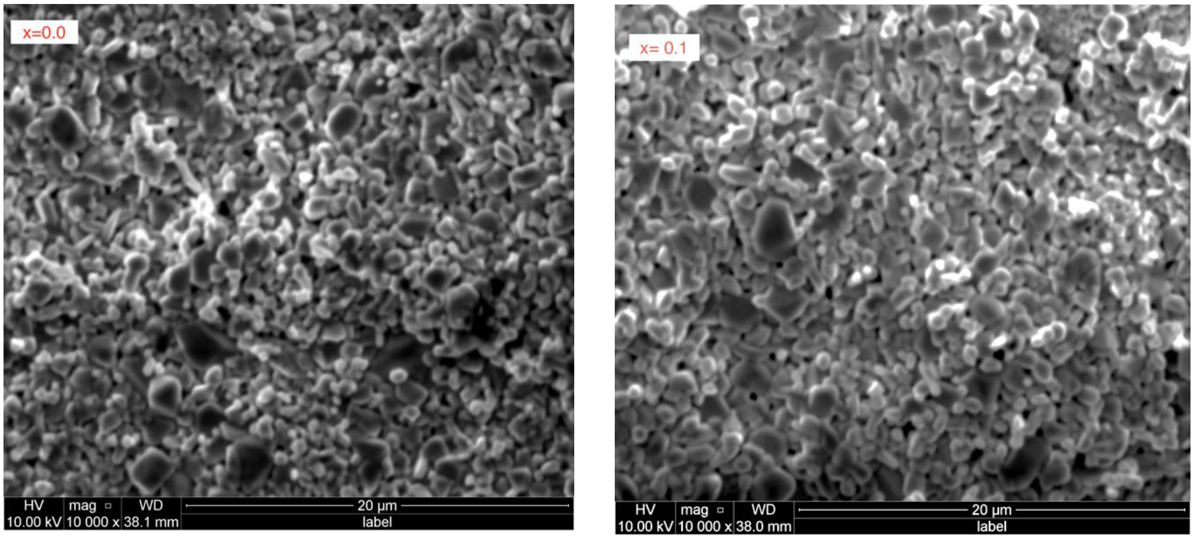

Figure 5.12: Scanning Electron Microscope (SEM) images for $Co_{1-x}Zn_xFe_2O_4$(x= 0,0.1) respectively.

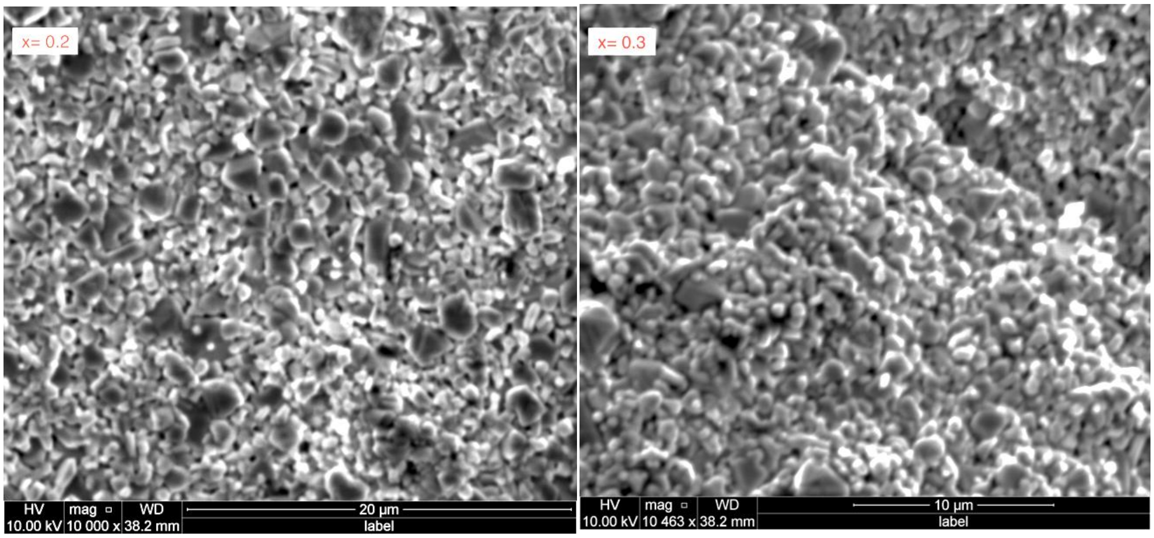

Figure 5.13: Scanning Electron Microscope (SEM) images for $Co_{1-x}Zn_xFe_2O_4$(x=0.2,0.3) respectively.

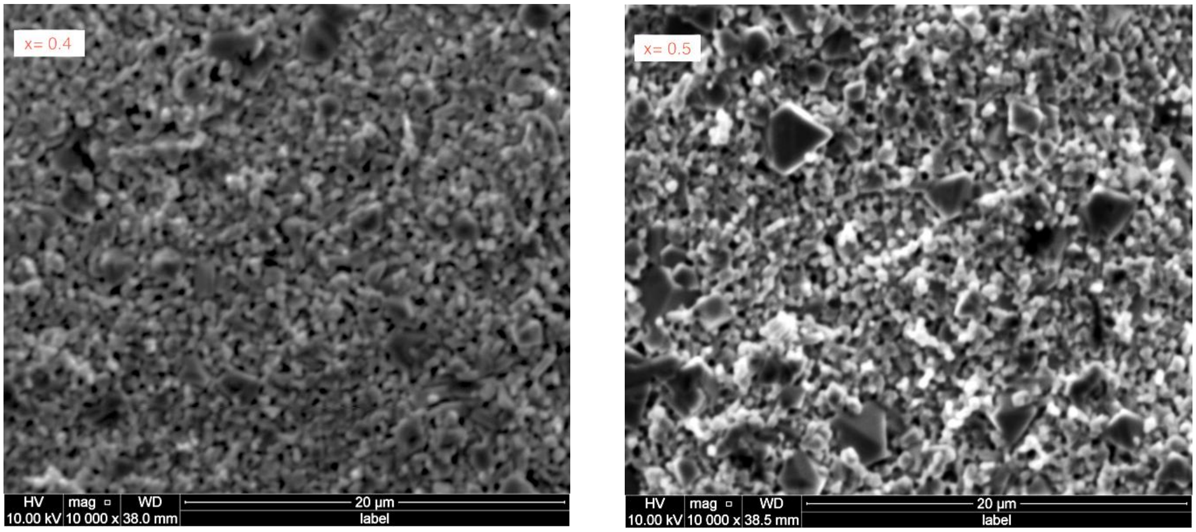

Figure 5.14: Scanning Electron Microscope (SEM) images for $Co_{1-x}Zn_xFe_2O_4$(x=0.4,0.5) respectively.

5.3 Frequency dependence of Dielectric Constant (ε')

The variation of the real (ε') and imaginary (ε'') part of dielectric constant with frequency from 10 KHz to 40 MHz at room temperature are shown in Fig. 5.15 and 5.16 respectively. The dielectric constant (ε') decreases with increasing frequency, which is rapid at lower frequencies and slower at higher frequencies. At much higher frequency it is very small and becomes independent of frequency. This is normal dielectric behavior observed in most of the ferromagnetic materials, which may be due to the interfacial polarization as predicted by Maxwell and Wagner [14].

The dielectric behavior of ferrites may be explained on the basis of dielectric polarization process, which is similar to that of the conduction mechanism that takes place mainly by the hopping of electrons. Electrical conduction in ferrites can be explained by Verway-de-Boer hopping mechanism [15]. Verway explained that the electronic conduction in ferrites is mainly due to hopping of electrons between ions of the same element existing in more than one valence state and distributed randomly over crystallographically equivalent lattice sites.

A number of such ions formed during the sintering of ferrites. Fe^{2+} ions concentration is a characteristic property of a ferrite material and depends upon several factors such as sintering temperature/ time and atmosphere including the grain structure. Creation of Fe^{2+} gives rise to electron hopping between Fe ions in +2 and +3 valance states. The electronic exchange between Fe^{2+} and Fe^{3+} results in local displacement of charges in the direction of applied electric field, which is responsible for the polarization of ferrites [16,17]. The magnitude of exchange depends on the concentration of Fe^{2+}/Fe^{3+} ion pairs present in B-site [5]. The dielectric constant decreases with increasing frequency and then reaches a constant value due to the fact that beyond a certain frequency of external AC field, the electron exchange between Fe^{2+} and Fe^{3+} cannot follow the alternating field. This type of dielectric behavior was observed in a number of ferrites such as Cu-Cd ferrites [18], Mg-Cu-Zn ferrites [19], Li-Co ferrites [20], Ni-Cu-Zn ferrites [21] and Li-Mg-Ti ferrites [22]. All the samples have high value of dielectric constant in the order of 10^3-10^5 at low frequencies. This high value at lower frequency region is due to the Maxwell-Wagner interfacial type of polarization [23, 24] for the inhomogeneous double layer dielectric structure, which is in agreement with Koop's Phenomenological theory [25].

The grain boundaries of low conductivity and high dielectric constant are found to be more effective at lower frequencies while the ferrite grains of high conductivity and lower dielectric constant are more effective at high frequencies [16, 24]. According to Koop's model, ferrite samples with inhomogeneous dielectric structure can be imagined as a system of high conductive grains (with ε_1, σ_1 and thickness d_1) separated by highly resistive thin grain boundaries (with ε_2

, σ_2 and thickness d_2). Koops assumed that $x=d_1/d_2$, $\sigma_2 << \sigma_1$ and $\varepsilon_1 \sim \varepsilon_2$ and the dielectric constant of the sample ε' is given by

$$\varepsilon' = \varepsilon_1 / x \sim \varepsilon_2 / x \quad (5.2)$$

Thus the grain boundary phase controls the behavior of ε' at lower frequencies. The thinner the grain boundary layers, the higher the values of ε'. The presence of Fe^{2+} ions in excess amount favors the polarization effects. Thus, the more dispersion observed in the samples can be attributed to the presence of Fe^{3+} ion in excess amount, which could be formed at elevated sintering temperature. Similarly, the weak dependence of dielectric constant on frequency can be due to lack of Fe^{2+}/ Fe^{3+} ions concentration. In the present Co-Zn ferrite, the following equilibrium may exist during sintering

$$Co^{2+} + Fe^{3+} \Leftrightarrow Co^{3+} + Fe^{2+}$$

The real dielectric constant is given by the following Debye equations [18] as:

$$\varepsilon' = \varepsilon_\infty + \frac{\varepsilon_0 - \varepsilon_\infty}{1 + \omega^2 \tau^2} \quad (5.3)$$

Where, τ is the relaxation time, ε_0 is the dielectric permittivity at very low frequency and ε_∞ is the dielectric permittivity at very high frequency. Equation (5.2) indicates the ε' decreases as the frequency increases. This is in agreement with the behavior of ε' for the present samples.

Figure 5.17 shows that dielectric constant increases for x = 0.1 after that it decreases with the increasing Zinc content. The dielectric constant is expected to decrease as the grain size is found to be decreased with Zinc content. The sample with x = 0.1 may content inhomogeneity of the raw material oxides during the preparation. Therefore, this sample shows comparatively high dielectric constant than the others.

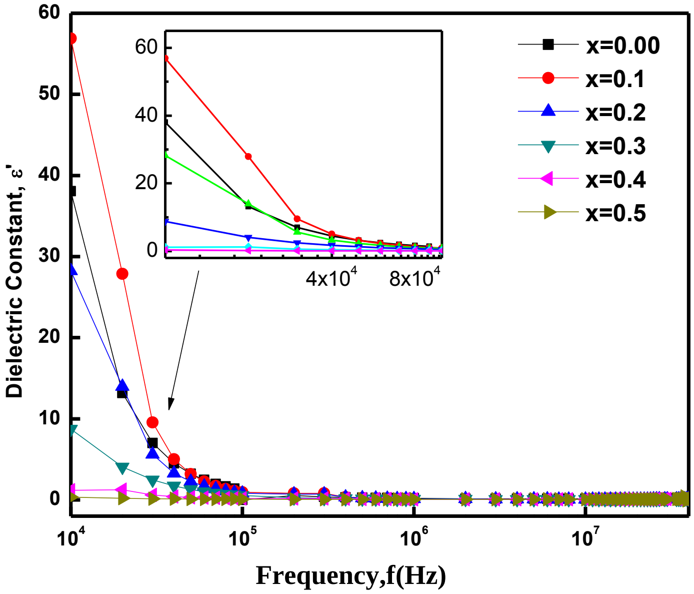

Figure 5.15: Variation of dielectric constant with increasing frequency of $Co_{1-x}Zn_xFe_2O_4$(x=0.0-0.5).

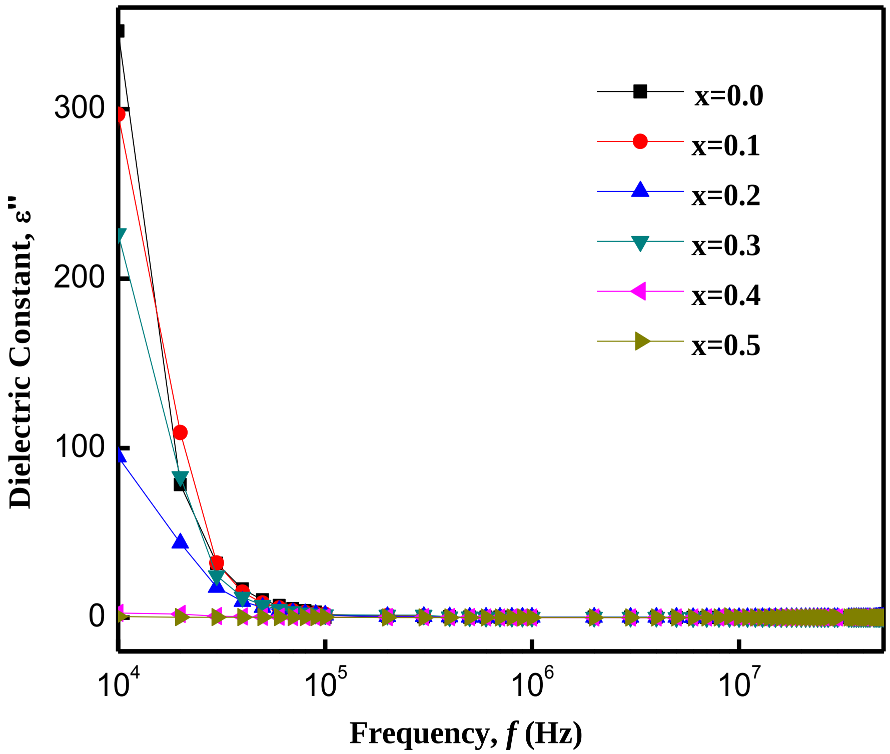

Figure 5.16: Variation of imaginary dielectric constant of $Co_{1x}Zn_xFe_2O_4$(x=0.0-0.5) with increasing frequency.

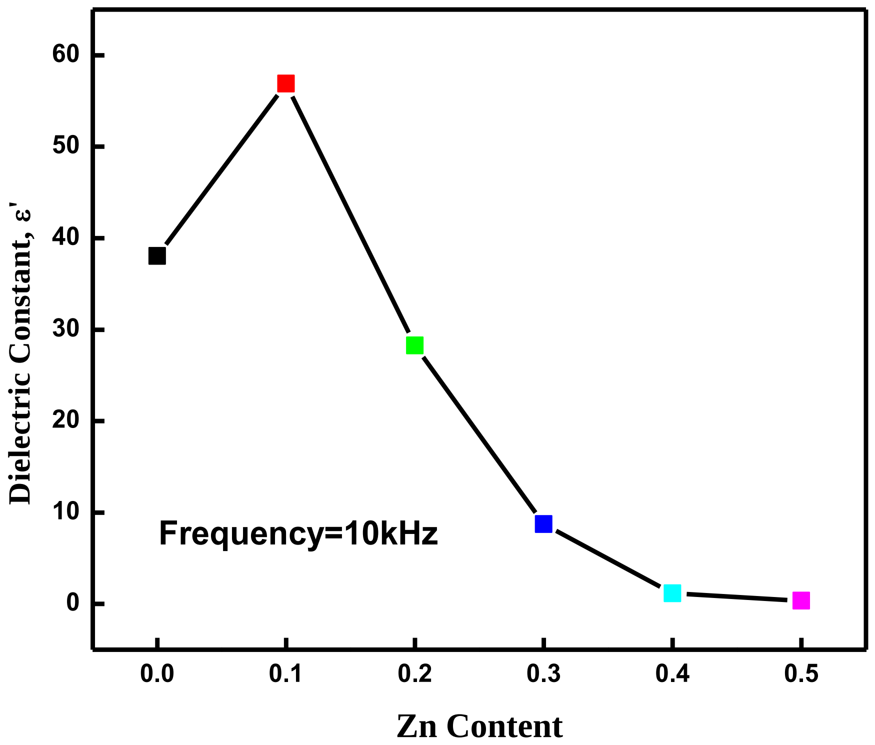

Figure 5.17: Variation of dielectric constant of $Co_{1-x}Zn_xFe_2O_4$(x=0.0-0.5) at frequency, *f*=10 kHz.

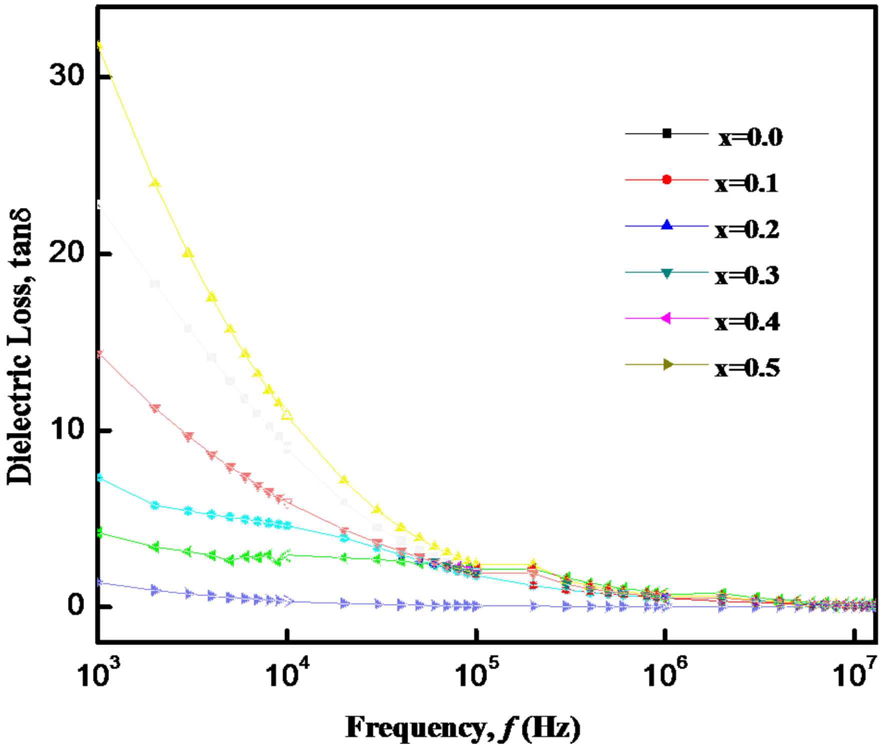

Figure 5.18: Dielectric loss of $Co_{1-x}Zn_xFe_2O_4$(x=0.0-0.5) as function of frequency.

Frequency dependence of dielectric loss

Figure 5.18 shows the variation of dielectric loss with frequency which is calculated from dielectric constant. Similar to dielectric constant, dielectric loss decreases rapidly with increasing frequency and becomes constant at higher frequency range. Dielectric loss arises when the polarization lags behind the applied field and is caused by grain boundaries, impurities and structural inhomogeneity [26]. The higher value of loss factor in the low frequency region may be due to the presence of high resistivity in the grain boundaries and more energy is required for exchange of electrons between Fe^{2+} and Fe^{3+}. On the other hand, in the high frequency that corresponds to low resistivity due to grain, small energy is required for electron exchange between Fe^{2+} and Fe^{3+} at the octahedral site results in lower value of dielectric loss [27]. From the Figure it is found that the value of dielectric loss decreases with increasing frequency. The obtained small loss in the high frequency range (10^6 Hz- 10^7 Hz) may be applicable to the high frequency microwave devices.

From Fig. 5.16, it is noticed that all the samples have high dielectric constant at low frequency range. The microstructure of the samples consists of well-conducting grains separated by poorly conducting grain boundaries. As the grain boundaries have large resistance that results in the large values of ε' and ε'' in low frequency range.

Frequency dependence of Q factor (QF)

Quality factor was calculated using equation, $Q = \frac{1}{\tan\delta}$. According to the equation it is clear that quality factor is inversely related to the dielectric loss. Figure 5.19 exhibits the variation of Q factor with the increasing frequency for the composition of $Co_{1-x}Zn_xFe_2O_4$(x=0.0-0.5) ferrite. It is noticed that Q factor is minimum at the low frequency region but it has started to increase from 1 MHz to nearly 5 MHz. The increase in quality factor, Q might be due to the increase of hopping mechanism.

Frequency dependence of Relative Quality Factor (RQF)

Figure 5.20 shows the variation of relative quality factor (RQF) of $Co_{1-x}Zn_xFe_2O_4$(x=0.0-0.5)ferrite with frequency. It is observed that the RQF has minimum value in the low to mid frequency region for sample $Co_{0.5}Zn_{0.5}Fe_2O_4$. Then the RQF started to increase at 1 MHz and has a peak value at 300MHz. The increase in RQF is inverse to the decrease of dielectric loss. It is also observed that the polarization is lower in mid frequency range for all the samples but it is found to be higher in low frequency range (except for x=0.5) and in high frequency range.

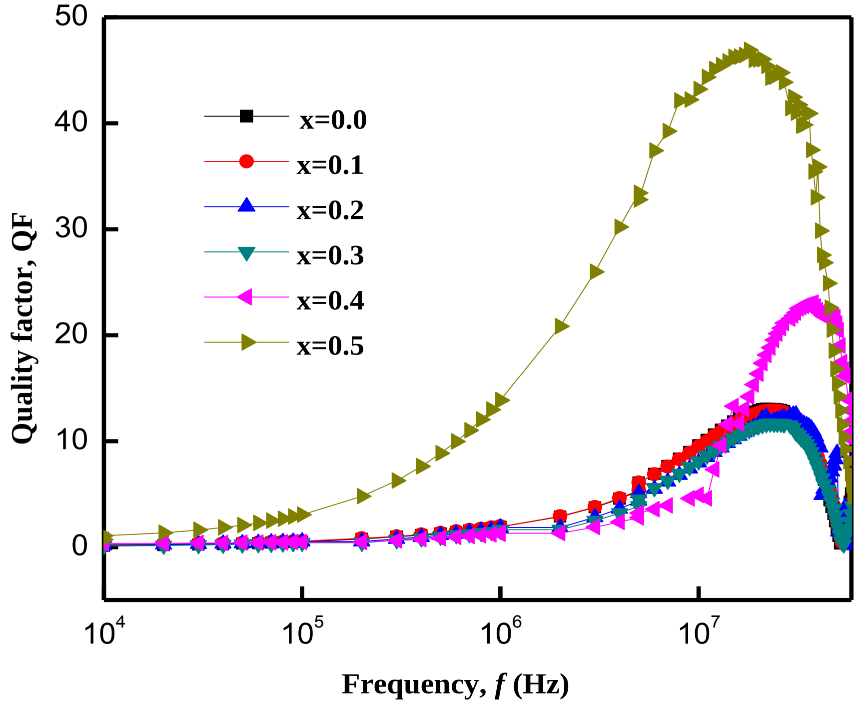

Figure 5.19: Variation of quality factor, QF of $Co_{1-x}Zn_xFe_2O_4$(x=0.0-0.5) with increasing frequency.

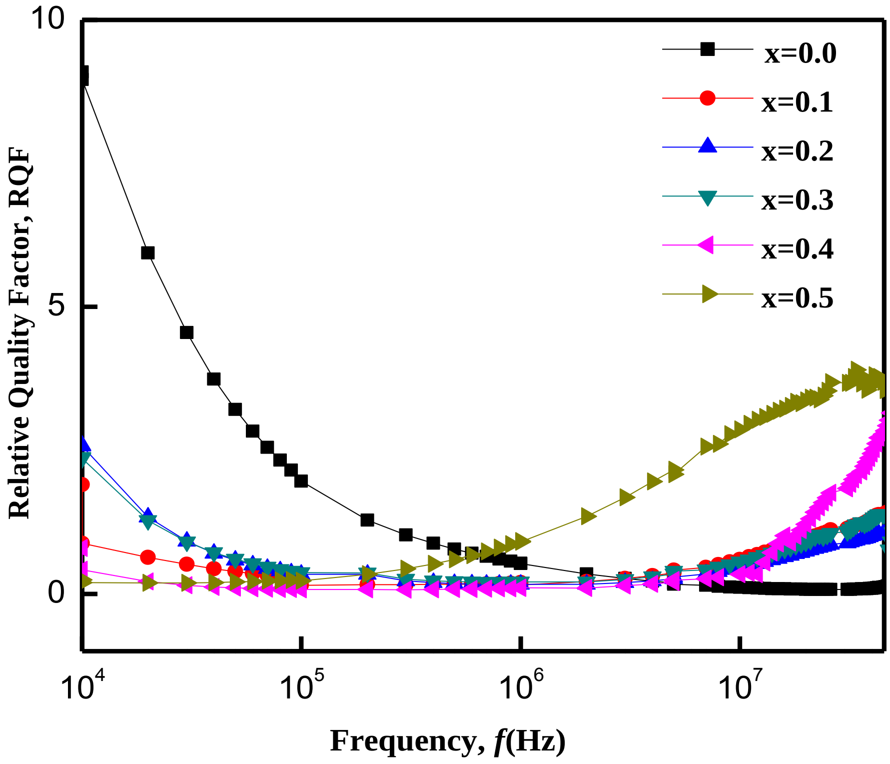

Figure 5.20: Variation of relative quality factor, RQF of $Co_{1-x}Zn_xFe_2O_4$(x=0.0-0.5) with increasing frequency.

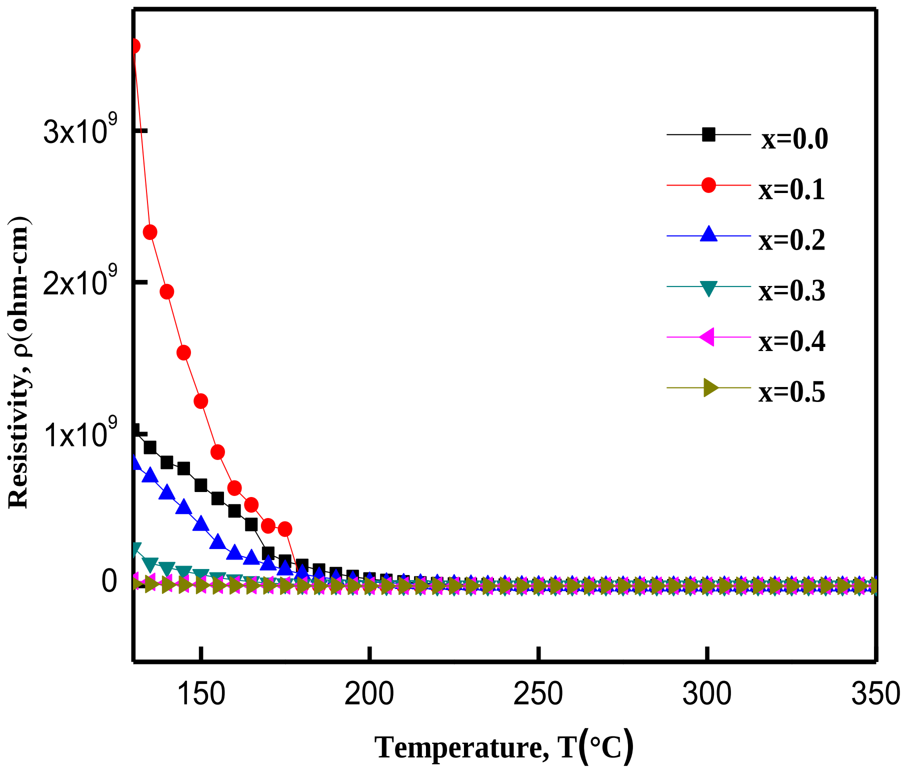

Figure 5.21: Variation of resistivity of $Co_{1-x}Zn_xFe_2O_4$(x=0.0-0.5)as a function of temperature.

5.4 Temperature Dependence of Resistivity

The temperature dependence of DC electrical resistivity of ferrites is crucial because of its huge applications with temperature characteristics. Resistivity is an intrinsic property of any material. The resistivity of $Co_{1-x}Zn_xFe_2O_4$(x=0.0-0.5) was calculated and plotted against temperature in Figure 5.21. From Figure it is seen that the DC resistivity decreases with increase in temperature which is the normal ferromagnetic behavior. The resistivity of the ferrites is expected to decrease with an increase in the temperature; this may be due to the low dielectric constant and also depends on the porosity and composition [28]. And also it is observed that the dispersion is more at low-temperature side which could be due to the difference in the concentration of Fe^{3+}/Fe^{2+} and other ions in the different samples [29]. The conduction mechanism in the ferrites can be explained on the basis of hopping of charge carriers between Fe^{3+} and Fe^{2+} ions on octahedral sites [30, 31]. The increase in temperature of the applied field enhances the hopping of charge carriers resulting in an increase in the conduction process thereby decreasing the resistivity. At high temperature, DC resistivitybecomes negligibly small and remains constant because the hopping frequency no longer exists.

It is observed that for x=0.1, the dielectric constant as well as the resistivity was higher than that of the pure Cobalt Ferrite. This sample may have higher dielectric properties and low eddy current loss than the other samples.

5.5 Magnetization measurement:

Magnetization measurements for the ferrite system $Co_{1-x}Zn_xFe_2O_4$(x=0.0-0.5) were carried out using the vibrating sample magnetometer (VSM) at room temperature as a function of field to reach saturation values and the results are plotted as in Fig. 5.22. The magnetization of all the samples is saturated. From Fig. 5.23 it is observed that the saturation magnetization decreases with Zn content. The saturation magnetization value of a sample has been taken the magnetization at high field where magnetization is independent of magnetic field.

Magnetization in ferrite samples originate due to the difference in the magnetic moments for the two sub-lattices. The larger the difference, the greater is the resultant magnetization, because of the anti-parallel arrangements of the moments in two sub-lattices. The magnetic moment of each sub-lattice arises due to the presence of magnetic ion such as Fe^{2+}, Fe^{3+}, Mn^{2+}, Cu^{2+}, Ni^{2+} etc. In our case, Co^{2+} and Fe^{3+} have magnetic moment while Zn^{2+} is non-magnetic. Different ions occupy different lattice sites i.e. tetrahedral (A-site) and octahedral (B-site) [5]. So as a whole, the two sub-lattices have their individual resultant magnetic moment which in turn yields magnetization. Now the site preference of the magnetic ions is rather complex since it is governed by many competing factors. The principle dominating factors are ionic radius, electronic configuration and the electrostatic energy.

The magnetic ordering in the simple spinel ferrites is based on the Neel's two sub-lattice (Tetrahedral A-site and octahedral B-site) model of ferrimagnetism in which the resultant magnetization is the difference between B-site and A-site magnetization, provided that they are co-linear and anti-parallel to each other [32]. The A-B exchange interaction is known to be the strongest and dominates over the B-B and A-A interactions. Hence the net magnetization is given by

$$M = M_B - M_A \tag{5.4}$$

Where M_B and M_A are the octahedral and tetrahedral sub-lattice magnetization respectively. The composition dependence of magnetization can be explained on the basis of cation distribution. In Co-Zn ions preferentially occupy the B-sites only and Zn^{2+} at A-sites. The cation distribution can be represented as

$$(Zn_X^{2+}Fe_{1-x}^{3+})_A[Co_{1-x}^{2+}Fe_{1+x}^{3+}]_B$$

Where the first and square brackets indicate the tetrahedral (A-site) and octahedral (B-site) sub-lattice respectively. The ionic magnetic moment of Zn^{2+} is zero (non-magnetic) while the ionic magnetic moment of Co^{2+} is $1\mu_B$ and the ionic magnetic moment of Fe^{3+} is $5\mu_B$. Therefore, the saturation magnetization decreases due to the non-magnetic nature of Zn. With the addition of Zn^{2+} concentration, the Fe^{3+} ions in the lattice loss their magnetic neighborhood and hence, the spin may become uncoupled [33] and more fields are required to saturate i.e. to align the magnetic moments in the direction of applied magnetic field.

From Fig. 5.23, it is observed that magnetization decreases with Zn content. The decrease of magnetization is due to the dilution of magnetic moment of A sub-lattice by substitution of non-magnetic Zn ions. Since the resultant magnetization is the difference between the B and A sub-lattice magnetization, it is obvious that decrease of net magnetization is expected on dilution of the A sub-lattice magnetization due to occupation of A-site by non-magnetic Zn content as well as decrease of B sub-lattice magnetization due to the introduction of Fe^{3+} ions having $5\mu_B$ migrated from A-site to B-site due to the occupation of Zn ion on the A-site [32,33].

The experimental magnetic moment in Bohr magneton has been calculated from the measured saturation magnetization value per unit mass using the formula.

$$n_B = \frac{MM_S}{N\mu_B} \tag{5.5}$$

Where M_S is the saturation magnetization, M is the molecular weight, n_B is the magnetic moment in Bohr magneton μ_B, N indicates the Avogadro's number. When the Zn content on A-site is higher, the Fe^{3+} ions on the A-sites are no longer be able to align all the moments of the B-site ions anti-parallel to them since this is opposed by the negative B-B exchange interaction, which remains unaffected. The magnetization of the B sub-lattices makes an angle (called Y-K angle) with each other differing from 0˚ or 180˚ [34].

Here, from the Fig. 5.22 and Fig. 5.23, it is observed that in cobalt ferrites, the coercivity increased with the degree of zinc substitution (x=0.0-0.3) and then again decreased with Zn content (x=0.4,0.5). The low coercive field confirms the cobalt-zinc ferrite as a soft ferrite. So, the graph shows that the ferrite nature changed to softer to harder and then again harder to softer magnet. The difference in the H_c values is expectable because the Zn substantially increases inside the grain in response to the increase of unit cell volume [35].

Anisotropy constant has been calculated by using the formula, K= $\frac{H_c M_s}{2}$.Anisotropy constant increased with increasing Zn content up-to x = 0.0-0.3 and then decreased at x = 0.4, 0.5 for the composites $Co_{1-x}Zn_xFe_2O_4$(x=0.0-0.5). Anisotropy represents the energy required to deflect the domains from the "easy" to "hard" positions. The easy and hard alignments and their relative energies depend on the interaction between spin magnetic moment of each atom of the compound being studied.

The change in anisotropy constant is similar to the change in coercive field. It is observed from the change of anisotropy constant with increasing Zn contents that Cobalt Ferrite behaved as “hard” magnet at the lower concentration of Zn (x=0.1,0.2). At x = 0.3-0.5, the Ferrite showed the characteristics of “soft” magnet.

As magnetization is easy to change for low anisotropy materials having small coercive field, such materials can be used as “soft” ferromagnets to make magnetic cores for transformers and inductors.

Also, the lower Zn substitution causes the anisotropy constant to be increased much higher (x = 0.1,0.2) than the higher Zn substitution (x = 0.3,0.4,0.5). It showed that x = 0.1,0.2 enhanced the storage capability of Cobalt ferrite. The results of magnetic characterization are summarized in Table-2.

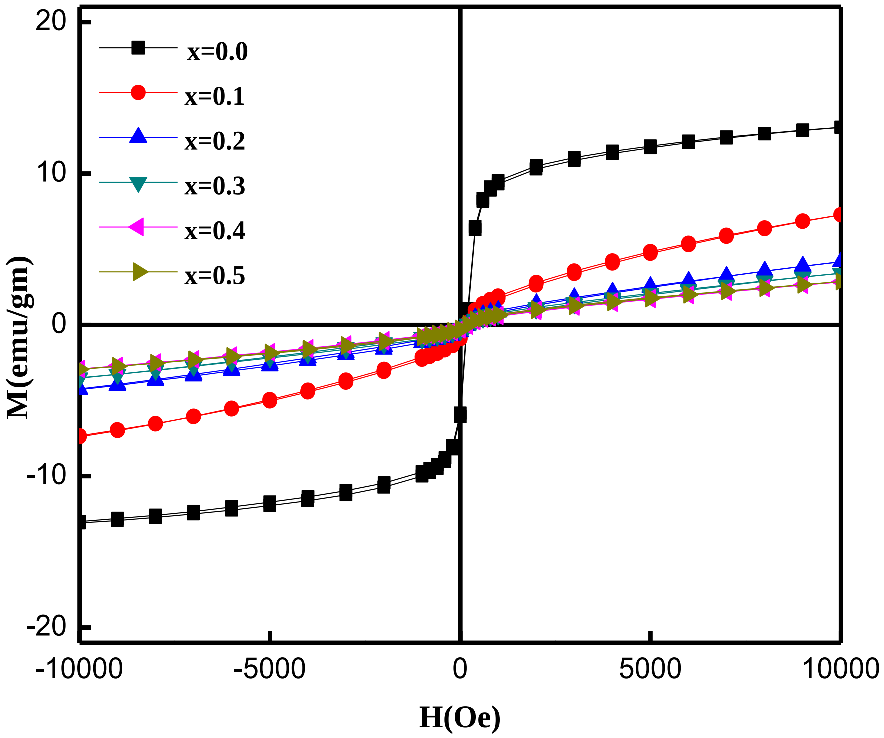

Figure 5.22: Hysteresis Loop of $Co_{1-x}Zn_xFe_2O_4$(x=0.0-0.5).

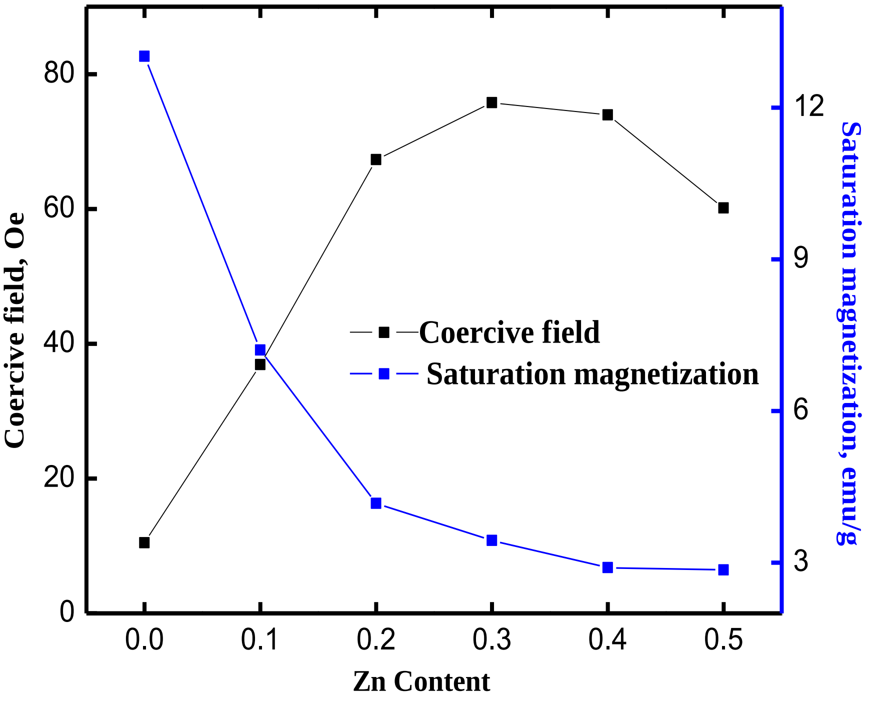

Figure 5.23: Variation of coercive field and saturation magnetization of $Co_{1-x}Zn_xFe_2O_4$(x=0.0-0.5) as function of Zinc content.

Table-2: Coercive field, Saturation magnetization and Anisotropy Constant for the samples with the composition $Co_{1-x}Zn_xFe_2O_4$(x=0.0-0.5).

Samples	Coercive field (Oe)	Saturation magnetization (emu/g)	Anisotropy Constant K emu/cm^3
$Co_{1-x}Zn_xFe_2O_4$(x=0.0)	10.4865	13.015	68.241
$Co_{1-x}Zn_xFe_2O_4$(x=0.1)	36.8806	7.2054	132.869
$Co_{1-x}Zn_xFe_2O_4$(x=0.2)	67.3183	4.1778	140.621
$Co_{1-x}Zn_xFe_2O_4$(x=0.3)	75.7387	3.4404	130.286
$Co_{1-x}Zn_xFe_2O_4$(x=0.4)	73.9391	2.9035	107.341
$Co_{1-x}Zn_xFe_2O_4$(x=0.5)	60.1089	2.8575	85.881

5.6 Permeability measurement:

Permeability is the measure of the ability of a material to support the formation of a magnetic field within itself. The frequency dependence of complex permeability is an important property that represents the dynamic magnetic properties of magnetic materials. Therefore, the optimization of the dynamic properties such as complex permeability in the high frequency range requires a precise knowledge of involving magnetization mechanisms. The complex permeability can be expressed as, $\mu = \mu' - i\mu''$ where, the real part of permeability μ' describes the stored energy expressing the component of magnetic induction B in phase and the imaginary part of permeability μ'' describes the dissipation of energy expressing the component of B 90^o out of phase with the alternating magnetic field H. The phase lag between the applied field and the response of the magnetic domains determine the real and the imaginary part of the complex permeability. The real part of complex permeability of ferrite materials are strongly modified by the change in the domain structure that depends on grain size, porosity and sintering temperature [36].

Frequency dependence of real and imaginary part of complex permeability

The complex permeability measurements on toroid shape specimens have been carried out at room temperature for all the samples of series $Co_{1-x}Zn_xFe_2O_4$(x=0.0-0.5) in the frequency range 1 kHz-100 MHz. The variation of μ' with frequency is shown in Fig. 5.24. It is found that the value of initial permeability (μ') remains constant up to a certain frequency (> 10^7 Hz) indicating good low frequency stability and then it falls rapidly to a very small value after a certain high frequency named as Cut-off frequency. The SEM images confirm that grain size decreases with the increasing Zn content. The decrease in grain size possibly have resulted in the reduction of the domain wall from each grain. As nonmagnetic impurities between intra-granular pores dominate over spin rotation and domain wall motion at high frequencies, permeability decreases at higher frequencies. Also, there is a decrease of imaginary part of permeability. This behavior refers a typical relaxation character which might be due to the reversible displacement of domain walls [30].

From Fig. 5.25, it is clearly visible that permeability decreases with the increasing Zn content. It is well known that the permeability of polycrystalline ferrite is related to two different magnetizing mechanisms: spin rotation and domain wall motion [37, 38]. According to the Globus- Duplex model [39], the permeability caused by wall motion is linearly influenced by the grain size, whereas the permeability for spin rotation is independent of grain size. The microstructure analysis of this work indicates the lowering of grain sizes with changing Zinc concentration of $Co_{1-x}Zn_xFe_2O_4$(x=0.0-0.5). Therefore, the decrease in domain wall movement results with the decrease of permeability [40, 41]. On another node, the dependence of permeability on molecular magnetism is such that the force on a domain wall due to a magnetic field and the resultant change of magnetization are both proportional to permeability [42]. The measured magnetization listed above is found to decrease with Zn content. This decrease of magnetization may influence the decrease of permeability. The results are in good agreement with each other.

Variation of imaginary permeability (loss component) with frequency is shown in the Fig. 5.26-5.28. The imaginary part decreases with the increase of frequency. In the high frequency region, the imaginary part of the complex permeability remains almost constant due to the saturation of the polarization.

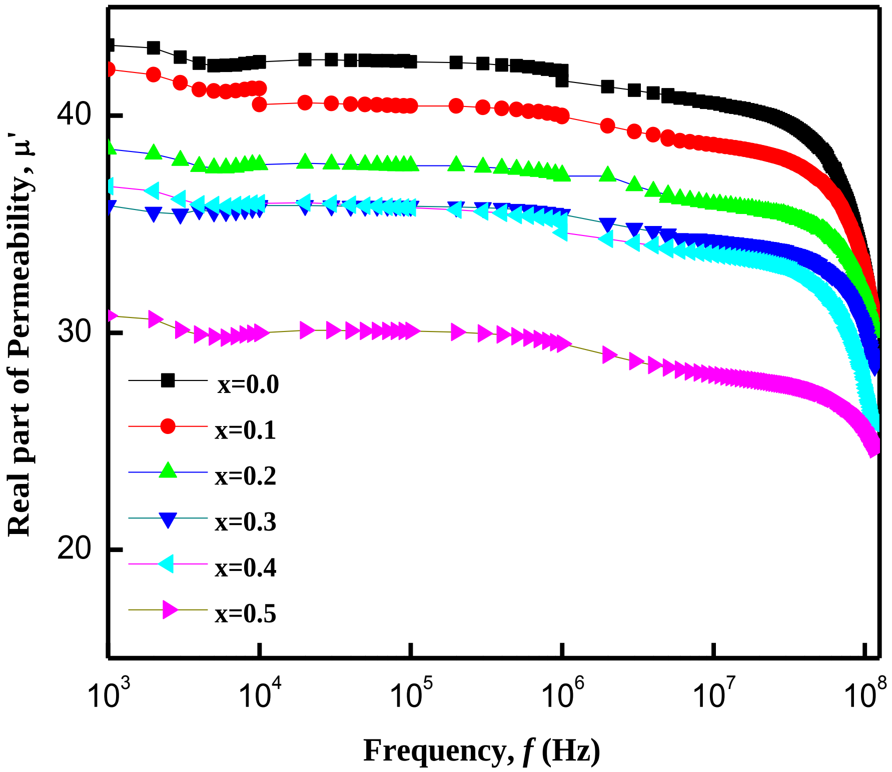

Figure 5.24: Variation of Permeability with increasing frequency of $Co_{1-x}Zn_xFe_2O_4$(x=0.0-0.5).

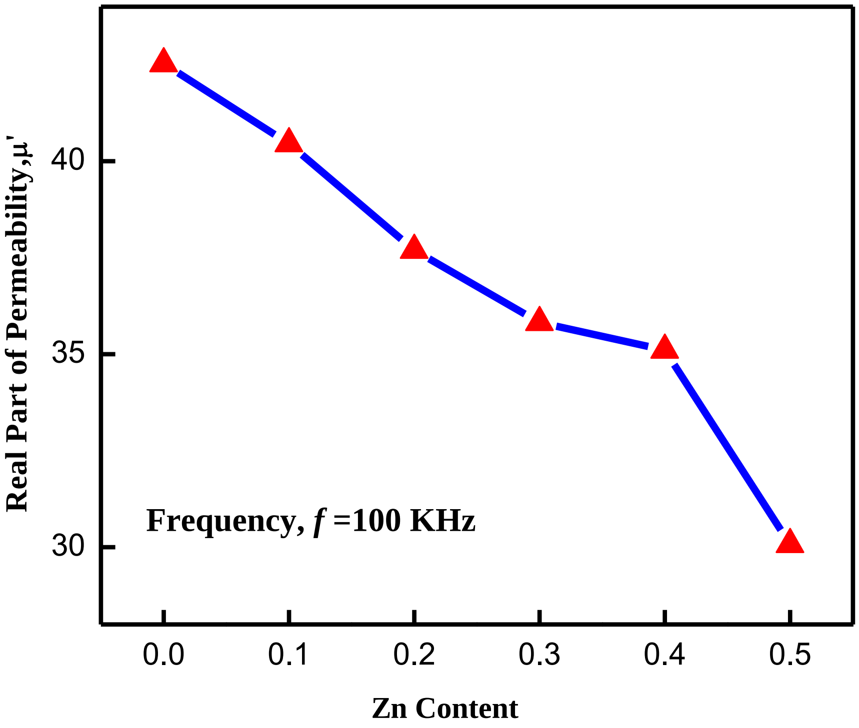

Figure 5.25: Variation of permeability at *f* = 100KHz with increasing Zinc concentration.

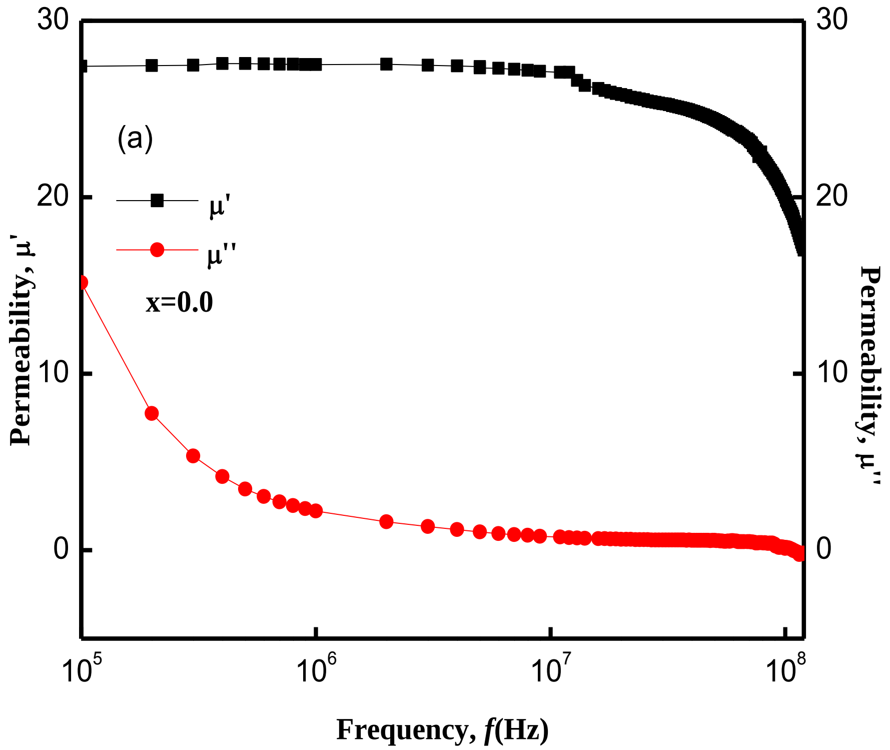

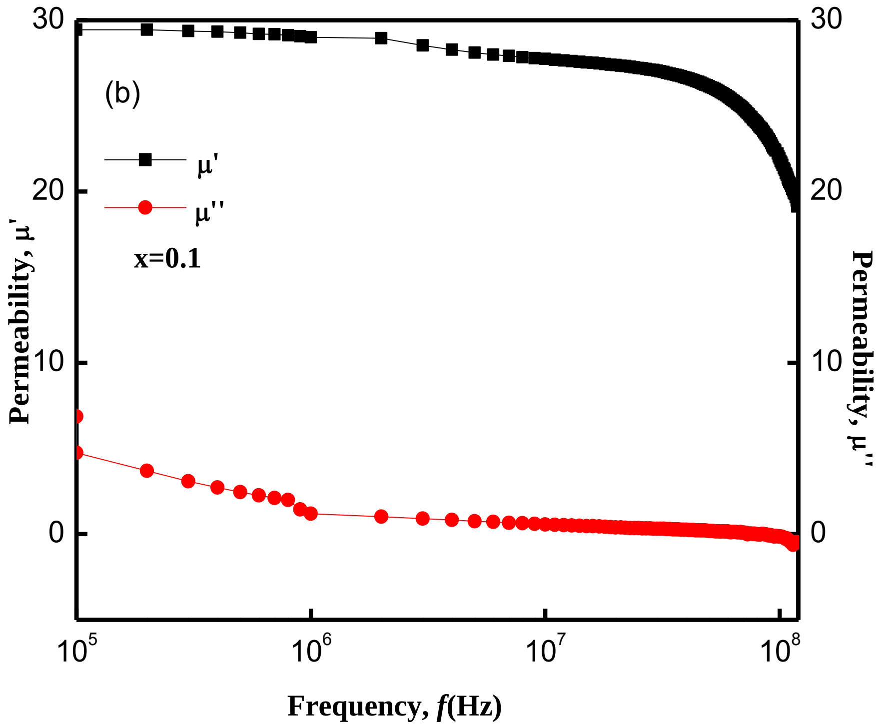

Figure 5.26: Variation of real and imaginary Part of Permeability of (a) x=0.0 and (b)x=0.1 of $Co_{1-x}Zn_xFe_2O_4$ ferrites as function of frequency.

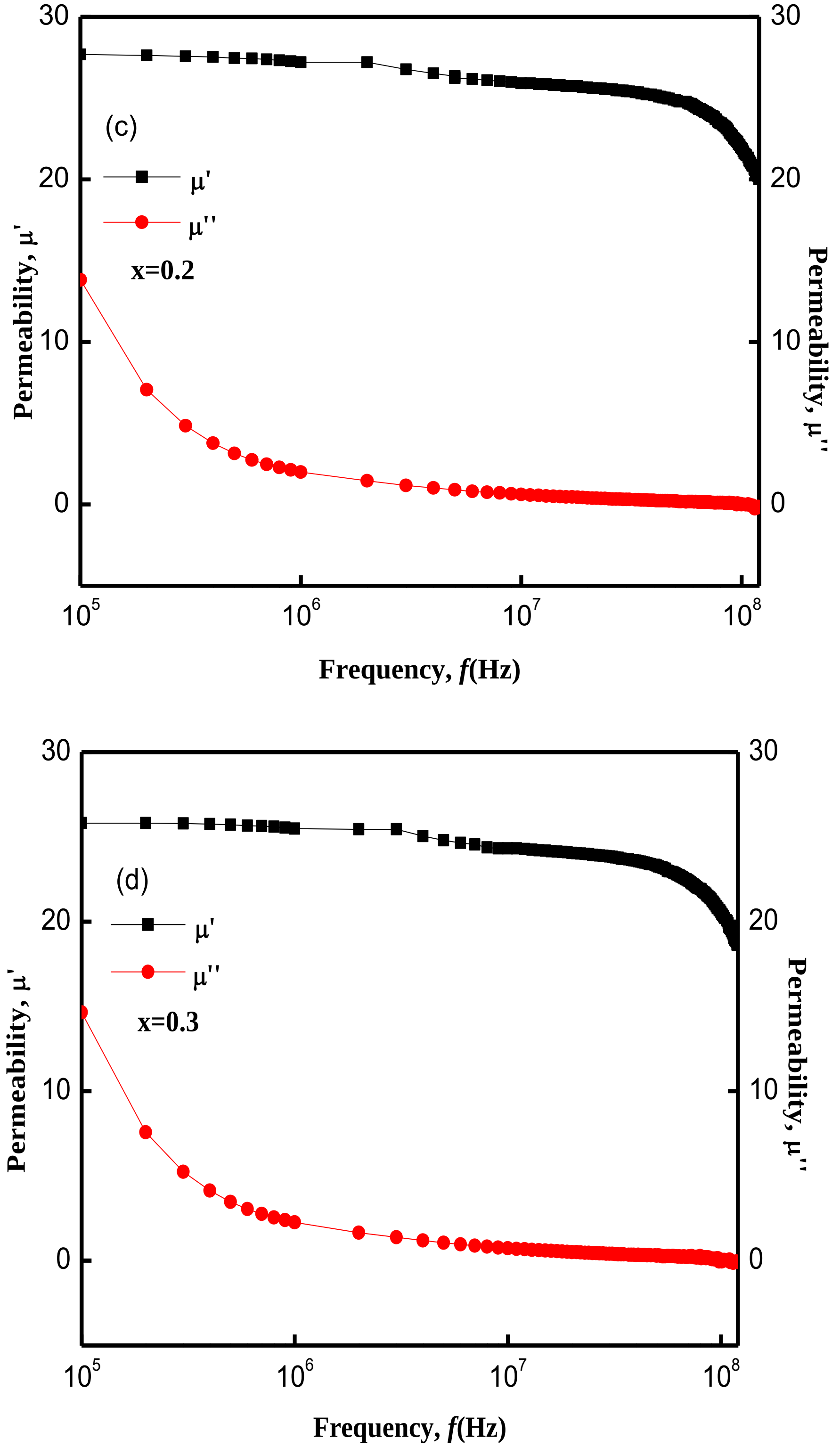

Figure 5.27: Variation of real and imaginary part of Permeability (c) x=0.2 and (d)x=0.3 of $Co_{1-x}Zn_xFe_2O_4$ ferrites as function of frequency.

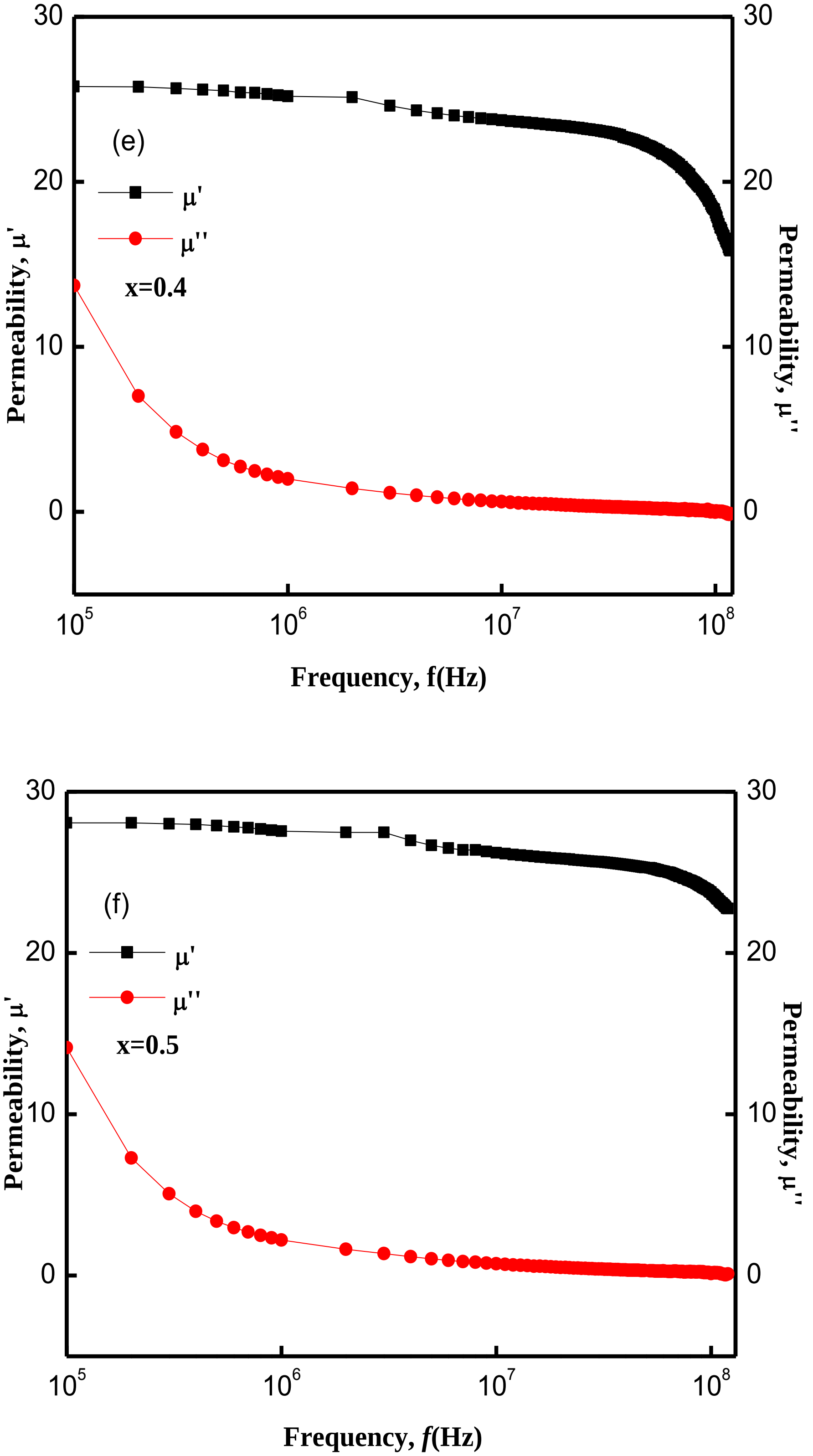

Figure 5.28: Variation of real and imaginary Part of Permeability (e) x=0.4 and (f)x=0.5 of $Co_{1-x}Zn_xFe_2O_4$ ferrites as function of frequency.

Frequency dependence of Q factor (QF) and Relative Quality Factor (RQF)

Figure 5.29 and Fig. 5.30 show the variation of Q factor & relative Q factor (RQF) with frequency of $Co_{1-x}Zn_xFe_2O_4$(x=0.0-0.5) that determines the efficiency of the magnetic materials. The variation of the quality factor and relative quality factor with frequency show a similar trend for all the samples. Q factor & relative Q factor increase with the increase in frequencies. Increase of Q-factor happens due to the low value of magnetic loss and low porosity. The Quality factor study is an important property to identify the perfect frequency band at which the sample works as soft magnetic material with low loss. Among the samples, Co-Zn ferrite with x = 0.1 has the highest QF and RQF. It means this sample has the lowest magnetic loss.

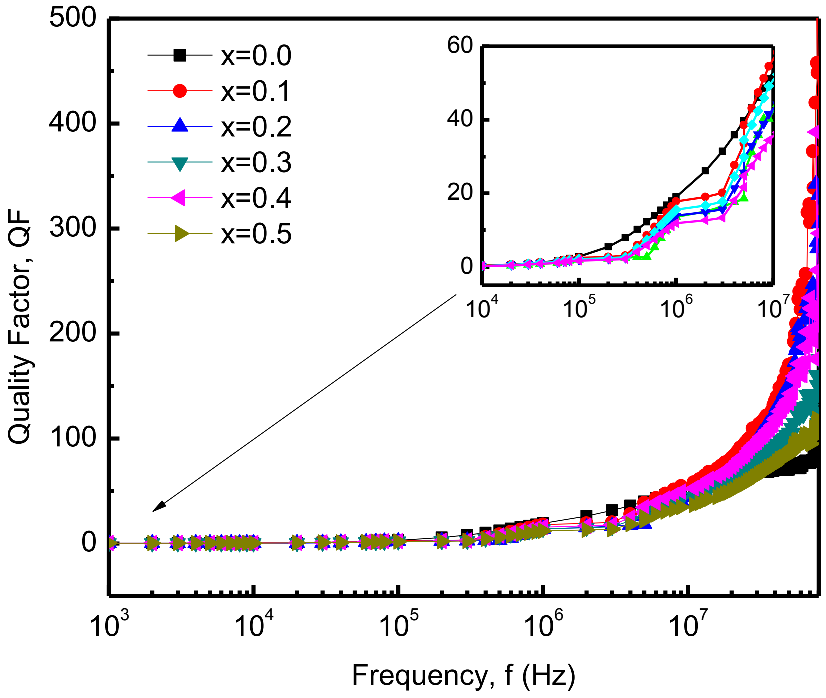

Figure 5.29: Variation of quality factor, QF of $Co_{1-x}Zn_xFe_2O_4$(x=0.0-0.5) with increasing frequency.

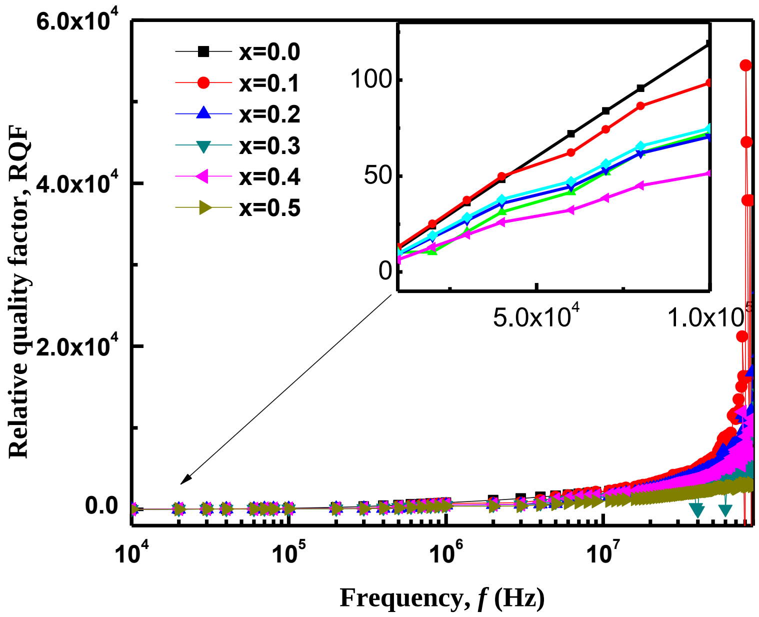

Figure 5.30: Variation of Relative quality factor, RQF of $Co_{1-x}Zn_xFe_2O_4$(x=0.0-0.5) with increasing frequency.

References:

[1] A.S.F. Al-Saaey, A.E.F.M. Khourshid, A.A. El-Hammady and A.RA. Badawi, IOSR-JAC, 7 (2014) 30.

[2] J.M.Garza, B.Wang, A.Madeira, C.D.Giorgio and G.Bossis , *J. Biomat. Nanobiotech.* 4 (2013) 222.

[3] M.A. Ameer and M. El-Hiti, J. Magn. magn. Matter., 234(2001) 118.

[4] A. Khan, M.A. Bhuiyan, G.D. Al-Quaderi, K.H. Maria, S. Choudhury, K.A. Hossain, S. Akther and D.K. Saha, J. Bang. Aca. Sci, 37(2013) 73.

[5] J. Smit, H.P.J. Wign, Ferrites, John Willy & Sons, Pub. Co. New York, (1959) 143.

[6] L. Vegard, Phys. Astro. 5 (1921) 17.

[7] G. Vaidyanathan, S. Sendhilnathan and R. Arulmurugan. J. Mag. Mag. Mater. 313(2007) 293.

[8] A.A Sattar, A.H. Wafik and H.M. El-Sayed, Phys. Status. Solidi (a) 186(3) (2001) 415.

[9] A.A. Sattar, H.M. El-Sayed, K.M. El-Shokrofy and M.M. El-Tabey, J.Appl.Sci. 5(1) (2005) 162.

[10] S.E. Jacobo, P.G. Bercoff, Ceram. Inter., 42(6) (2016) 7664.

[11] T. Mariam and S. Choudhury, J. Bangladesh Acad. of Sci. 41(2017)85.

[12] S.S. Bellad, S.C. Watawe, A.M. Shaikh and B.K. Chougule, Bull. Mater. Sci. 23(2000) 83.

[13] A. Gonchar, V. Andrev, L. Letyuk and A. Shishkanov, J. Magn. Magn. Mater. 544 (2003) 254.

[14] L. Néel, In Annales de Physique, 3 (1948) 137.

[15] L.I. Rabkin, Z.I. Novikova, Ferrites(Minsk), USSR (1960) 146.

[16] K. Iwachi, Jpn. J.Appl. Phys. 10(1971) 1520.

[17] C.B. Kolekar, P.N. Kamble and S.G. Kulkarni, J. Mat. Sci. 30 (1995) 5784.

[18] N. Gupta, S. Kashyap and D.C. Dube, Phys. Stat. Solidi(a) 204 (2007) 2441.

[19] A. Baskar, B. Rajinikanth and S. Murthy, J. Magn. Magn.Mat. 283(2004)109.

[20] Z. Yue, Z. Ji, Z. Gui and L. Li, J. Magn. Magn.Mat. 264(2003) 258.

[21] S.S. Bellad and B.K. Choughule, J.Mater.Chem.Phys.66(2000) 58.

[22] J. Maxwell, "A Treatise on Electricity and Magnetism" Clarendon Press, Oxford, London, (1982).

[23] B. Kumar and G. Srivastava, J. Appl.Phys.70(1994)6115.

[24] C.G. Koops, Phys. Rev.8391(1951)121.

[25] J. J. Thomas, A. B. Shinde, P. S. R. Krishna and N. Kalarikkal, J. All. Comp. 546 (2013) 77.

[26] R. Lebourgeois, J.P. Ganne and B. Llot, J. Phys. IV France 7 Suppl. CI: (1997)105.

[27] J. J., Shrotri, S. D. Kulkarni, C. E. Deshpande, A. Mitra, S. R. Sainkar, P. S. Anil Kumar and S. K. Date, Mat. Chem. Phy., 59 (1999) 1.

[28] A. Globus, J. Phys. Collaques, 38 (1977) C1-1.

[29] Y. Bai, J. Shou, Z. Gui, Z. Yue and L. Li, J. Magn. Magn. Mater., 264 (2003) 44.

[30] F.G. Brockman, P.H. Dowliay and W.G. Stenneck, Phys. Rev. 77 (1950) 85.

[31] K. Overshott, IEEE Trans. Magn. 17 (1981) 2698.

[32] T.T. Srinivasan, R. Ravandranathan, L.E. Cross, R. Newham, S.G. Sanker and K.C. Patil, J. Appl. Phys,63(8) (1988)3789.

[33] K.H. Maria, S. Choudhury and M.A. Hakim, International Nano Letters, 42(3) (2013) 1.

[34] S. S. Jadhav, S.E. Shirsath, S.M. Patange, and K.M. Jadhav**,** J.Appl.Phys, 108 (2010) 093920.

[35] B.R. Karche, B.V. Khasbardar and A.S. Vaingankar, J. Magn. Magn. Mat.168 (1997) 292.

[36] A.Hassadee,T.Jutarosaga andW.Onreabroy, Pro.Eng. 32(2012) 597.

[37] A. Globus, R.V. Monjaras, IEEE Trans. Magn. 11(5) (1975) 1300.

[38] K.K. Bharathi, G. Markandeyulu and C.V. Ramana, J. Physl. Chems., 115(2) (2010) 554.

[39] R.T. Shannon, Acta Crystallographica Section A: Crystal Physics, Diffraction, Theoretical and General Crystallography, 32(5) (1976) 751.

[40] S.E. Shirsath, M.L. Mane, Y. Yasukawa, X. Liu and A. Morisako, Physc. Chems. Chemi. Phys., 16 (2014) 2347.

[41] P. Puspitasari, Y. Yahya, N. A. M. Zabidi and N. A. Ahmad, J. Appl. Sci.11 (2011) 1199.

[42] K.H. Maria, S. Choudhury, M.A. Hakim, J. Bangladesh Acad. of Sci. 34(2010)1.

CHAPTER 6

CONCLUSION

CHAPTER 6

CONCLUSION

6.1 Conclusion

A series of polycrystalline samples with the stoichiometric composition having the general formula $Co_{1-x}Zn_xFe_2O_4$ where x = 0.0-0.5, have been prepared using the standard double sintering ceramic technique, sintered at 1050˚C for 2 hours. The samples were characterized by X-Ray diffraction, which confirmed the single-phase cubic spinel structure since no ambiguous reflections other than the spinel structures were evidenced. From the experimental results it was observed that the lattice parameter increased with Zn content substitution. This was attributed to the substitution of larger Zn^{2+} ions over smaller Co^{2+} ion as well as a slight transformation of Fe^{3+} (0.64Å) ions from tetrahedral (A) sites to octahedral (B) sites. The lattice parameter of $CoFe_2O_4$ was found to be 8.018Å, which is very close to the standard value 8.378Å [1]. The density of all the samples increased with increasing Zn content, which may be due to the inter-granular porosity. The porosity was found to behave exactly opposite to the density with the increase of Zn content.

From microstructural study, it was observed that the grain size remained almost same with increasing Zn content. For higher content of Zn, the grain size decreased slightly. Higher value of Zn radius squeezed the radius of Cobalt. As a result, the grain size decreased when concentration of Zn is increased.

The Dielectric Constant was found to decrease with increasing frequency, which was rapid at lower frequencies and slower at higher frequencies. This is normal dielectric behavior observed in most of the ferromagnetic materials, which may be due to the interfacial polarization as predicted by Maxwell and Wagner.

DC electrical resistivity decreased with Zn Content, which is related to the decrease of grain size. The resistivity of the ferrites is expected to decrease with an increase in temperature; this may be due to the low dielectric constant and also depends on the porosity and composition. The increase in temperature of the applied field enhanced the hopping of charge carriers resulting in an increase in conduction process thereby decreasing the resistivity.

Magnetization as a function of field had been measured with a VSM at room temperature. The magnetization of all the samples was found as saturated. It was observed that the saturation magnetization and coercive field decreased with Zn content. The decrease of magnetization is due to the dilution of magnetic moment of A sub-lattice by substitution of non-magnetic Zn ions which results in replacing an equal amount of Fe^{3+} to the B-site. This enhancement of magnetization can be explained on the basis of Neel's two sub-lattice models. The change in the coercivity with the degree of zinc substitution increased and then decreased with Zn content(x). The higher coercive field showed hard magnetic nature and lower coercive field confirmed that the cobalt-ferrite is a soft ferrite [2].

Permeability decreased with Zn content, which was confirmed by the microstructural study. Again,the decrease of permeability with Zn content showed the decrease of grain size. Frequency dependence of real part of permeability, μ' was almost independent up to 2 MHz. The frequency dependence of the dielectric constant of all the samples showed the frequency-dependent phenomena i.e. the dielectric constant decreased with the increasing frequency, which confirmed the dielectric behavior of the ferrite materials and in consistent with other workers [3].

From the dielectric properties and resistivity measurement, it was observed that Zn content substitution of Cobalt (x=0.1) increased the dielectric properties and resistivity of the samples. From the magnetization study, the magnetization and permeability behaved similarly i.e. decreased with increase of frequency. Also anisotropy constant increased for x = 0.1,0.2 and then decreased with higher Zn content. So it is suggested that Cobalt ferrite with 10% Zn substitution can be used as magnetic and dielectric material. It can also be used as multiferroic material and in storage devices.

6.2 Suggestions for further work

Cobalt ferrites and allied compounds have wide spread application in microwave devices. This is largely used due to the comparatively low magnetic and dielectric losses obtainable and in particular, to the high resistivity which can be obtained by selection of suitable additives and use of appropriate firing procedures. Addition of different dopants into Co-Zn ferrites will change many properties of the materials. Further work is needed to find the suitable addition of different dopants. Changing the sintering temperature, sintering time, the heating rate and cooling rate can also be done, since these parameters also effect the properties of any magnetic materials.

Some results of this work are interpreted in terms of changed grain size with composition. However, experimental values of this parameter are not known. So, measurements of the grain size of these materials are essential. Also study on grain size with different sintering temperature can be done. The frequency dependence AC resistivity of these materials should also be measured. Also the curie temperature should be measured. We see the porous property of these ceramic materials which can be used as a humidity sensor. The humidity dependence of these materials can also be measured since the resistivity of Co-Zn ferrite changed with humidity [4].

In the M-H curves we see some hysteresis but since the applied fields are very higher order of magnitude, we could not exactly measure the hysteresis characteristics of the samples. The exact hysteresis will be found by a very low field B-H loop tracer which operates at a very small magnetic field. So hysteresis parameters of loop of the samples can be done in future. The temperature dependence of magnetization can also be done on the prepared samples using SQUID magnetometer.

References:

[1] J. Smit, H.P.J. Wign, Ferrites, John Willy and Sons, Pub. Co. New York, (1959) 143.

[2] A. hassadee, T. Jutarosaga and W. Onreabroy, proc. Eng. 32 (2012) 597.

[3] L. Néel, In Annales de Physique, 3 (1948) 137.

[4] V. Jeseentharani, M. George, B. Jeyaraj, A. Dayalan and K. S Nagaraja, J. Exp. Nanosci. 8 (2012) 358.